Doctoral Dissertation

Self-assembled Si/Silicide Bulk Composites as High-Performance Thermoelectric Materials

Jun Xie

January 2018

Division of Sustainable Energy and Environmental Engineering
Graduate School of Engineering,
Osaka University

Abstract

With the continuous development of nanostructure engineering technology, bulk nanostructured materials are focused on for thermoelectricity. Si is rich in resources, low-cost, nontoxic materials, and available in industrial quantities. This thesis work mainly developed and investigated the bulk Si, which demonstrated a great potential for thermoelectric (TE) applications at high temperature owing to an enhanced phonon scattering and reserved electrical performance by forming refined and self-assembled nanoscale structure.

Chapter 1 reviewed the latest progress in nanostructure engineering of TE materials from the perspective of physical background to the recent advances. The great challenges in developing bulk Si-based materials for practical thermoelectric application were also addressed.

Chapter 2 presented detailed information on the synthesis technique, phase analysis, microstructure characterization and TE properties measurement, which were used in the experimental researches.

Chapter 3 systematically studied TE properties of heavily-doped monocrystalline Si. The TE properties of p-type and n-type heavily doped monocrystalline Si were measured from room temperature to above 1000 K. By modeling the experimental results, a theoretical model was proposed to provide a reasonable estimation of the TE properties for heavily-doped monocrystalline Si based on Boltzmann transport equation, which laid the groundwork for our following researches to design and fabricate high-performance Si TE composites.

Chapter 4 employed a simple self-assembly process through melt-spinning technology and spark plasma sintering to prepare p-type Si/SiB_3 and $Si/CoSi_2$ composites. Precipitates with size ranging from tens to 500 nanometers were observed in Si matrix, which only slightly affected the electrical properties and greatly reduced the lattice thermal conductivity by 20% - 44% compared to a homogeneous p-type Si with a similar carrier concentration. Enhanced *ZT* values of 0.21 for $Si/CoSi_2$ and 0.23 for Si/SiB_3 at 1073K were obtained. The results showed that the self-assembled precipitation is effective in improvement of the TE performance of Si, and demonstrated that *ZT* can be further increased by optimizing the size of precipitates.

Chapter 5 explored a novel route to introduce dislocations in n-type Si/Silicide TE composites. Multi-scaled microstructures, including high-density nanoprecipitates and dislocations, were assembled together by controlling the sintering temperature of a synthesis process based on the route that was employed in chapter 4. These dislocations were found naturally decorated with nanodots, stacking faults and dislocation cores as well as the related strain fields. Calculations indicated that in addition to a 30% reduction in lattice thermal conductivity by nanoprecipitates, the naturally decorated dislocations contributed an additional 50% reduction, resulting a comparative high figure of merit of 0.39 at 1045K. This work offered a unique route for introducing multi-scale microstructures and a new strategy for *ZT* enhancement in bulk Si TE materials.

Chapter 6 proposed an outlook for future researches in bulk Si TE materials via an overall comparison of the TE properties of self-assembled Si/Silicide composites with the newly-developed theoretical model and all the available literature data for bulk Si-based thermoelectric materials.

Index

1. General introduction

1.1 Background

With the growth of population and the improvement of living standards, energy supply has become increasingly concerned around the world over the past few decades. About 90% of the global electricity is still generated by the heat of burning fossil fuels such as natural, oil and coal. Generally speaking, the operation efficiency of plants is about 30%-40%, which shows that vast waste heat can be further used. By improving efficiency and reducing fuel costs, the waste heat can be recovered to available electricity, which is also conductive to environmental protection. The waste heat can be recovered and turned to useful energy through thermoelectric technology. According to the energy conversion between electrical energy and heat, the thermoelectric device in Figure 1.1 can be used to convert heat generated by the sources like industrial processes, automotive exhaust and solar radiation to electricity. Thermoelectric equipment (solid equipment with no moving part) has been widely used in satellite, computer chips and infrared sensor because of its excellent reliability. However, the low efficiency of thermoelectric equipment limits its extensive application. To this end, it has become a crucial part of solving the current energy challenges and key problems in the research field to look for materials with a significant increase in efficiency.[1][2][3]

Silicon (Si) is rich in resources. As a low-cost TE material, it has been widely applied in industrial processing at high temperature, and attracts great attention. Because of the remarkable thermal conductivity, Si is a perfect material to test the increase of TE attributes through nanostructuring.[4] This paper systematically studies the thermoelectric attributes of heavily doped monocrystalline Si. Moreover, the enhancement of its thermoelectric performance through the introduction of nanostructures to Si matrix is further explored. Based on the combination of theoretical and experimental methods, this paper aims to narrow the gap between experimental research and theoretical thinking, which provides a crucial design perspective to further explore the preparation of high-performance TE composite.

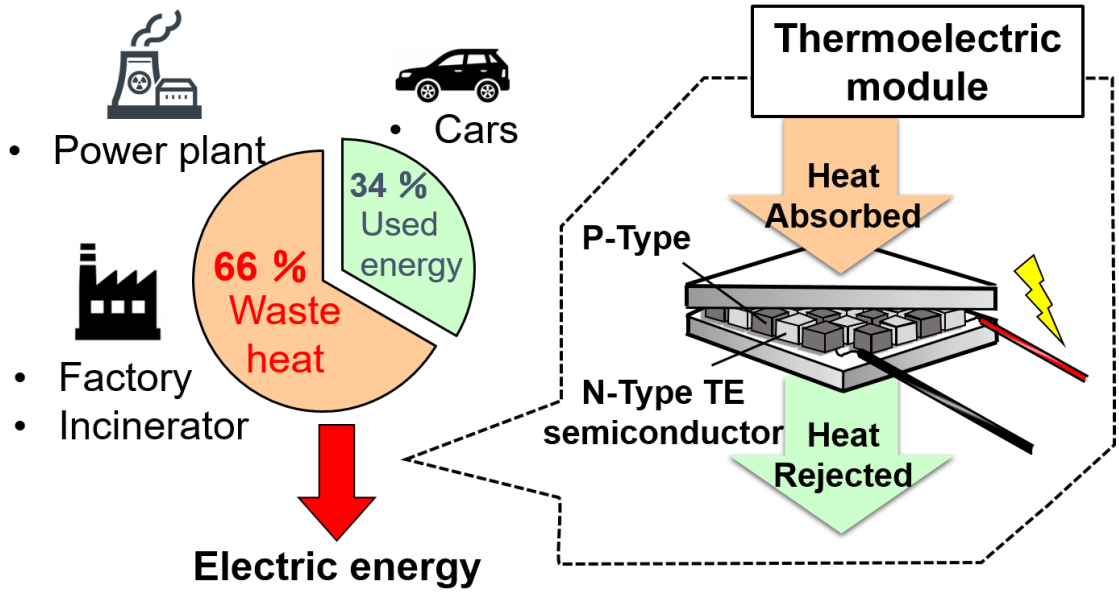

Fig. 1.1 A Schematic diagram of heat-electric energy convention and thermoelectric device.

1.2 Thermoelectric phenomena

1.2.1 Introduction

Thermoelectric materials are defined as the materials that can directly convert thermal energy into electrical energy. The fundamental mechanism of the thermoelectric effect is related to free carriers in semiconductors and metals. In order to further understand the thermoelectric materials, this section introduces the three major thermoelectric effects, namely, Thomson effect, Peltier effect and Seebeck effect, as well as the electron and phonon transport phenomena.

1.2.2 Thermodynamics

Obviously, thermocouple should be realized through materials with low thermal conductivity, high electrical conductivity and great thermoelectric coefficient. Thermal conductivity κ and electrical conductivity σ are well-known to readers. However, thermoelectric coefficient should be further defined. As shown in Figure 1.2, open circuit potential difference dV is resulted from temperature difference dT between conductor b and conductor junctions. Differential Seebeck coefficient S_{ab} is defined as below:

$$dS_{ab} = dV/dT \tag{1.1}$$

According to Figure 1.3, the rate of reversible heat absorption or generation Q is resulted from the current I passing through the junction between conductor a and conductor b. Peltier coefficient is:

$$\pi_{\mathrm{ab}} = Q/I \tag{1.2}$$

In Figure 1.4, current I passes through a single uniform conductor with a temperature difference ΔT, leading to a reversible heat generation rate ΔQ. Thomson coefficient γ is defined as below:

$$d\gamma = dQ/IdT \tag{1.3}$$

The thermoelectric coefficients discussed above are relevant with Kelvin relationships:

$$\gamma_a - \gamma_b = T\frac{dS_{ab}}{dT} \tag{1.4}$$

and

$$\pi_{\mathrm{ab}} = S_{ab}T \tag{1.5}$$

The second equation is of great importance because it indicates Peltier coefficient to Seebeck coefficient than can be measured more easily.

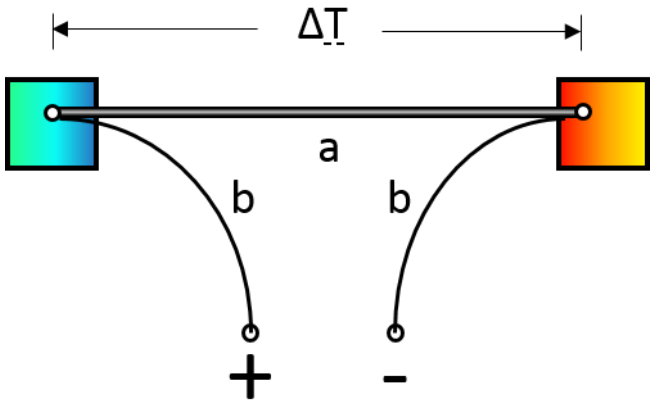

Fig. 1.2 Schematic diagram of thermoelectric effect[5].

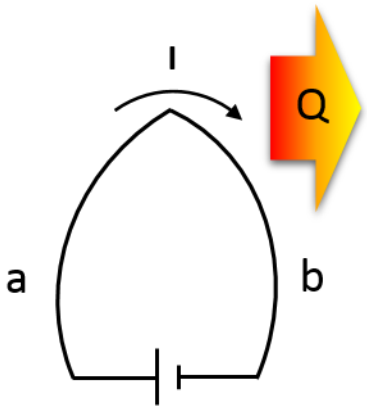

Fig. 1.3 Schematic diagram of Peltier effect[5].

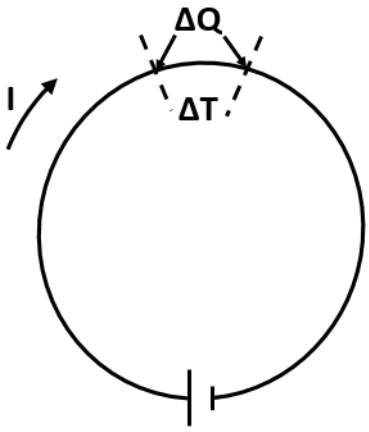

Fig. 1.4 Schematic diagram of Thomson effect[5].

1.2.3 Thermoelectric conversion efficiency and the figure-of-merit

Thermoelectric converter, as a heat engine, follows thermodynamic law. If the converter operation is regarded as an ideal generator without heat loss, efficiency refers to the ratio of output power to the load to absorbed heat energy by the contact. Based on the simplest generation containing a thermocouple with p-type and n-type semiconductors, which are attached to conductors, as shown in Figure 1.5 and 1.6.

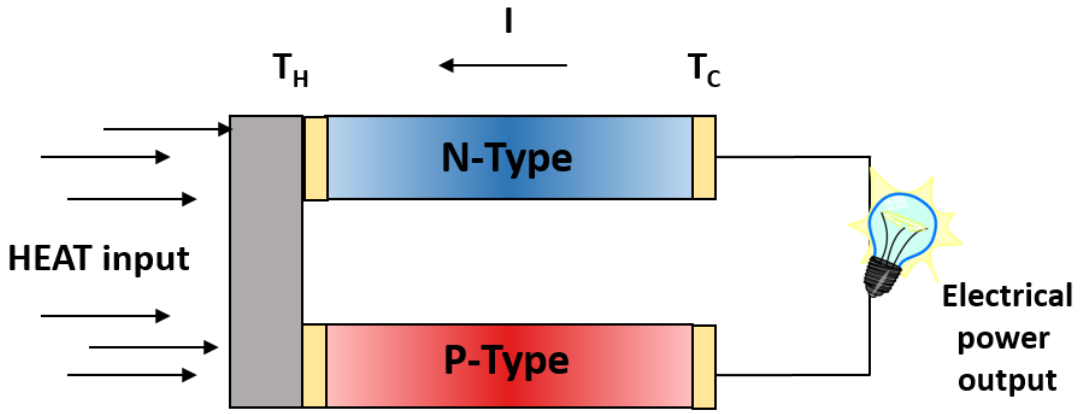

Fig. 1.5 The Seebeck effect (Thermoelectric generation).

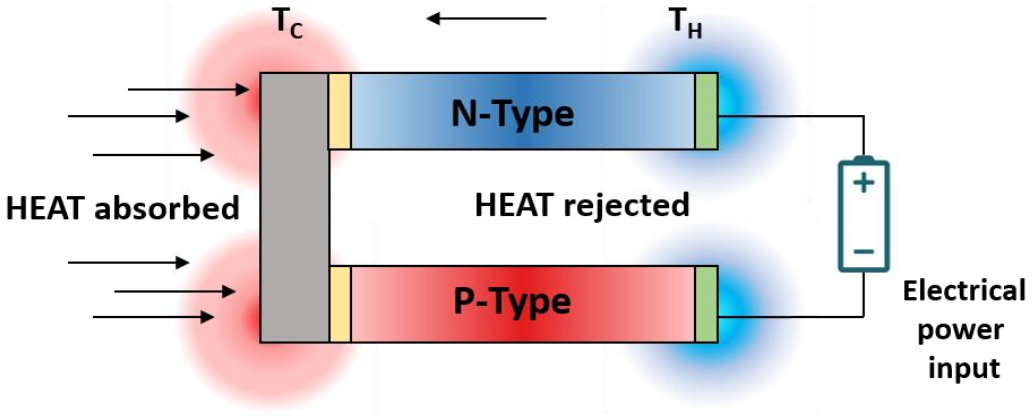

Fig 1.6 The Peltier effect (Thermoelectric cooling).

The generator efficiency can be described by[6]

$$\phi = \frac{output\ power}{absorbed\ heat\ energy} \tag{1.6}$$

Here, Seebeck coefficients, thermal conductivities and electrical conductivities of *a* and *b* arc are assumed to be are assumed to be constant in an arm. Compared with the total arm resistance, the contact resistance at the cold and hot junctions can be neglected. Therefore, the generator efficiency is as below:

$$\phi = \frac{I^2R}{S_{ab}IT_H = \kappa'(T_H - T_C) - \frac{1}{2}I^2R} \tag{1.7}$$

Where, λ' represents the thermal conductance between *a* and *b*. R represents the series resistance. For

thermoelectric material, S, σ and κ' vary with the temperature, and both refrigeration and generation should be considered. However, if the approximate mean value is used within the range of temperature, the simple expression of the parameters can still be acceptable so as to make appropriate allowance for contact resistance.

When the output efficiency reaches peak value, it can be expressed as:

$$\phi_p = \frac{T_H - T_C}{\frac{3T_H}{2} + \frac{T_C}{2} + \frac{4}{Z_c}} \tag{1.8}$$

The maximum efficiency is:

$$\phi_{max} = \eta_c \gamma \tag{1.9}$$

Where

$$\eta_c = \frac{T_H - T_C}{T_H} \tag{1.10}$$

$$\gamma = \frac{\sqrt{1 + Z_C \bar{T}} - 1}{\sqrt{1 + Z_C \bar{T}} + \frac{T_C}{T_H}} \tag{1.11}$$

and

$$\bar{T} = \frac{T_H + T_C}{2} \tag{1.12}$$

and

$$Z_c = \frac{\alpha_{ab}^2}{R\kappa} \tag{1.13}$$

where Z_c is the thermoelectric figure of merit of the couple. The maximum efficiency is the product of Carnot efficiency, which is smaller than unity. γ is obviously smaller than unity. This indicates that material parameters.

The heat absorption is minimized by matching the geometries of *a* and *b*.

$$Z_c = \frac{\alpha_{ab}^2}{\left[\left(\frac{\kappa_a}{\sigma_a}\right)^{\frac{1}{2}} + \left(\frac{\kappa_b}{\sigma_b}\right)^{\frac{1}{2}}\right]} \tag{1.14}$$

The material constants of the two junction arms are similar in practice. In this case, a figure-of merit for a material is defined:

$$Z = \frac{\alpha^2 \sigma}{\kappa} \tag{1.15}$$

Where, $\alpha^2\sigma$ is the electrical power factor.

Thermoelectric parameters in figure-of-merit are assumed to be irrelevant with temperature, and the above relationship can be derived. Although this is not the general case, it is assumed that the results provided by the average value are within 10% of the real value.

As shown in Figure 1.7, the conversion efficiency ϕ_{max} is a function of operation temperature difference and a series of figure-of-merit values of the material. Obviously, the increase of temperature difference correspondingly

enhances the available heat for the conversion indicated by Carnot efficiency. Therefore, the wide temperature difference is ideal. Figure 1.8 shows the relationship between $Z\bar{T}$ and ϕ_{max} when T_C = 300 K. In order to achieve higher thermoelectric efficiency, a higher Z and a larger temperature difference are necessary. From the perspective of commercial use, devices with $ZT_m > 1 \sim 1.5$ are more likely to realize the efficiency η> 0.1.

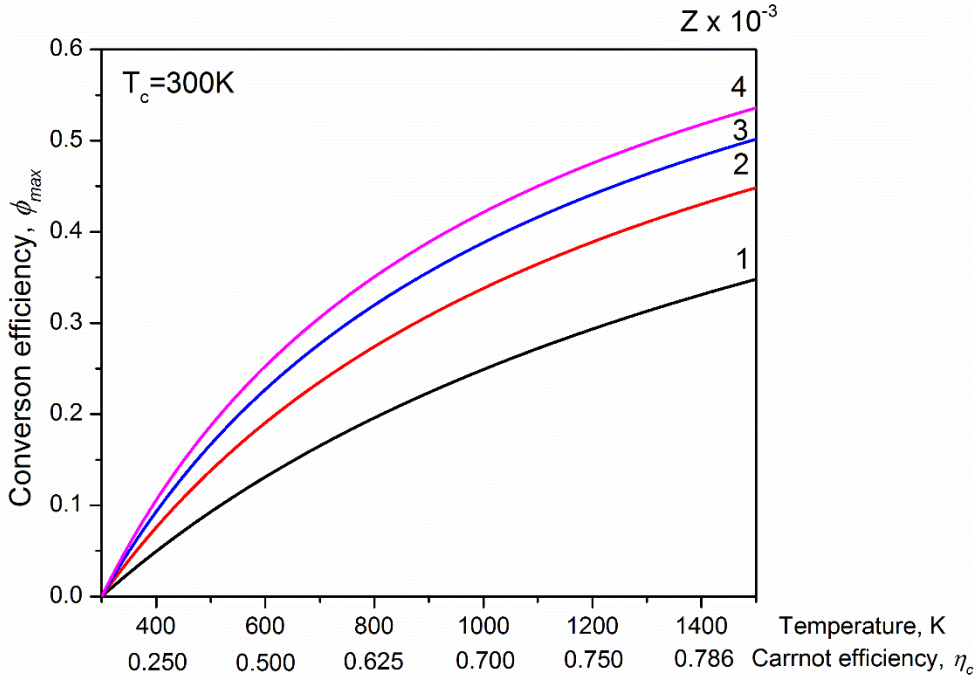

Fig 1.7 Generating efficiency as a function of temperature and thermocouple material figure-of merit.

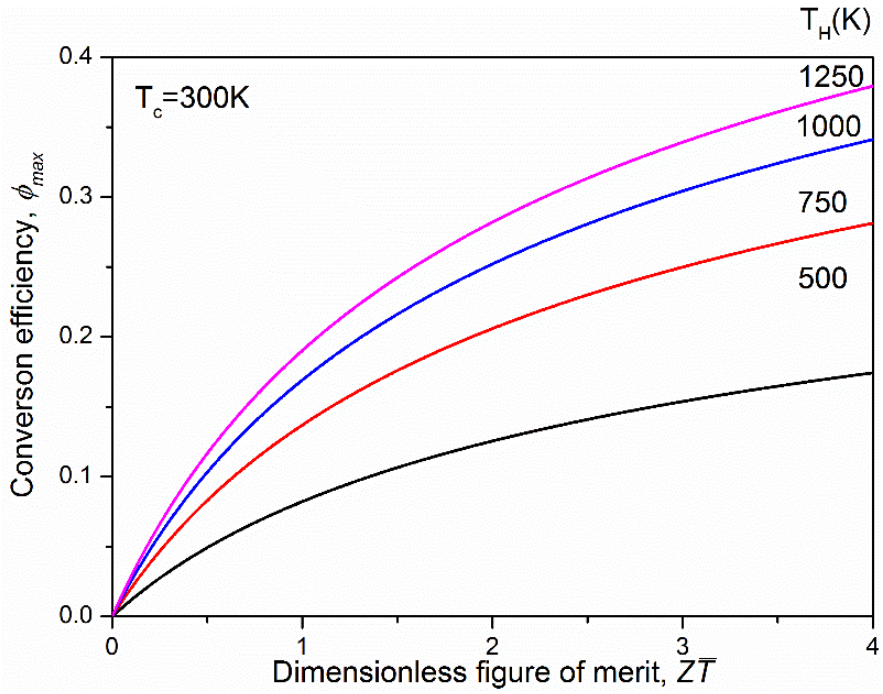

Fig 1.8 *ZT* dependent maximum efficiency, ϕ_{max}, in the case of T_C = 300 K.

1.2.4 Thermoelectric transport theory

This section discusses the dimensionless merit value *ZT*, including electrical conductivity σ, Seebeck coefficient *S* and thermal conductivity κ, which can be acquired from transport equations of carrier and phonon

I. Electrical Properties

The isotropic conductor with the Fermi level ε_F and conduction band edge $\varepsilon_C = 0$ are considered. In the equilibrium state, the Fermi function gives the occupation of states when the energy ε is higher than the bottom of the guide band[7].

$$f_0(\varepsilon) = \frac{1}{\exp((\varepsilon - \varepsilon_F)/k_B T) + 1}, \tag{1.16}$$

Where, k_B is the constant of Boltzmann. The carrier energy ε is defined through the equation as below:

$$\varepsilon = \frac{\eta^2}{2m^*}\left(k_x^{\,2} + k_y^{\,2} + k_z^{\,2}\right) = \frac{m^*}{2}\left(v_x^{\,2} + v_y^{\,2} + v_z^{\,2}\right) \tag{1.17}$$

Where, $\hbar$ is the Planck's constant divided by 2π, *v* the velocity, m^* the effective mass of electrons and *k* the wave number.

The distribution in *k*-space is shifted to the field by an electric field *E* in the *x*-direction through a displacement which is proportional to *E*. The relaxation time τ is determined through the electron scattering processes where the normal distribution is restored.

$$f = f_0 + \frac{(-e)E}{\eta}\tau\frac{\partial f_0}{\partial k_x} = f_0 + (-e)Ev_x\tau\frac{\partial f_0}{\partial E}. \tag{1.17}$$

The current density which is corresponding to the corrected angular distribution is

$$j = -e\int_0^\infty v_x(f - f_0)D(\varepsilon)d\varepsilon, \tag{1.18}$$

Where, *e* represents the electron charge. The energy (heat) flux that the electron can transfer is written as:

$$W = \int_0^\infty v_x(\varepsilon - \varepsilon_F)(f - f_0)D(\varepsilon)d\varepsilon. \tag{1.19}$$

Where, $D(\varepsilon)$ represents the density of state in the conduction band on the energy scale, and the spherical energy surfaces of $\varepsilon \propto \boldsymbol{k}^2$ (SPB model) is assumed as

$$D(\varepsilon) = \frac{1}{2\pi^2}\left(\frac{2m^*}{\eta^2}\right)^{3/2}\varepsilon^{1/2}. \tag{1.20}$$

If we know the change of the relaxation time with the electron energy, the integration can be implemented. The simple relationship is assumed as

$$\tau = \tau_0\xi^s, \tag{1.21}$$

Where, $\xi = \varepsilon / k_B$ is the reduced energy.

$$j = -eE\frac{4e\tau_0}{3\pi^{1/2}m^*}N_C K_{s+3/2}, \tag{1.22}$$

and

$$W = E\frac{4e\tau_0}{3\pi^{1/2}m^*}N_C\left(k_BT\cdot K_{s+5/2}-\varepsilon_f\cdot K_{s+3/2}\right), \tag{1.23}$$

with

$$N_C = 2\left(\frac{m^*k_BT}{2\pi\eta^2}\right)^{3/2}, \tag{1.24}$$

and

$$K_n = \int_0^\infty \xi^n \frac{\exp\left(\xi-\xi_F\right)}{\left(1+\exp\left(\xi-\xi_F\right)\right)^2}d\xi\,. \tag{1.25}$$

Obviously, when $\xi_F \gg 1$,

$$K_n = n!\exp\left(\xi_F\right), \tag{1.26}$$

while

$$K_n = \left(\xi_F\right)^n\left[1+\frac{\pi^2}{6}n(n-1)\left(\frac{1}{-\xi_F}\right)^2+\Lambda\right], \tag{1.27}$$

Equation (1.26) can be applied to n-type semiconductor. Equation (1.27) is applicable for metal. Seebeck coefficient can be obtained according to equations (1.22) and (1.23).

$$S = \frac{W}{jT} = -\frac{k_B}{e}\left(\frac{K_{s+5/2}}{K_{s+3/2}}-\xi_F\right). \tag{1.28}$$

Partial integration is applied to equation (1.28), and we can obtain equation (1.29).

$$S = -\frac{k_B}{e}\left(\frac{s+5/2}{s+3/2}\frac{F_{s+3/2}\left(\xi_F\right)}{F_{s+1/2}\left(\xi_F\right)}-\xi_F\right) \tag{1.29}$$

Where, F_n is Fermi integral

$$F_n\left(\xi_F\right) = \int_0^\infty \frac{\xi^n}{\exp\left(\xi-\xi_F\right)+1}d\xi\,. \tag{1.30}$$

In a similar way, the current with thermal scattering can be obtained from equation (1.23).

$$j = -\sigma E\,. \tag{1.31}$$

Therefore, the electrical conductivity can be defined through the equation as below:

$$\sigma = \frac{4e^2\tau_0}{3\pi^{1/2}m^*}N_CK_{s+3/2}$$

$$= \frac{4e^2\tau_0N_C}{3\pi^{1/2}m^*}\left(s+\frac{3}{2}\right)F_{s+1/2}\left(\xi_F\right) \tag{1.32}$$

Carrier concentration n can be expressed:

$$n = \int_0^\infty D\left(\varepsilon\right)f_0\left(\varepsilon\right)d\varepsilon \tag{1.33}$$

$$= \frac{2}{\pi^{1/2}} N_{\mathrm{C}} F_{1/2}(\xi_{\mathrm{F}}). \tag{1.34}$$

According to equations (1.34) and (1.36), carrier mobility $\mu = \sigma / ne$ can be written as

$$\mu = \frac{2e\tau_0}{3m^*}\left(s+\frac{3}{2}\right)\frac{F_{s+1/2}(\xi_{\mathrm{F}})}{F_{1/2}(\xi_{\mathrm{F}})}. \tag{1.35}$$

Electronical thermal conductivity κ_{e} can be estimated in a similar way with that of electrical conductivity. The variation of the distribution function generated by the thermal gradient in the material is corresponding to the drop of the electron drift gradient. In the insulating sample, this drift generates a reverse electric field for the carrier diffusion. The flow of electronic energy on the temperature gradient is balanced through the smaller energy electron flow in the opposite direction. The thermal conductivity of the electron is obtained through calculation.

$$\begin{aligned}\kappa_{\mathrm{e}} &= \frac{4\tau_0 N_{\mathrm{C}}}{3\pi^{1/2}m^*}{k_{\mathrm{B}}}^2 T\left[K_{s+7/2} - \frac{K_{s+5/2}^2}{K_{s+3/2}}\right] \\ &= \frac{4\tau_0 N_{\mathrm{C}}}{3\pi^{1/2}m^*}{k_{\mathrm{B}}}^2 T\left[\left(s+\frac{7}{2}\right)F_{s+5/2}(\xi_{\mathrm{F}}) - \frac{\left(s+\frac{5}{2}\right)^2\{F_{s+3/2}(\xi_{\mathrm{F}})\}^2}{\left(s+\frac{3}{2}\right)F_{s+1/2}(\xi_{\mathrm{F}})}\right]\end{aligned} \tag{1.36}$$

Moreover, the Lorenz number is obtained according to the Wiedemann-Franz law.

$$L = \frac{\kappa_{\mathrm{e}}}{\sigma T} = \left(\frac{k_{\mathrm{B}}}{q}\right)^2\left[\frac{(s+7/2)F_{s+5/2}(\xi_{\mathrm{F}})}{(s+3/2)F_{s+1/2}(\xi_{\mathrm{F}})} - \frac{(s+5/2)^2 F_{s+3/2}^2(\xi_{\mathrm{F}})}{(s+3/2)^2 F_{s+1/2}^2(\xi_{\mathrm{F}})}\right] \tag{1.37}$$

The Lorentz number of metals is computed:

$$L = \frac{k_{\mathrm{B}}}{e^2}\frac{\pi^2}{3} = 2.44\times10^{-8}\ \ \mathrm{W\Omega K^{-2}} \tag{1.38}$$

A similar relationship can also be applied to semiconductors with heat scattering.

$$L = \frac{k_{\mathrm{B}}}{e^2}\cdot 2 = 1.49\times10^{-8}\ \ \mathrm{W\Omega K^{-2}}. \tag{1.39}$$

The electrical parameters are determined by the reduced Fermi energy. Figure 1.9 shows the relationship between the reduced Fermi energy and the parameters. Carrier scattering mechanisms determine the scattering parameter *s*. Figure 1.9 selects the two typical values of $s = -1/2$ and 3/2 for common scattering mechanisms. When acoustic deformation potential dominantly scatter the carriers, $s = -1/2$. When the carriers are scattered by ionized impurities, $s = 3/2$[8]. Scattering parameter is energy dependence of relaxation time $\tau = \tau_0(T)\xi^s$. Table 1.1 summarizes the probability of scattering, namely, the reciprocal of relaxation time. As shown in Table 1.1, the alloy scattering and the piezoelectric scattering are $s = 1/2$ and $-1/2$, respectively.

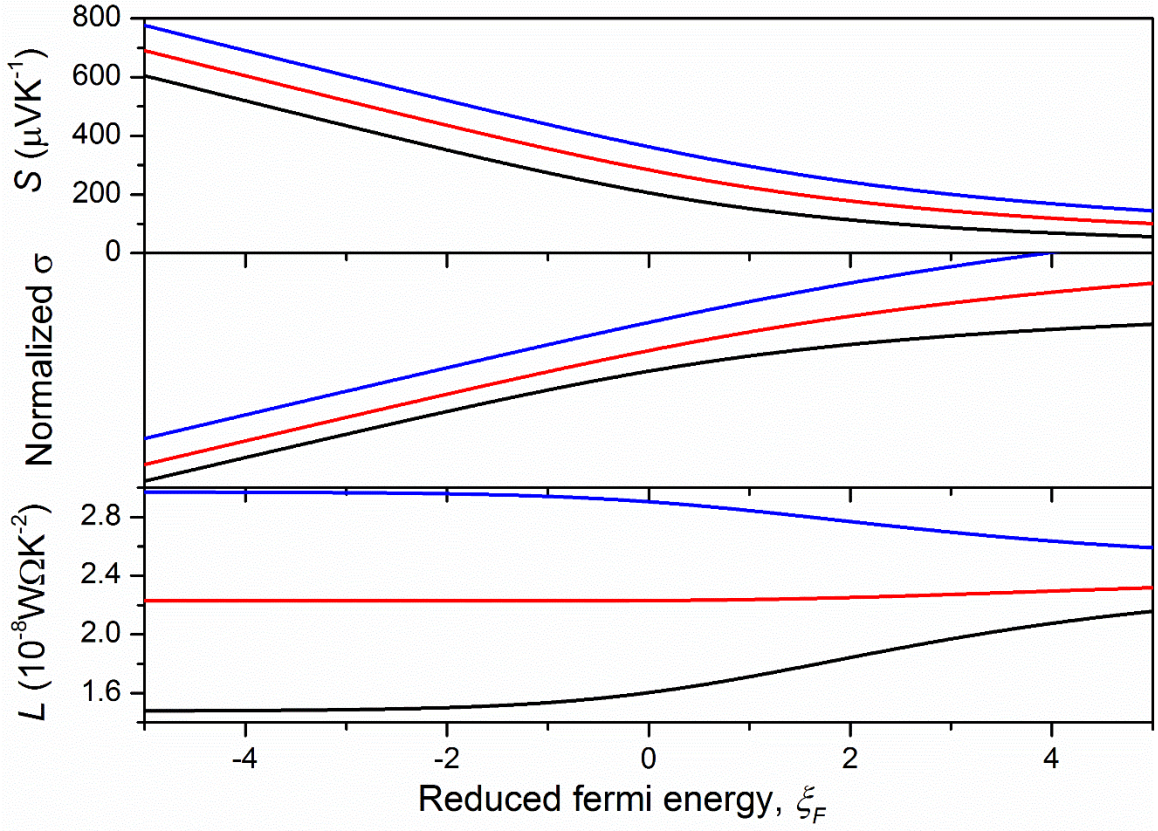

Fig. 1.9 Reduced Fermi energy dependence of electrical properties[8].

Table 1.1 Scattering probability of carriers for each scattering mechanism[8].

Scattering mechanism	Scattering probability
Acoustic deformation potential scattering	$\frac{1}{\tau_{ac}} = \frac{\sqrt{2}E_{def}^2\left(m^* k_B T\right)^{3/2}}{\pi d \eta^4 v_s^{\ 2}} \xi^{1/2}$
Ionized impurity scattering	$\frac{1}{\tau_{ii}} = \frac{N_i Z^2 e^4}{16\sqrt{2}\pi m^{*1/2}\varepsilon^2\left(k_B T\right)^{3/2}}\left[\ln\left(1+p(\xi)\right) - \frac{p(\xi)}{1+p(\xi)}\right]\xi^{-3/2}$ $p(\xi) = \frac{8m^*\varepsilon\left(k_B T\right)^2}{\eta^2 e^2 n}\xi$
Piezoelectric scattering	$\frac{1}{\tau_p} = \frac{\left(eK_p\right)^2 m^{*1/2}\left(k_B T\right)^{1/2}}{2\sqrt{2}\varepsilon^2 d v_s^{\ 2}\eta^2}\xi^{-1/2}$
Alloy scattering	$\frac{1}{\tau_{al}} = \frac{\sqrt{2}y(1-y)\left(\Delta V\right)^2 m^{*3/2}\left(k_B T\right)^{1/2}}{N_0 \pi \eta^4}\xi^{1/2}$

E_{def}: Acoustic deformation potential constant
d: Density of material
v_s: Mean sound velocity
N_i: Concentration of ionized impurity
Z: Charge of ionized impurity
ε: Dielectric constant
n: Carrier concentration
K_p: Piezoelectric constant
y: Composition of alloyed impurity
ΔV: Band offset
N_0: Number of atoms per unit volume

II. Thermal Properties

Heat is transported by phonon conduction through a semiconductor and electrons through the lattice. Based on the electrical contribution κ_e discussed above, this section will further discuss lattice thermal conductivity κ_l. Phonons is created and annihilated through phonon scattering events constrained by momentum and energy conservation. In the equilibrium state, the scattering events lead to the average occupancy of each phonon state in the Bose Einstein statistical description.[9]

$$f_0 = \frac{1}{e^{\frac{h\omega}{k_B T}-1}} \tag{1.40}$$

where k_B is Boltzmann's constant. In the nonequilibrium state, a solution to BTE (Boltzmann transport equation) can describe the nonequilibrium occupation and net energy transport. The BTE for phonons is solved through a typical approximation, which is a SMRT (single mode relaxation time approximation). The occupation is assumed to exponentially decay to the value in equilibrium state. BTE for the distribution in nonequilibrium state can be solved based on the assumption that the spatial and time derivate of the deviation of distribution from equilibrium $f - f_0$ can be neglected compared with the spatial variation f_0.

$$f(\boldsymbol{r}, \boldsymbol{k}, p) = f_0 - \frac{df_0}{dT} \cdot \nabla \mathrm{T} \cdot \boldsymbol{\nu} \cdot \tau, \tag{1.41}$$

Where, wave vector $\boldsymbol{k}$ is the phonon state, the location in the system is described by $\boldsymbol{r}$. Polarization p includes the relaxation time τ and velocity $\boldsymbol{\nu}$. According to the distribution, the heat flux (net energy flux) carried by a phonon in the direction of X can be written based on the summarization of phonon contribution with occupation:

$$J_x(x) = \frac{1}{V} \sum_p \sum_{k_x=-\infty}^{\infty} \sum_{k_y=-\infty}^{\infty} \sum_{k_z=-\infty}^{\infty} h\omega \cdot f \cdot \boldsymbol{\nu} \cdot \hat{x}. \tag{1.42}$$

Taking the system to be large, wave vector summations can be converted to the spherical integral over $\boldsymbol{k}$-space through discrete k-space interval of $\Delta\|\boldsymbol{k}\| = 2\pi/L$, where L is the length of the system in each direction.

$$J_x(x) = \frac{1}{V} \sum_p \int_0^{\infty} \int_0^{2\pi} \int_0^{\pi} h\omega \cdot f \cdot v_x \cdot \frac{k^2 dk \sin(\theta)\, d\theta d\varphi}{V \cdot \left(\frac{2\pi}{L}\right)^3}. \tag{1.43}$$

With $\boldsymbol{k}$-space as isotropic, the density of states $D(\omega)$ (the state number in a differential frequency interval) is substituted. $(2\pi/L)^3$ is the volume of $\boldsymbol{k}$-space occupied by state. Equation (1.43) is written as the integral on the phonon frequency and two spatial integrals.

$$J_x(x) = \frac{1}{V} \sum_p \int_0^{\omega_{max}} \int_0^{2\pi} \int_0^{\pi} h\omega \cdot f \cdot v_x \cdot D(\omega) \cdot \sin(\theta)\, d\theta d\varphi d\omega. \tag{1.44}$$

Equation (1.41) is substituted to nonequilibrium occupation. Relaxation times τ and isotropic velocities ν are assumed, and the spatial integrals can be carried out:

$$J_x(x) = -\left\{\frac{1}{3}\sum_p \int_0^{\omega_{max}} \int_0^{2\pi} \int_0^{\pi} \left[h\omega \cdot D(\omega) \cdot \frac{df_0}{dT}\right] v^2 \tau d\omega\right\} \cdot \frac{dT}{dx} \tag{1.45}$$

The form is the same as Fourier's law of heat conduction

$$C(v) = -\frac{dE}{dx} = \left[h\omega \cdot D(\omega) \cdot \frac{df_0}{dT}\right], \tag{1.46}$$

where, is the frequency that unit volume depends on the specific heat. Expression of thermal conductivity is as below:

$$\kappa = \sum_p \frac{1}{3} \int_0^{\omega_{max}} C \cdot v^2 \cdot \tau_{eff} \cdot d\omega = \sum_p \frac{1}{3} \int_0^{\omega_{max}} C \cdot v \cdot \Lambda_{eff} \cdot d\omega, \tag{1.47}$$

Where, velocity v of phonon group is generally greater than that of sound in branches:

$$v^{-1} = \frac{1}{3}(v_{SL}^{-1} + 2v_{ST}^{-1}) \tag{1.48}$$

τ_{eff} and Λ_{eff} are relaxation time and effective phonon mean free path, respectively. Through Equation (1.47), spectral dependence of the thermal conductivity of solid phonons can be investigated. Polarizations are summarized in Equation (1.48), so that the separate contributions in each branch can be determined, and the polarization that dominates a specific material can be identified.

In real crystals, a variety of scattering experienced by the phonons limit the transmission process. Phonon-phonon scattering because of lattice potential anharmonicity, including Umklapp phonon-phonon scattering and normal phonon-phonon scattering, is the basic scattering mechanism. The other scattering mechanisms include:

- Phonon scattering at defects and impurities
- Phonon scattering at surfaces or grain boundaries
- Phonon scattering with carriers
- Phonon scattering with nanoparticles

Various scattering mechanisms are likely to dominate at different temperatures and in different structures and materials. Phonon-interface/surface scattering in nanostructures occupies the transport at room temperature and even higher temperatures, which is similar with that in bulk materials at low temperature. The scattering categories can be differentiated according to the phonons type. It is difficult to evaluate the scattering integrals for phonons. According to Matthiessen's rule, the effective relaxation time of phonon is written as

$$\Lambda_{eff}^{-1} = \Lambda_U^{-1} + \Lambda_{AD}^{-1} + \Lambda_{GB}^{-1} + \Lambda_{PE}^{-1} + \Lambda_{NP}^{-1} \tag{1.49}$$

Table 1.2 Equations for mean free paths (Λ) associated with different types of scattering processes[10][11]

Phonon scattering processes	Phonon mean-free path
Umklapp scattering	$\Lambda_U^{-1} = \frac{B_1 \omega^2 T e^{-\frac{B_2}{T}}}{v}$
Alloy disorder scattering	$\Lambda_{PD}^{-1} = \frac{\bar{V}\omega^4}{4\pi v^3} \sum_i f_i \left\{ \left(\frac{M - M_i}{M} \right) + \varepsilon \left(\frac{\delta - \delta_i}{\delta} \right)^2 \right\}$
Carrier-Phonon scattering	$\Lambda_{EP}^{-1} = \frac{E_F^2 m^{*2} \omega}{2\pi\hbar^3}$
Grain boundary scattering	$\Lambda_{GB}^{-1} = D_A$
Nanoparticle scattering	$\Lambda_{NP}^{-1} = (\Gamma_R^{-1} + \Gamma_G^{-1})^{-1} \rho$ $\Gamma_R = \pi R^2 \frac{4}{9} (\frac{d - d_i}{d})^2 (\omega R / v)^4$ $\Gamma_G = 2\pi R^2$

Table 1.3 Parameters for the Boltzmann transport equation with frequency-dependent phonon mean free path

Property		**Parameters**
Sound velocity	Longitude	v^L
	Transverse	v^T
	Group	v
Debye temperature	Longitude	θ^L
	Transverse	θ^T
Umklapp scattering parameters		B_1 B_2
Fractional concentration of the impurity		f_i
Volume of a primitive cell		$\bar{V}$
Averaged atomic mass		M
Atomic mass of impurity		M_i
Averaged atomic radius		δ
Atomic radius of impurity		δ
Alloy disorder scattering parameter		ε
Electron-phonon deformation potential		E_F
Density-of-stages effective mass		m^*
Grain size		D_A
Density of matrix		d
Density of particles		d_i
Radius of particles		R_A
Number density of particles		ρ_A

1.2.5 **Optimization of Thermoelectric Figure of Merit**

Based on the electron transport model demonstrated above, the dimensionless figure of merit *ZT* can be expressed as[12]

$$ZT = \frac{S^2}{\rho\kappa} = \frac{S^2}{L + \frac{\rho\kappa_{\text{latt}}}{T}} = \frac{\left\{\frac{\left(s+\frac{5}{2}\right)F_{s+\frac{3}{2}}(\xi_{\text{F}})}{\left(s+\frac{3}{2}\right)F_{s+\frac{1}{2}}(\xi_{\text{F}})} - \xi_{\text{F}}\right\}^2}{\frac{\left(s+\frac{7}{2}\right)F_{s+\frac{5}{2}}(\xi_{\text{F}})}{\left(s+\frac{3}{2}\right)F_{s+\frac{1}{2}}(\xi_{\text{F}})} - \{\delta(\xi_{\text{F}})\} + \frac{1}{B\varepsilon(\xi_{\text{F}})}} \tag{1.50}$$

where

$$B \equiv \frac{{k_{\text{B}}}^2}{q} N_{\text{B}} \frac{T\mu_c}{\kappa_{\text{latt}}} \tag{1.51}$$

$$\varepsilon(\xi_{\text{F}}) = \frac{F_{s+\frac{1}{2}}(\xi_{\text{F}})}{\Gamma\left(s+\frac{3}{2}\right)} \tag{1.52}$$

Carrier distribution is asymptotic to Maxwell distribution at high temperature. Therefore, the Fermi integral is as below:

$$F_s(\xi_{\text{F}}) = \int_0^\infty \frac{\xi^s}{\text{e}^{\xi-\xi_{\text{F}}+1}} d\xi \approx \text{e}^{\xi_{\text{F}}}\Gamma(s+1) \tag{1.53}$$

$$\Gamma(z) \equiv \int_0^\infty \text{e}^{-x} x^{z-1} dx \tag{1.54}$$

The reduced Fermi energy ξ_F, the attributes of base materials *B* and the scattering process *s* jointly determine *ZT*. As shown in Figure 1.10, the maximum value of *ZT* which is a function of ξ_F is increased with Parameter B. In other words, the carrier concentration should be optimized, and materials with higher B should be found so that *ZT* can be increased. According to Equation (1.51), lower carrier mobility and lattice thermal conductivity can lead to higher B. Therefore, low thermal conductivity of lattice which does not destroy electrical properties is necessary for thermoelectric materials.

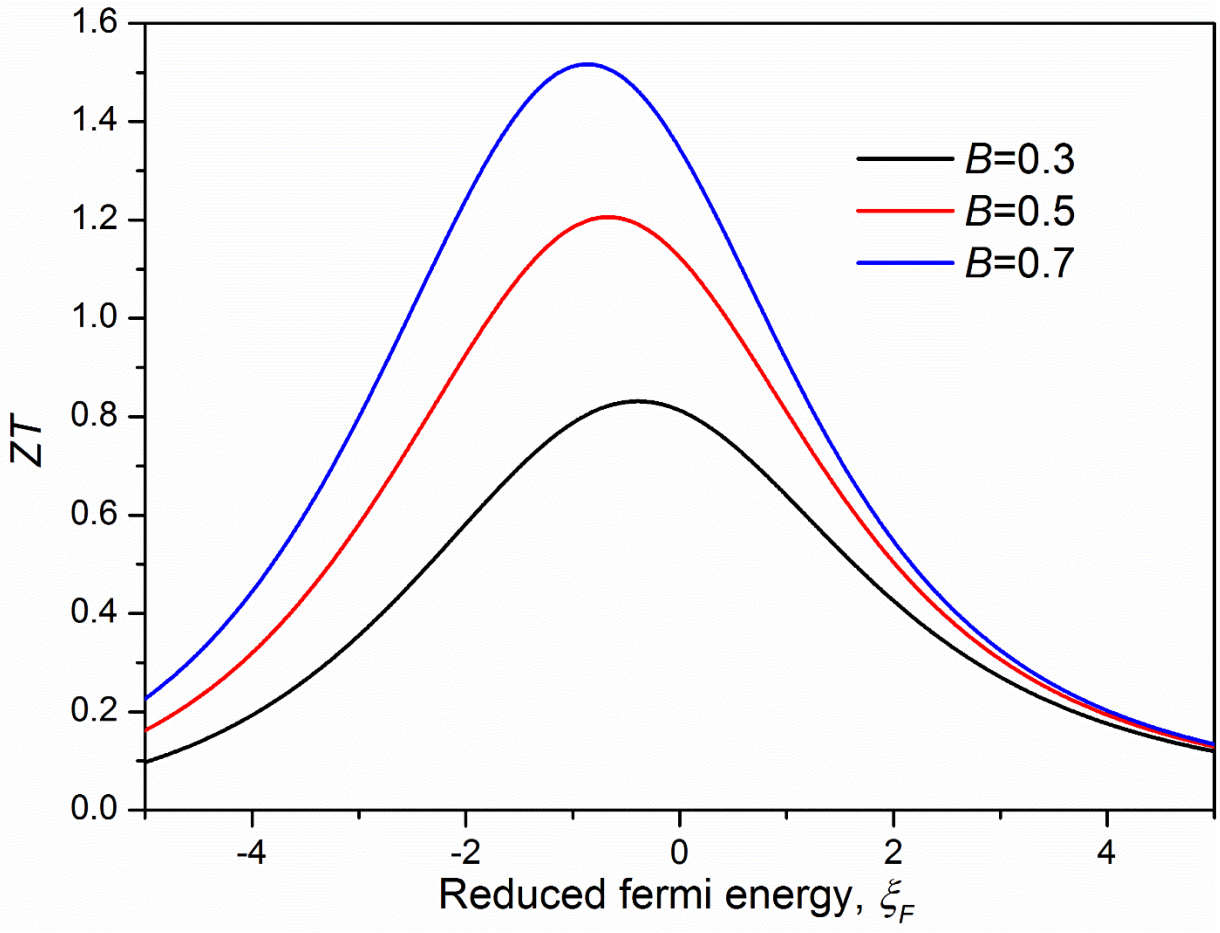

Fig. 1.10 Reduced Fermi energy dependent *ZT* as a function of *B*.

1.3 Si as an environmental-friendly thermoelectric material

As show in Fig. 1.11, high-performance Bi-Te, Pb-Te compounds and Si-Ge alloys are representative as the conventional TE materials for low-/mid-/high-temperature application, which have been intensively studied for decades. However, their use in large-scale applications is still limited by several factors such as toxicity, cost and rarity of constituent element. From a practical point of view, Si is a desirable semiconductor for most application because (a) Si constitutes about 29% by weight of the earth's crust, being the second most abundant element on Earth and rich in resource[13]; (b) the raw material (sand, i.e., quartzite) is inexpensive and (c) Si is non-toxic, i.e., environmentally safe. These characteristics of Si become more obvious when compared with Bi, Te and Pb that are main component of conventional TE materials (Table 1.4). Therefore, the strong sustainability and availability of Si-based materials may compensate its low conversion efficiency to some extent, making it an attractive TE material. Moreover, Si is widely used in semiconductor industry and one of the most extensively studied materials.

On the other hand, since most of the efficient TE materials exist in the lower temperature region and few are efficient at high temperatures, there is a need for developing high-temperature thermoelectric materials which can use high-temperature waste heat in for automobiles, electricity production and industrial sector. Typical waste heat and operating temperature ranges of various thermoelectric materials are shown in Fig. 1.12. To fulfill the industrially need of feasible TE materials, high performance TE materials must contain low cost earth abundant elements with low toxicity, which, as mentioned above, drives our attention to Si. (As for half-Heusler (HH) materials, some high-performance HH compounds also use costly precious metals such as Pd[14], or are efficient at relatively lower temperatures when compared with Si.[15])

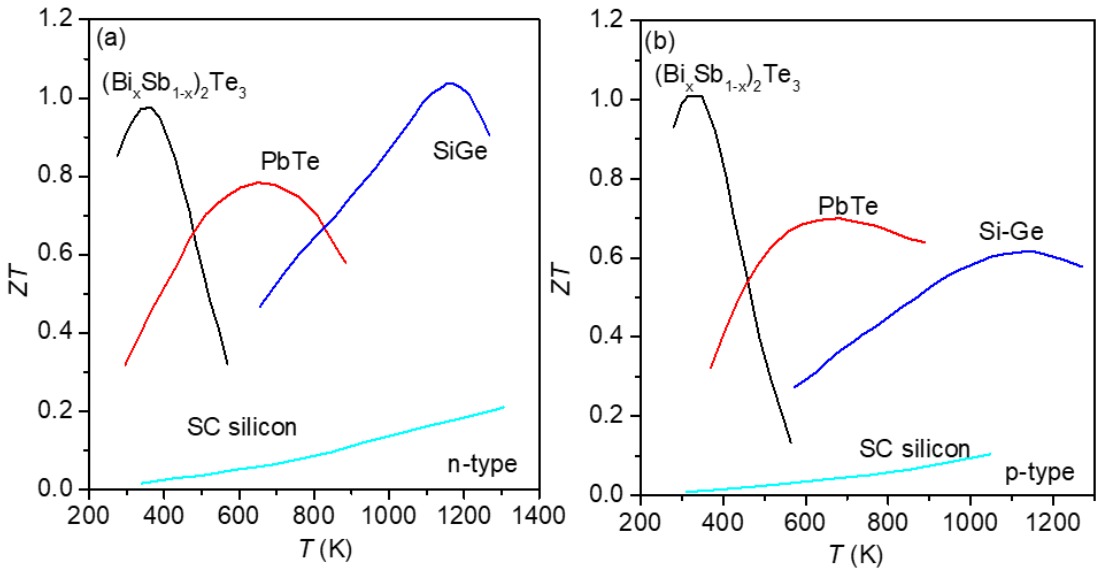

Fig. 1.11 *ZT* values for (a) n-type and (b) p-type conventional TE materials[16] and single-crystal (SC) Si (n-type: Bux et al.[17]; p-type: Ohishi et al.[18]).

Pure Si is an intrinsic semiconductor with a band gap of 1.12eV. Although its σ can be regulated by controlling the charge and number of the dopant, such as B and P, its high κ_{lat} (> 140 $W \cdot m^{-1} \cdot K^{-1}$ for nondoped Si at room temperature[19]) leads to the poor TE performance, as shown in Fig. 1.11.

It is no doubt that the most efficient way to optimize the thermoelectric properties of Si is alloying with

germanium. The substituted germanium atoms can act as strong scatter centers to lowing the thermal conductivity and contribute to a high thermoelectric figure-of-merit *ZT* ~0.9 for n-type and ~0.6 for p-type $Si_{0.8}Ge_{0.2}$ alloy[20]. In terms of sustainability and cost for Si-based thermoelectric materials, however, seeking other scattering centers which can compensate the loss of germanium-induced point defects in reducing thermal conductivity is one of the central issue for Si-based thermoelectric materials.

Table 1.4 Elemental characteristics of Bi, Te, Pb, and Si: reserves, distribution, and toxicity

Elements	Crustal abundance[13]	Reserve(t)[a]	Distribution[a]	LD_{50}[b]
Bi	85 ppb	370000	64.8% China	5,000 mg/kg
Te	5 ppb	22000	14.4% Peru	83 mg/kg
Pb	14.8 ppm	88,000,000	39.8% Australia	-
Si	28.8 %	-	-	-

[a] Mineral Commodity Summaries 2017

[b] Furuuchi chemical SDS

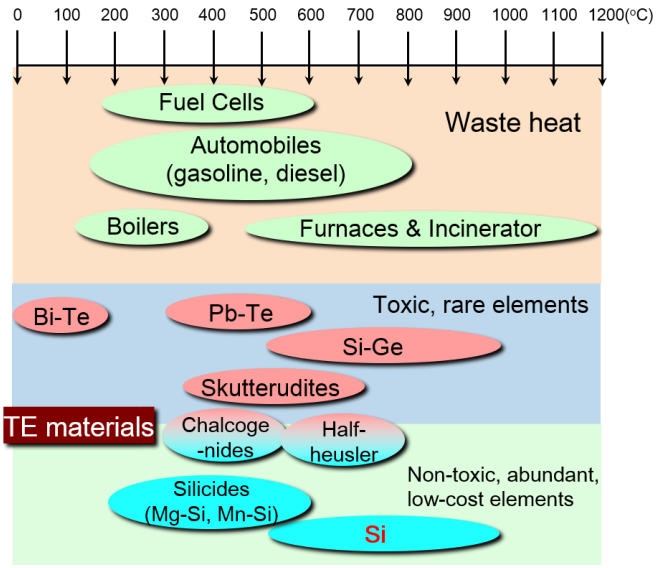

Fig. 1.12 Typical waste heat and operating temperature ranges of various thermoelectric materials[26].

With the development of nanostructure engineering technologies over past years, bulk nanostructured Si has been focused for its great potential for practical applications[21][22]. Phonons which carry a majority of heat possess average free paths in the sub-micrometer to micrometer scope[23], while the average free path of electron that are scattered at impurity atoms is a few nanometers in Si at optimal doping level[24]. Owing to the large difference of the phonon and electron mean free paths in Si, lattice thermal conductivity of Si can be reduced with maintaining high electrical conductivity when the structure of Si is controlled in nanoscale. Although *ZT* values >1 have not been obtained for the doped nanocrystalline bulk Si without alloying experimentally, it is predicted theoretically that that figure of merit *ZT* of nanocrystalline bulk Si can reach 1[25]. Therefore, there are two steps to further improve the thermoelectric performance of bulk Si: (1) optimization of carrier concentration to obtain a high power factor and (2) lowing the lattice thermal conductivity through nanostructuring.

1.3.1 Carrier concentration Optimization

Typically, the semiconductors doped degenerately with the charge carrier concentration ranging from 10^{19} to 10^{21}cm^{-3} exhibits high thermoelectric performance. The detailed band structure of material determines the ideal carrier concentration, which varies with the type of carrier because of different structures and scattering mechanisms between valence band and conduction band of material. Figure 1.13 shows the calculated thermoelectric transport coefficients of n- and p-type Si as a function of impurity concentration at 300 K based on the Boltzmann transport equation within the relaxation time approximation. Note that the power factor and *ZT* value of n-type Si is larger than that of p-type Si at same doping level. *ZT* peaks at about > 1 × 10^{21} for n-type and 5 × 10^{20} cm^{-3} for p-type, which is corresponding to 1-2 at% of dopant atoms activated electrically. These values are close to or beyond the solubility limit of the dopant atoms in crystalline Si.

Since solubility limit greatly depends on temperature and the reported data show discrepancies due to the various measurement methods and experimental difficulties such as presence of impurities and sample oxidation, it is also a challenge to work at the solubility limit of Si. Boron is a primary element for p-type doping because its solid solubility in Si is substantially greater than that of some other elements in Group IIIA. The research results of Si–B binary phase diagram show maximum solubility limit from ~3 to 3.5 at. % at the eutectic temperature, which decreased to ~1 at. % at 1200 °C sharply[27]. For n-type doping, although both phosphorus and arsenic are capable of reaching such high solubility, toxic arsenic and arsenic compounds are in contradiction to our initial interest in environmental-friendly TE material. The maximum phosphorus solubility of ~ 2.4 at% in Si has been widely used to design the n-type Si with optimized carrier concentration in many studies[28]. However, the resultant carrier concentrations are always much lower than the expected value, which are addressed to the high fraction of electrical inactive phosphorus atoms[4][21][29]. Several recent studies suggest a much lower P solubility of about 1 at% at the eutectic temperature, which is considered to be more convincing due to the utilization of high purity of the starting materials and precise characterization techniques[27][30][31]. When the solubility limit is lower than B/P concentration, other B/P atoms can form precipitates of SiP/SiB_3 phase. The influence on thermoelectric attributes will be further discussed latter.

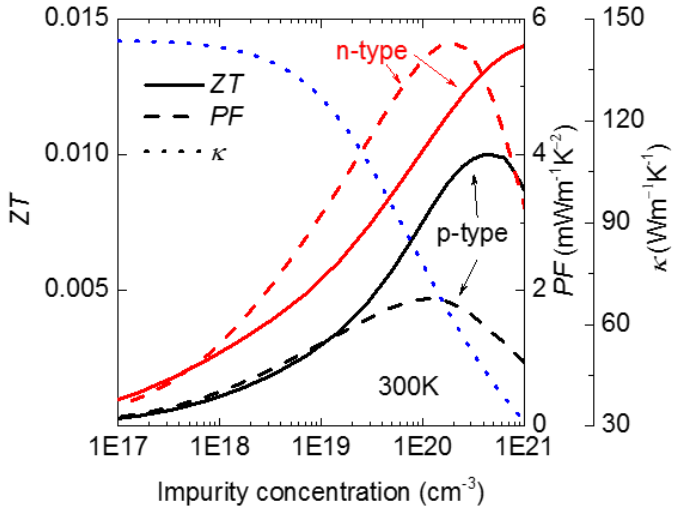

Fig. 1.13 Calculated doping concentration dependence of thermoelectric transport properties for n- and p-type Si at 300 K. The data is taken from Ohishi et al.[18]

1.3.2 Phonon scattering enhancement

It has been proved that decrease of thermal conductivity can enhance the thermoelectric efficiency of Si. Thermal conductivity has been understood comprehensively based on the research on heat transfer of a variety of materials. The dominant mechanisms of bulk Si with the ideal carrier concentration include: alloying disorder phonon scattering, charge-carrier–phonon scattering and phonon–phonon scattering. To investigate which scattering mechanism is dominant in heat transport, the spectral lattice thermal conductivity κ_s was calculated by using Born von Karman model (see the chapter 1.2.4.II. for more details):

$$\kappa_s = C \cdot \nu \cdot \Lambda \tag{1.50}$$

Where, Λ is the mean free path of phonon for individual scattering center, ν is the velocity, and C is the spectral heat capacity. The influence of scattering mechanism on phonon is estimated through single crystal Si which is doped with 1 at. % boron (assuming all the boron dopant is electrically-activated, leading to the hole concentration of ~5 $\times$ 10^{20} cm^{-3}). The contribution of phonon scattering mechanisms in spectral thermal conductivities is estimated as shown in Figure 1.14. Phonons are scattered in pure monocrystalline Si by other phonons through Umklapp scattering with the dependence of $\Lambda_U^{-1} \sim \omega^2$. A Rayleigh type scattering is shown in alloy disorder scattering because of the differences of alloying atoms in terms of size and mass, with the dependence of $\Lambda_{AD}^{-1} \sim \omega^4$. It should be noted that although alloying with germanium can create a quite strong scattering effect on high-frequency phonon in Si, alternative solute atom is limited due to the generally low solubility of other atoms in Si. Only a minor influence is exerted by boron/phosphors doping on phonon scattering due to their lower solid solubility and similar mass and size compared to Si, especially for phosphors. Carrier-phonon scattering ($\Lambda_{CP}^{-1} \sim \omega^2$) is normally regarded as the phonon scattering mechanism only effective at low temperature. Therefore, for conventional TE materials, less attention have been paid to carrier-phonon scattering. However, for bulk Si with optimal carrier concentration of over 10^{20} cm^{-3}, enhanced carrier-phonon interaction is also a critically important scattering mechanism. Liao et al. theoretically argued that 45% decrease of thermal conductivity of lattice in highly-doped Si at room temperature is resulted from carrier-phonon scattering[32]. In addition, although higher carrier concentration is corresponding to a higher electronic thermal conductivity, it is still much smaller than the lattice thermal conductivity in Si (experimental data of the electrical conductivity of heavily doped Si yields electronical thermal conductivities below 2 $W \cdot m^{-1} \cdot K^{-1}$ for carrier concentrations <10^{21} cm^{-3} by using the Wiedemann–Franz law[33]).

Based on the equation 1. 47, we can also obtain accumulative thermal conductivity as a function of phonon mean-free paths. As presented in fig. 1. 15. The thermal conductivity accumulation of Si at 300 K as a function of phonon mean-free path predicted by our models are compared with the first-principles calculation available in literature. The results considering only Umklapp process agrees quite well with the first principles calculations by Esfarjani[34] and Henry[9]. The mean free paths of phonon in Si distribute over a wide range from 1 nm to 100 microns, and phonon with a sub-nanometer mean-free path (100 nm ~ 10 μm) contribute to most of the bulk κ_{lat} (about 70%) at 300K. However, due to the strong scattering effect in heavily doped Si, the resultant phonon mean free path shift to the left side (shorter mean free path) at 300K. This tendency is also clearly enhanced at higher temperature (e.g. 1070K). Thus, phonon with a nanometer mean-free path (<100nm) will also contribute to the bulk κ_{lat} of heavily doped Si to some extent. This also should be taken under consideration for optimal design of microstructure to achieve a significant reduction in the lattice thermal conductivity.

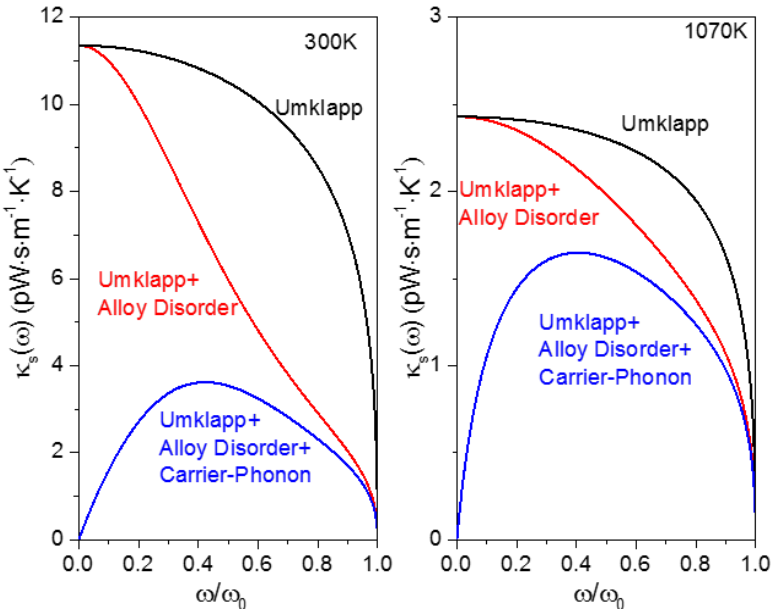

Fig. 1.14 Contribution of scattering mechanisms of phonon to spectral thermal conductivity.

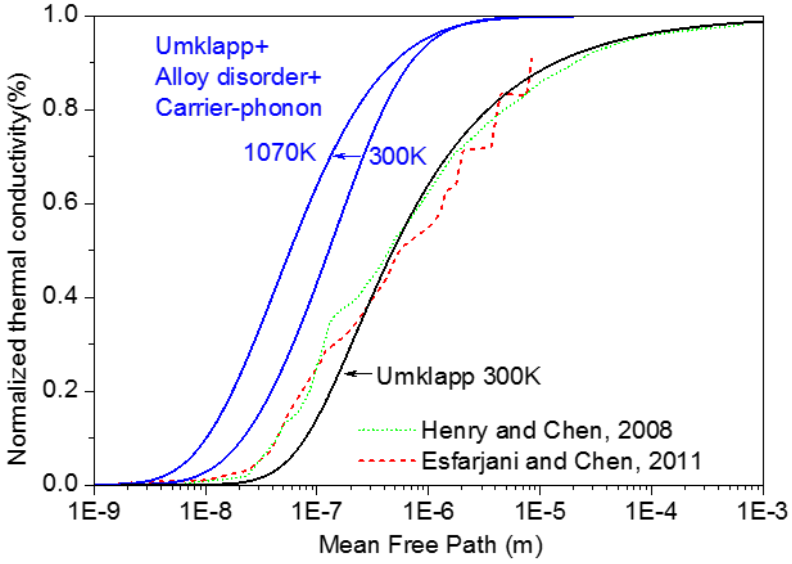

Fig. 1.15 Accumulative thermal conductivity of single crystal Si as a function of the phonon mean-free path.

I. Low-dimensional nanostructured Si

Due to the relatively long mean-free path of phonons in Si, lattice thermal conductivity can be dramatically reduced via low-dimensional nanostructuring, including nanowires, porous nanomeshes and thin-film nanocomposites, which results in a promising thermoelectric figure of merit.

High-performance Si nanowires have been presented with diameters much less than the average phonon mean free path of Si. Hochbaum et al. have successfully synthesized P-type Si nanowires whose diameters are within the range from 50nm to 115nm and reported a maximum *ZT* value of 0.6 at 300K for the Si nanowires with a diameter of 52 nm due to the large reduction in thermal conductivity[35]. Boukai et al. further achieved *ZT*~1 at 200K via Si-nanowire arrays with a width of 10 nm and a thickness of 20 nm owing to the reduction thermal conductivity and the simultaneously increased power factor by a strong quantum confinement effect[36].

Another case is Si nanomeshes containing periodic porous structures with nanoscale diameters. Tang et al. reported Si nanomeshes with 22nm in the average hole size, 55nm in spacing and 100nm in membrane thickness. These nanomeshes reduce the thermal conductivity to ~ 1.73 $W \cdot m^{-1} \cdot K^{-1}$, while retain the power factor to some degree, leading a high *ZT* ~ 0.4 at room temperature[37]. Yu et al. also showed a suppressed thermal conductivity of 1.9 $W \cdot m^{-1} \cdot K^{-1}$ for Si nanomeshes with hole sizes of 11−16 nm, spacing of 55 nm and thickness of 20 nm[38].

Thin-film nanocomposite has been also paid attention to as an attractive route for controlled thermal conductivity of Si. According to Nakamura et al.[39], the thin-film composites containing oriented nanocrystals with size of ~3 nm by Si epitaxial growth exhibited an extremely low thermal conductivity of < 1.0 $W \cdot m^{-1} \cdot K^{-1}$, which is below the amorphous limit of Si. They estimated that a high *ZT* ~ 0.2 at room temperature can be achieved if the electron concentration is further optimized. Sputtering has been also proved as an easy fabrication process for self-assembly inducing nanostructures in Si. Uchida[40][41] and Ohishi[42][43] employed targets of Si/transition metal to deposit on amorphous films followed by a subsequent thermal annealing. Among these studies, an outstanding high *ZT* of 0.22–0.42 for p-type Ni–Si nanocrystal film and 0.08–0.13 for n-type were obtained owing to improvement of carrier transport properties and reduction of the thermal conductivity in the oriented film with multi-scale nanostructures[41].

It is clear that the practical application of low-dimensional nanostructured Si is limited because it is inefficient for mass production. Still, such nanostructure engineering technologies serve to advance the understanding of basic the principles of size effect on thermoelectric transport properties, which is important for further development of Bulk nanostructured Si.

II. Bulk Si nanocrystals

Condensing nanocrystalline powders into bulk state are one of the promising route for realizing the advantages of nanostructuring while providing an easy way to scale-up. Generally, strengthening the grain boundary scattering by introducing high-density grain boundary is basic idea for nanocrystalline bulk strategy. Some theoretical studies reveals that phonon mean free path can be intensely suppressed by phonon-boundary scattering[44][45]. Grain size effect in thermal conductivity of nanocrystalline bulk are found in many thermoelectric materials[46].

Because of the long phonon mean free path of Si, the phonon transport is also demonstrated strongly influenced by the nanocrystalline nature of the bulk. The nanocrystalline nature of the bulk has been demonstrated strongly affects the phonon transport in Si due to its long mean-free path. Theoretical study has shown that nanostructuring reduces the thermal conductivity by the selective scattering of phonons as a result of a much higher density of grain boundaries and a *ZT* values as high as 1.0 were predicted for nanocrystalline Si at 1173K for a grain size of 10nm. At the time of writing, the highest *ZT* values of 0.7 at 1275 K for nanocrystalline bulk Si were reported by Bux et al. They employed a typical synthesis route where the Si nanopowder was firstly obtained by a ball-milling in a glove box under regulated atmosphere and then condensed into bulk materials with a hot processing. A finely controlled nanostructures with average crystallite size of ~ 15 nm limit the lattice thermal conductivity of heavily n-type doped Si to only 6.3 $W \cdot m^{-1} \cdot K^{-1}$ at room temperature. Similar values of the figure of merit of ~ 0.6 were later achieved by plasma-assist chemical vapor deposition method followed by a spark plasma sintering[47].

Among the above-mentioned synthesis methods for nanocrystalline bulk Si that is currently used, there are still some experimental difficulties encountered in avoiding the unfavorable oxidation of Si nanopowders and sintering-induced grain growth, which may deteriorate the overall thermoelectric performance. These features may conspire to produce great difficulties in mass-production of desirable bulk nanostructured materials. Therefore, developing methods that resolve these issues, i.e., simple and easy methods for reproducibly preparing bulk Si nanostructures with grain boundaries that do not disrupt the transport of charge carriers, is considered the most important topic for the further development of bulk, nanostructured, Si-based, TE materials.

III.Self-assembled nanocomposites

Solid phase transformations, for example, second-phase precipitation, eutectoid reaction and spinodal decomposition that can introduce two-phase interface into the bulk thermoelectric material. Because of the quick, easy and reliable preparation processing, these self-assembly methods show promising prospect as nanostructure engineering technologies for bulk thermoelectric materials.

There are theoretical models proposed to quantitatively predict how nanoparticle influences thermal conductivity. Kim et al.[48], proposed an analytical solution which is approximate for the estimation of the phonon scattering cross section of the poly-dispersed spherical nanoparticle. The theoretical study worked by Mingo et al.[10] displays whether it is possible to obviously decrease the thermal conductivity of the alloyed Si/Ge matrix under the situation of phonon scattering from the nano-silicide particle. These nano-silicide inclusions will scatter phonons preferentially over electrical charge carriers. Such nanostructuring strategy can also be employed in Si without any alloying to tune phonon dispersion to scatter the dominant phonon frequency. Figure 1.16 shows that a simplified model for the evaluation of additional phonon scattering from $CoSi_2$, $NiSi_2$, VSi_2, SiP or SiB_3 nanoparticle (see chapter 1.2.4 for details. Here, the influence on composite lattice thermal conductivity by secondary phase is neglected for simplicity). Modeling predicts a highly effective size for nanoparticle scattering is in the range of 5nm to 25nm, there is an obvious decrease when the nanoparticle size reaches 30nm. Although SiP exhibits a minor scattering effect in the order of a few nanometers because their density is quite close to that of Si, the discrepancy can be ignored for inclusion sizes larger than 5 nm, indication that the thermal conductivity mainly depends on the short-frequency scattering regimes corresponding to a high interface density.

On the other hand, in alloy (heavily doped Si), since low frequency phonons carry most of the heat in the alloy (in this case, heavily doped Si), the heat carrying phonons have MFPs longer than the nanoinclusions spacing and are thus effectively scattered by the nanoinclusions. As shown in Figure 1.17, short-frequency phonon are effectively scattered by nanoinclusions, leading to the large reduction in lattice thermal conductivity of heavily-doped Si.

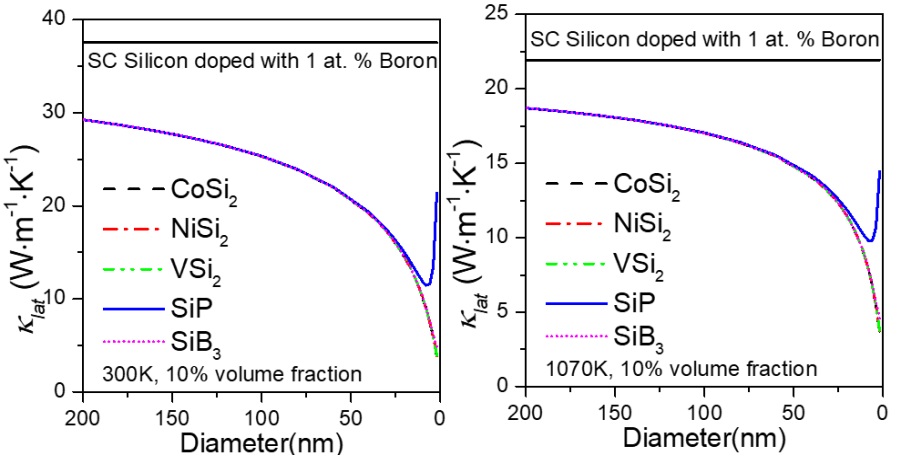

Precipitate type	ρ (10^3 kg·m^{-3})
(Si)	2.33
$CoSi_2$	4.95
VSi_2	4.62
$NiSi_2$	4.83
SiP	2.40
SiB_3	1.38

Fig. 1.16 Calculated lattice thermal conductivities of single crystalline Si doped with 1 at. % boron embed with $CoSi_2$, $NiSi_2$, VSi_2, SiP or SiB_3 nanoparticle as a function of nanoparticle diameter at (a) 300K and (b) 1070K with 10% volume fraction. The calculated thermal conductivities of heavily doped Si are indicated by the horizontal lines for comparison. The inserted table present the density of all type of inclusions calculated in (a) and (b).

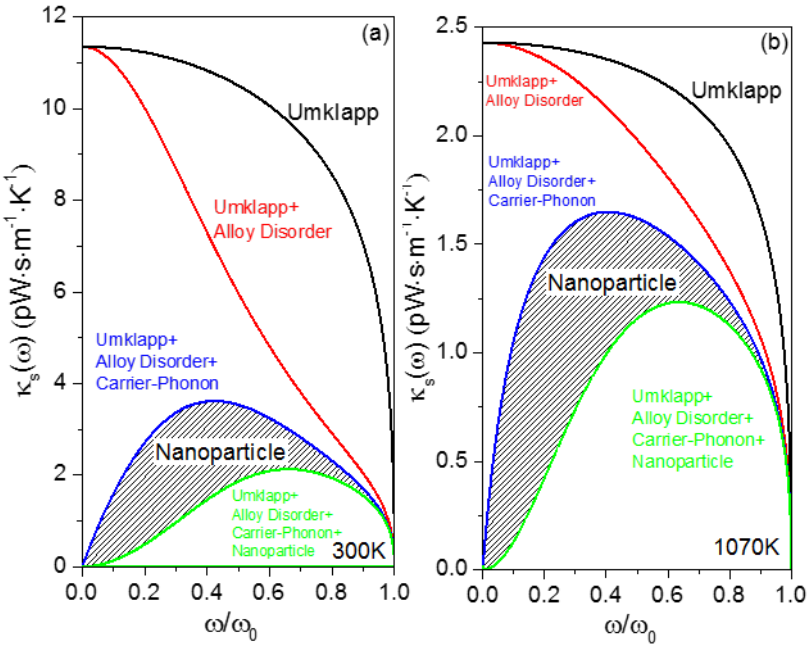

Fig. 1.17 The contribution of different phonon scattering mechanisms to the spectral thermal conductivities. The scattering effect by nanoparticle is estimated by $CoSi_2$ with a volume fraction of 10% and a size of 40 nm.

1.4 Research Objective

This thesis work aims to develop and investigate the bulk Si, which is expected to possess a large potential for high-temperature thermoelectric applications if a retention of its high electrical performance together with an enhanced phonon scattering can be achieved simultaneously. Although nanostructure engineering can be an effective way of lowering the thermal conductivity, currently used nanostructuring methods possess some experimental difficulties encountered in avoiding the unfavorable oxidation of Si nanopowders and sintering-induced grain growth, which may deteriorate the overall thermoelectric performance. Herein, development of a simple self-assembly method to introduce nanoscale structures is highly required to fabricate high-performance Si thermoelectric materials, which is however rarely investigated so far. Following this background, the specific objectives of the thesis are briefly listed as follow:

1. To get a better insight and understanding of the effect of nanostructures on the thermoelectric properties, it is necessary to develop convenient theoretical model for the prediction of fundamental thermoelectric properties for bulk Si. Since available reference on the thermoelectric properties of single-crystal Si is quite limited for high doping concentrations at high temperatures, heavily doped (10^{18}-10^{20} cm^{-3}) n-type and p-type single crystal Si will be prepared to establish a modeling of thermoelectric properties of Si.
2. To tune the microstructures in nanoscale, some critical parameters for the self-assembling approach, including phase diagram, chemical composition, solidification rate and processing route should be carefully designed and investigated in Si-based materials. The effects of these parameters on the microstructure, charge carrier and phonon transport properties targeting an optimized thermoelectric performance of self-assembled Si/Silicide composites will be focused on.
3. To develop a novel self-assembly route to introduce dislocation into Si-based materials as additional scattering centers for phonons since the effect of dislocation on thermoelectric properties and the synthesis process for dislocation formation are rarely experimentally investigated. Due the atomic scale of dislocations, detailed observations of the microstructure are also considered necessary for highlighting their impact on thermoelectric properties.
4. To further propose an outlook for the future research in Si thermoelectrics, an overall comparison of the thermoelectric transport properties of self-assembled Si/Silicide with the newly-developed theoretical model and all the available literature data for bulk Si-based thermoelectric material will be performed and discussed in the end.

To sum up, investigation of self-assembly synthesis for Si-based thermoelectric materials and improvement of thermoelectric properties of Si by introducing self-assembled microstructure are the main objectives in this dissertation. The relationship between the chapter 3, 4 and 5 is illustrated in Fig 1.18. Chapter 3 focus on the TE properties of heavily doped Si which takes Λ_U and Λ_{AD} into consideration on phonon transport, laying the groundwork for extending the model to combining other scattering mechanisms, such as Λ_{EP} for chapter 4 and Λ_{NP}, Λ_{dis} (details on dislocation-induced scattering mechanism will be given in chapter 5.1.1) for chapter 5.

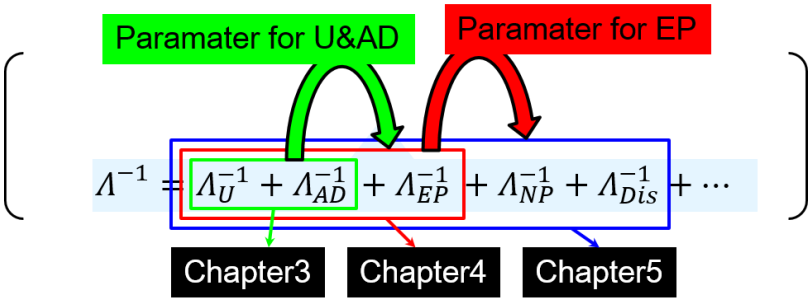

Fig. 1.18 the relationship between the chapter 3, 4 and 5 based on equation 1.47 and 1.49.

1.5 Reference

[1] A. Minnich, M. Dresselhaus, Z. Ren, G. Chen, *Energy Environ. Sci.* **2009**, *2*, 466.

[2] C. Vining, *Nat. Mater.* **2009**, *8*, 83.

[3] L. Bell, *Science* **2008**, *321*, 1457.

[4] T. Claudio, N. Stein, D. Stroppa, B. Klobes, M. Koza, P. Kudejova, N. Petermann, H. Wiggers, G. Schierning, R. Hermann, *Phys. Chem. Chem. Phys.* **2014**, 25701.

[5] T. Tritt, *Recent Trends in Thermoelectric Materials Research. I*, Elsevier, **2001**.

[6] D. Rowe, *Thermoelectrics Handbook : Macro to Nano*, CRC/Taylor & Francis, **2006**.

[7] F. D. Rosi, *Solid. State. Electron.* **1968**, *11*, 833.

[8] K. Seeger, *Semiconductor Physics : An Introduction*, Springer Berlin Heidelberg, **2004**.

[9] H. Asegun, C. Gang, *J. Comput. Theor. Nanosci.* **2008**, *5*, 1.

[10] N. Mingo, D. Hauser, N. P. Kobayashi, M. Plissonnier, a. Shakouri, *Nano Lett.* **2009**, *9*, 711.

[11] H. Xie, H. Wang, Y. Pei, C. Fu, X. Liu, G. J. Snyder, X. Zhao, T. Zhu, *Adv. Funct. Mater.* **2013**, *23*, 5123.

[12] C. Wood, *Reports Prog. Phys.* **1988**, *51*, 459.

[13] K. Hans Wedepohl, *Geochim. Cosmochim. Acta* **1995**, *59*, 1217.

[14] Q. Shen, L. Chen, T. Goto, T. Hirai, J. Yang, G. P. Meisner, C. Uher, *Appl. Phys. Lett.* **2001**, *79*, 4165.

[15] S. Populoh, M. H. Aguirre, O. C. Brunko, K. Galazka, Y. Lu, a. Weidenkaff, *Scr. Mater.* **2012**, *66*, 1073.

[16] J. Snyder, E. Toberer, *Nat. Mater.* **2008**, *7*, 105.

[17] S. Bux, R. Blair, P. Gogna, H. Lee, G. Chen, M. Dresselhaus, R. Kaner, J. Fleurial, *Adv. Funct. Mater.* **2009**, *19*, 2445.

[18] Y. Ohishi, J. Xie, Y. Miyazaki, Y. Aikebaier, H. Muta, K. Kurosaki, S. Yamanaka, N. Uchida, T. Tada, *Jpn. J. Appl. Phys.* **2015**, *54*, 71301.

[19] R. Shanks, D. Maycock, H. Sidles, C. Danielson, *Phys. Rev.* **1963**, *130*, 1743.

[20] J. Minnich, H. Lee, W. Wang, G. Joshi, S. Dresselhaus, F. Ren, G. Chen, D. Vashaee, *Phys. Rev. B* **2009**, *80*, 155327.

[21] G. Schierning, *Phys. Status Solidi* **2014**, *211*, 1235.

[22] K. Kurosaki, A. Yusufu, Y. Miyazaki, Y. Ohishi, H. Muta, S. Yamanaka, *Mater. Trans.* **2016**, *57*, 1018.

[23] K. Regner, D. Sellan, Z. Su, C. Amon, A. McGaughey, J. Malen, *Nat. Commun.* **2013**, *4*, 1640.

[24] B. Qiu, Z. Tian, A. Vallabhaneni, B. Liao, J. M. Mendoza, O. D. Restrepo, X. Ruan, G. Chen, *EPL (Europhysics Lett.* **2015**, *109*, 57006.

[25] Q. Hao, G. Zhu, G. Joshi, X. Wang, A. Minnich, Z. Ren, G. Chen, *Appl. Phys. Lett.* **2010**, *97*, 2008.

[26] M. Ohtaki, *J. Ceram. Soc. Japan* **2011**, *119*, 770.

[27] A. Mostafa, M. Medraj, *Materials (Basel).* **2017**, *10*, 676.

[28] S. Bux, R. Blair, P. Gogna, H. Lee, G. Chen, M. Dresselhaus, R. Kaner, J. Fleurial, *Adv. Funct. Mater.* **2009**, *19*, 2445.

[29] G. Schierning, R. Theissmann, N. Stein, N. Petermann, A. Becker, M. Engenhorst, V. Kessler, M. Geller, A. Beckel, H. Wiggers, R. Schmechel, *J. Appl. Phys.* **2011**, *110*, DOI 10.1063/1.3658021.

[30] S. Liang, R. Schmid, *J. Phase Equilibria Diffus.* **2014**, *35*, 24.

[31] J. Safarian, M. Tangstad, *J. Mater. Res.* **2011**, *26*, 1494.

[32] B. Liao, B. Qiu, J. Zhou, S. Huberman, K. Esfarjani, G. Chen, *Phys. Rev. Lett.* **2015**, *114*, 1.

[33] G. Masetti, M. Severi, S. Solmi, *IEEE Trans. Electron Devices* **1983**, *30*, 764.

[34] K. Esfarjani, G. Chen, H. T. Stokes, *Phys. Rev. B* **2011**, *84*, 85204.

[35] H. Allon, C. Renkun, D. Raul, L. Wenjie, G. Erik, N. Mark, M. Arun, Y. Peidong, *Nature* **2008**, *451*, 163.

[36] A. Boukai, Y. Bunimovich, J. Tahir, J. Yu, W. Goddard, J. Heath, *Nature* **2008**, *451*, 168.

[37] T. Jinyao, W. Hung-Ta, L. Dong Hyun, F. Melissa, H. Ziyang, R. Thomas, Y. Peidong, *Nano Lett.* **2010**, *10*, 4279.

[38] J. Yu, S. Mitrovic, D. Tham, J. Varghese, J. Heath, *Nat. Nanotechnol.* **2010**, *5*, 718.

[39] Y. Nakamura, M. Isogawa, T. Ueda, S. Yamasaka, H. Matsui, J. Kikkawa, S. Ikeuchi, T. Oyake, T. Hori, J. Shiomi, A. Sakai, *Nano Energy* **2015**, *12*, 845.

[40] N. Uchida, T. Tada, Y. Ohishi, Y. Miyazaki, K. Kurosaki, S. Yamanaka, *J. Appl. Phys.* **2013**, *114*, 134311.

[41] N. Uchida, Y. Ohishi, Y. Miyazaki, K. Kurosaki, S. Yamanaka, T. Tada, *Mater. Trans.* **2016**, *57*, 1076.

[42] Y. Ohishi, Y. Miyazaki, H. Muta, K. Kurosaki, S. Yamanaka, N. Uchida, T. Tada, *J. Electron. Mater.* **2015**, *44*, 2074.

[43] Y. Ohishi, K. Kurosaki, T. Suzuki, H. Muta, S. Yamanaka, N. Uchida, T. Tada, T. Kanayama, *Thin Solid Films* **2013**, *534*, 238.

[44] L. Yang, A. J. Minnich, *Sci. Rep.* **2017**, *7*, 1.

[45] C. Hua, A. J. Minnich, *Semicond. Sci. Technol.* **2014**, *29*, 124004.

[46] Y. Lan, A. J. Minnich, G. Chen, Z. Ren, *Adv. Funct. Mater.* **2010**, *20*, 357.

[47] J. Shiomi, *APL Mater.* **2016**, *4*, 104504.

[48] W. Kim, A. Majumdar, *J. Appl. Phys.* **2006**, *99*, 84306.

2. Experimental technique

2.1 Melt spinning technique

Melt spinning serves as the key for many advanced functional materials. It is a rapid solidification technique. As shown from Fig. 2.1, small quantity of alloy has melted through levitation methods or inside a crucible in the typical laboratory melt spinner. Afterward, it would be ejected through pressurization via a fine nozzle over the fast-rotating copper wheel. Each of such parameters would be controlled carefully and hence to obtain the desired thickness, shape and size of the ribbon. The crucible material is selected according to its low porosity, thermal conductivity, resistance to thermal shock and chemical compatibility. In the cross section, the nozzles are typically circular, which ranges from 50 to 1250 um. They are made by refractory materials. The exact nature of these nozzles relies on the type of metal to be processed while the ejection pressure relies intensively on the desired melt delivery rate. Desired melt delivery rate is of great importance for the election pressure. The adoption of higher ejection pressure leads to the development of the wetting pattern and hence would have better thermal contact between the substrate and melt puddle. When the nozzle diameter decrease, there would be an increase of the required ejection pressure. Typically, the solidification rates would be ~100m/s. Transforming the melt to the amorphous structure has been made possible due to the high solidification rates.

Table 2.1 The parameters of the melt spinning utilized in this study

Roll speed	21m/s, 42m/s, 63m/s
Protective gas	Ar
Ambient pressure	0.086MPa
Injection pressure	0.005MPa
Distance between roll and nozzle	0.20mm
Nozzle type	BN
Diameter of Nozzle	0.4mm

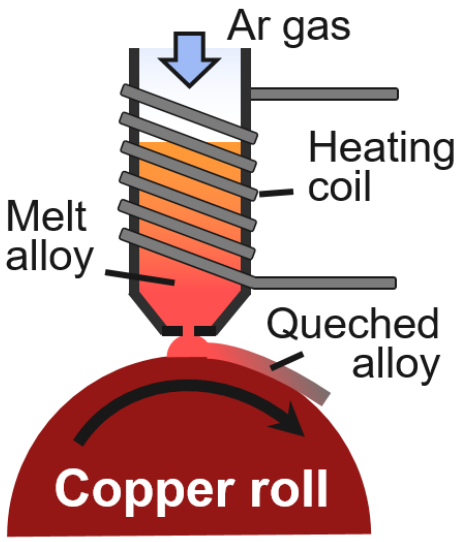

Fig. 2.1 Schematic illustration of melt spinning.

2.2 Spark Plasma Sintering

Spark plasma sintering (SPS), as a technique, takes advantages of electrical current to charge the space between powders and, meanwhile, puts high pressure into use. By contrast, SPS is more advantageous than the following methods, such as hot-pressing (HP) and hot isostatic pressing (HIP) because of its strengths that contain rapid sintering, fewer sintering additives and uniform sintering in simple operation. The SPS process is demonstrated by a schematic diagram in Fig. 2.2(a). The die is utilized to hold the powder, the whole of which, then, is under a constant load with a pulsed direct current. Moreover the current flows in resistance paths that are formed by the space between powders. Inside, the powder is heated by the energy from resistance points, which is a high-efficiency approach. It is possible to appear electrical breakdown, leading to skin current. As shown by Fig. 2.2(b), there is a schematic which displays current paths in powder samples. What's more, in Fig. 2.2(c), it can be found that SPS is utilized to connect Si wafers. Applying alternating current leads to the appearance of capacitors created by air pockets between particles. At the same time, with the help of electrical discharge, these gaps also generate plasmas. To gain a well-proportioned sample, it is necessary to control its temperature gradient in a lower level. Resistance heating is the heating way, so the material electrical conductivity is vital. The operation also utilized graphite paper to isolate powders from graphite punches. Besides, for excellent electrical contact between parts, other graphite parts are put into utilization.

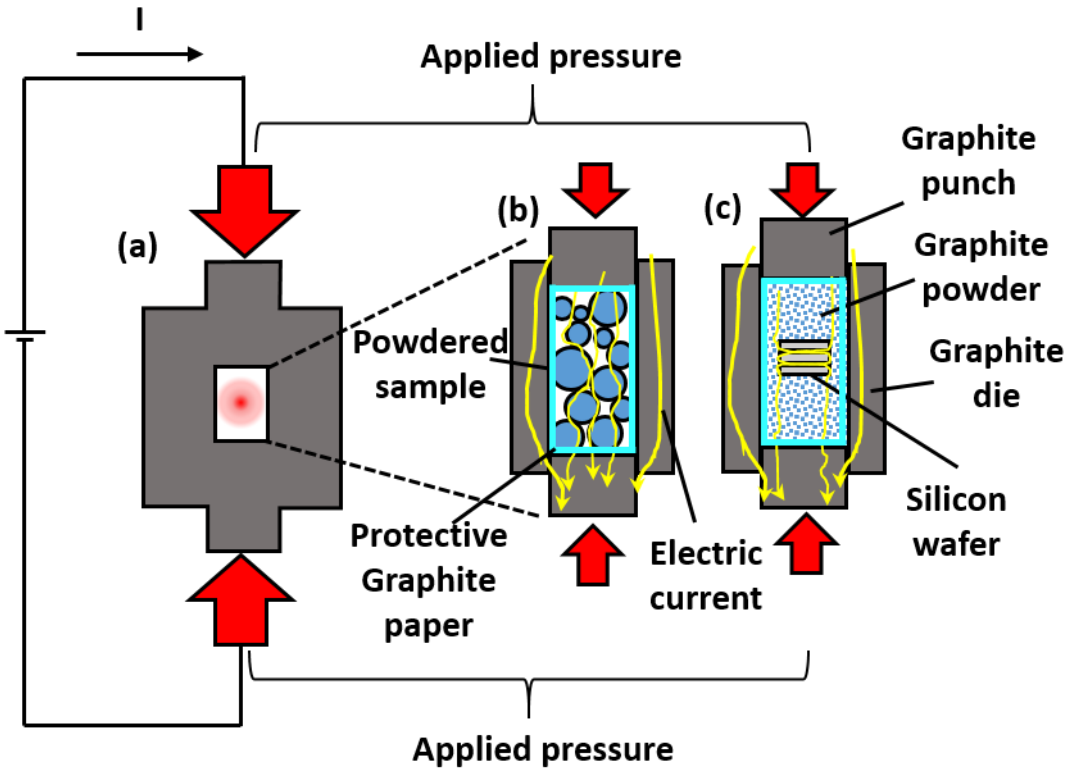

Fig. 2.2 Schematic illustration of (a) spark plasma sintering, (b) resistance heating of powdered sample and (c) resistance heating of Si wafer.

2.3 Measurement of Thermal Conductivity

With the distribution of temperature changing, there is a trouble that heat transfer is short. Thermal diffusivity is a concept that the fundamental quantity makes the entrance into the heat transfer situation that is unsteady. There is a formula with the relation to the steady-state thermal conductivity.

$$\kappa = dCD, \tag{2.1}$$

where D is the thermal diffusivity, C the specific heat and d the sample density. In this equation, it can be found that *D*, thermal diffusivity, can help to compute κ (thermal conductivity). To obtain the value of *D*, the experiment has to use a laser flash in Netzsch LFA457 instrument. In addition, *D* is to judge the speed of the body changing temperature. For the purpose of measure a material's thermal diffusivity, it is demanded to heat one side of the sample and to measure the temperature trend of the other side.

It needs a period of time to heat the sample and increase temperature on the rear surface. This time is useful for the measurement of the through-plane diffusivity and the calculation of the through-plane thermal conductivity under the given specific heat and density. Figure.1 makes a particular description of the through-plane measurement.

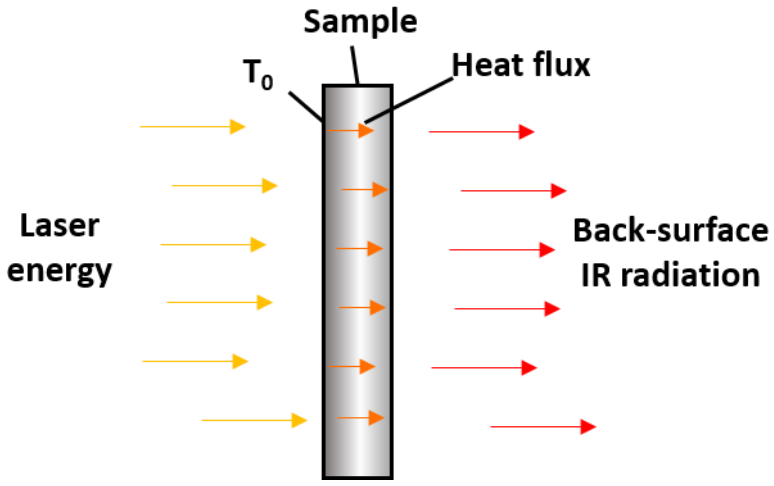

Fig. 2.3 Schematic illustration of through-plane measurement.

Figure 2.3 describes the basic way used in this paper. The experiment takes a disk as a sample which is 12.7 mm in diameter, a standard one, and has a thickness range within 1mm to 3 mm. The Netzsch LFA457 Laser Flash system makes the disk aligned in a tantalum tube furnace, namely the position between a neodymium glass laser and an indium antimonite (lnSb) IR detector. If a thermocouple touches the disk, it will control the disk as well as its surroundings when temperature changes within the range of 300K to 1273K. When there is a stable state on the condition that the sample reaches to the expected temperature, the laser, within a few minutes, shoots several times over a span, and, at the same time, an instrument records relative data of each laser "shot". The laser beam shoots energy which the front surface of the sample assimilates, thus, a heat pulse goes through sample thickness. In addition, the increase of temperature is next to nothing. The temperature is in the most ideal range, which is beneficial from adjustable filters between the laser and the furnace. It can be found that the back surface of the sample is focused by a lens onto the detector. Besides, there is an amplified trend of the temperature rise signal vs. time, which is recorded by a high speed AID converter. In Figure 2.4, it provides an illustration of a temperature rise curve in practice.

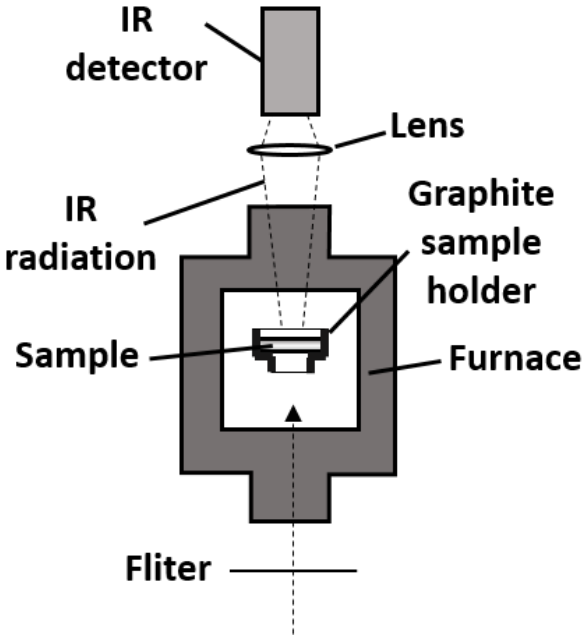

Fig. 2.4 Schematic illustration of laser flash instrument.

This paper carries out a test in an environment filled with argon gas. The equipment is completely automated so that it can command systems. Moreover, it also records, analyzes and reports thermal diffusivity and specific heat, calculating thermal conductivity.

Before test, a graphite film is utilized to cover the sample without a naturally high value of emissivity or absorptivity. As a result, graphite enhances not only the energy that the laser side absorbs but also the temperature of the sample backside.

Figure 2.5 describes a through-plane measurement where the sample is regarded as a part of the material sheet, which is infinite in two dimensions but finite in thickness. Prior to flash, sample temperature is the same to surroundings temperature so that the temperature can be set as zero. However, there is a higher temperature (T_0) on the sample front surface after flash. What's more, the heat flux lines which are parallel directly pass through the sample, while in the sample plane is no heat flow. At the beginning, when the temperature is 0, the radiation heat that forms boundary conditions moves from the front and rear faces to a surrounding space. The heat equation problem of the boundary initial value can be handled with from different perspectives. Parker et al. take the lead in putting the solution to measure flash diffusivity in practice[1]. On basis of Koski's notation[2], there is a resulting equation of the temperature on the sample rear surface as follows:

$$T(a,t) = 2T_f \sum_{n=1}^{\infty} \frac{{\gamma_n}^2 (L^2 + {\gamma_n}^2) \cos \gamma_n}{{\gamma_n}^2 + L^2 + 2L} e^{\frac{-\gamma_n^2 Dt}{a^2}} \tag{2.2}$$

where

T_f Final sample temperature

D Thermal diffusivity

t Time

a Sample thickness

L Heat loss factor

The following transcendental equation is used to calculate γ_n:

$$\tan \gamma_n = \frac{2\gamma_n L}{{\gamma_n}^2 - L} \tag{2.3}$$

The heating on the front surface is not regarded as instantaneous with respect to the time when the heat diffuses through the sample. Thus, measuring the thin and/or high diffusivity sample can be impacted by the finite width of laser pulse. To analyze the influence, the convoluting formula (2.2) with the pulse shape folds the width of laser pulse. Without heat loss, namely L=O, the finite pulse can be neglected. The Parker expression can be obtained in the light of equation (2.4):

$$\alpha = 0.1388 \frac{d^2}{t_{\frac{1}{2}}} \tag{2.4}$$

$t_{\frac{1}{2}}$ is named as the half rise time, which means the time when the temperature on the back surface temperature reaches to 50% of the highest. Under the condition that diffusivity is approximately known, Equation (2.4) can calculate the optimum thickness and the expected rise time of the sample so that it is a very useful expression.

This paper uses the Cowan method to analyze the obtained data. As a result, the data from the sample, in practice, are not completely in accordance with the results offered by the theoretical analysis, while there will be results which ideally agree with them through the Cowan method. It is demanded to depict the time curve, analyzed, and compare the theoretical curve with the steady diffusivity, which should be finished after every shot of laser.

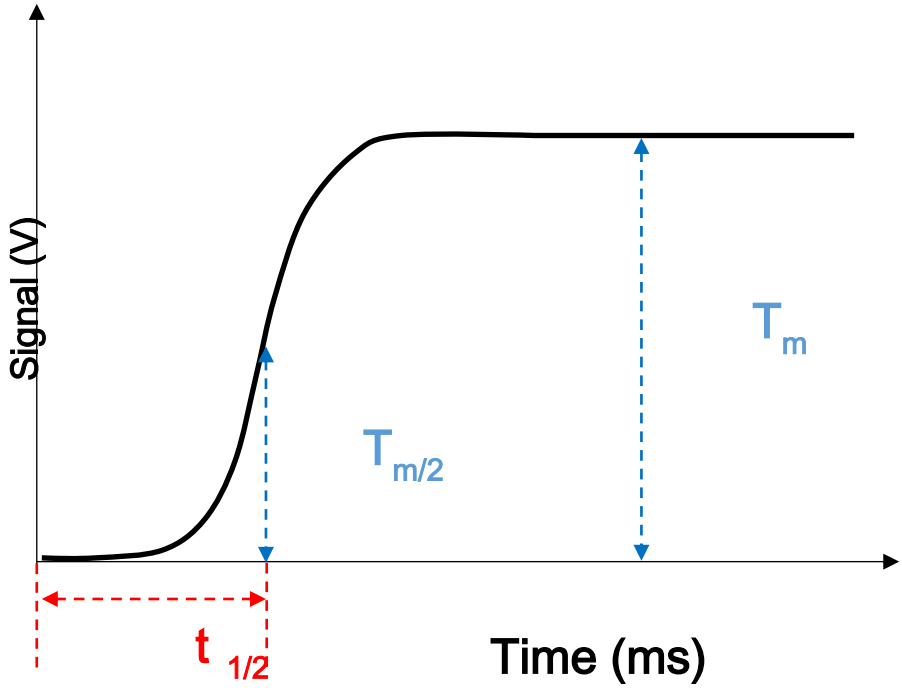

Fig. 2.5 Dimensionless plot of rear surface temperature history.

2.4 Hall Effect Measurement

n ($n_H \approx 10^{-17}$-10^{-20} cm^{-3}) represents the range of carrier concentrations used for the typical optimization of the power factor of thermoelectric materials. Therefore, Hall effect measurement plays an important role in measuring carrier concentration.

In this thesis, the Hall effect/resistivity measurement system ResiTest-8340 (TOYO Corp.) measures samples' Hall coefficients and resistivity values when it is at room temperature and the magnetic field is 0.5T. Next, this paper measures samples' Hall carrier concentrations and Hall carrier mobility values. In addition, in Fig. 2.6 is the schematic diagram of the Vander Pauw measurement. The following is a primary equation used to measure Hall coefficient[3]:

$$\mathrm{R}_H = \frac{V_H t}{IB} \tag{2.5}$$

In this equation, V_H means potential difference between two Hall probes. B indicates the magnetic field in application. R_r points variable resistor which can cancel the voltage from one Hall probe to another prior to the application of magnetic field. In a simple, the magnetic field direction is perpendicular to where the electric current flows, thus, across the simple is potential V_H. At the same time, V_H is perpendicular to the direction of both magnetic field and current flow. On basis of the following equation, hall coefficient can be calculated:

$$R_H = R_r \frac{V_H t}{V_s B} \tag{2.6}$$

The following equation connects n (carrier concentration) and μ (mobility):

$$n_{\mathrm{H}} = \frac{\gamma_{\mathrm{H}}}{eR_{\mathrm{H}}} \tag{2.7}$$

$$\rho = \frac{1}{en\mu_{\mathrm{H}}} \tag{2.8}$$

γ_{H} means Hall factor. It is a variable that changes with *s*- the carrier scattering parameter- and degeneracy degree changing. $\gamma_{\mathrm{H}} = 1$, when acoustic phonon scattering is degenerate. Moreover, $\gamma_{\mathrm{H}} = 3\pi/8$, when acoustic phonon scattering is nondegenerate. This paper takes advantage of the Vander Pauw measurement to gain R_H, Hall coefficient, as follows:

$$R_H = \frac{t}{B}\Delta R_{BD,\ AC} \tag{2.9}$$

In this equation, if *B*, magnetic field, is used in practice, $\Delta R_{BD,\ AC}$ indicates the variation in potential.

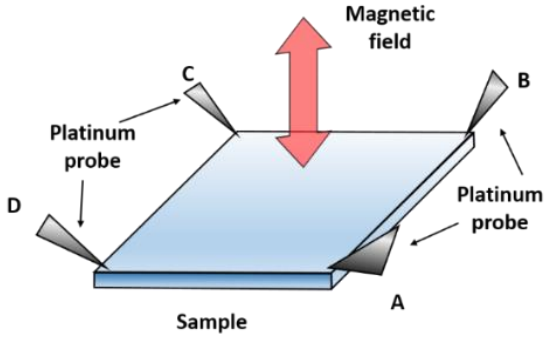

Fig. 2.6 Schematic illustration of the Vander Pauw method.

2.5 Electrical resistivity and Seebeck coefficient

Through the four-point approach, there is an equation to calculate electrical resistivity as follows:[4]

$$\rho = \frac{1}{\sigma} = \frac{A}{I}\frac{\Delta V}{\Delta x} \tag{2.10}$$

The operation of this approach is to put four probes at some intervals that are equidistant. As shown in Fig. 2.7, when there is current flowing between two probes, the distance between which is the outmost, between two internal probes appears a decreasing trend of voltage. To gain electrical resistivity *R*, this paper takes advantage of Ohm's law as the following:

$$\rho = \frac{A\Delta V}{I\Delta x} \tag{2.11}$$

In this equation, $\frac{\Delta V}{\Delta x}$ means potential gradient along current direction. A points the cross-sectional area. Meanwhile, I indicates current flowing in the sample. Fig. 2.7 also shows an equation to calculate ΔV the voltage between current electrodes:

$$\Delta V = \frac{V_s}{R_s} \tag{2.12}$$

V_s represents reduced voltage and ρ_s implies resistivity, both of which are between current electrodes. After the measurement of rectangular sample, there is an improved formula

$$\rho = \rho_s \frac{V_r bt}{V_s L} = \frac{A\Delta V}{IL} \tag{2.13}$$

The parameters above all exist between current electrodes. They are respectively b- width, t- thickness and L- length of the sample.

Under the comparison with the similar two-point probe method, the four-point probe method is more accurate than because of separate current and voltage probe.[4] There is an obvious example that the variation of current direction can cause the neglect of contact resistivity and electromotive in semiconductor or metal. There is a method to avoid: electrical current going through the sample in a short pulse. Therefore, there are only two factors which can decide the measurement of accuracy: geometry and homogeneous property. On the consideration of variety of research materials in the aspects of geometry and contact resistivity, it will be longer for potentiometric arrangement and lower in the cross-sectional area of specimen.

In terms of the Seebeck effect, a conductor's electric potential emergently changes in a thermal gradient. Equation (2.14) shows how the Seebeck coefficient is calculated as follows:

$$S_{ab} = \frac{\Delta V}{T_H - T_L} \tag{2.14}$$

Fig. 2.7 shows that in a furnace is a measuring arrangement, and there is a heater contained in the lower electrode block. The sample is heated to the setup temperature by the furnace which surrounds the measuring arrangement. When it reaches to the required temperature, there will appear a temperature gradient in the lower electrode block. Then, $\Delta T = T_H - T_L$, the temperature gradient, will be tested by double thermocouples that contact with each other.

However, Fig. 2.8 demonstrated that if the Seebeck coefficient doesn't rely on temperature when ΔT is big, a problem will appear despite of bigger ΔT and raiser measurement.

This paper has chosen the ΔT values of 20K, 30K and 40K for the measurement of the Seebeck effect, because it is universally acknowledged that it is dependent. T_H is higher than T_L for 5K, thus the measurement takes the mean of them as the experimental temperature.

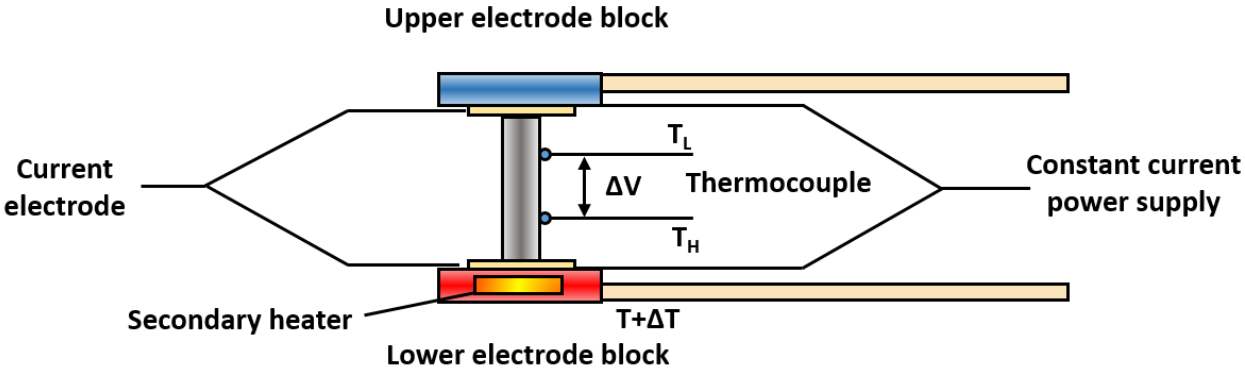

Fig. 2.7 Schematic illustration of electrical resistivity and the Seebeck coefficient measurement

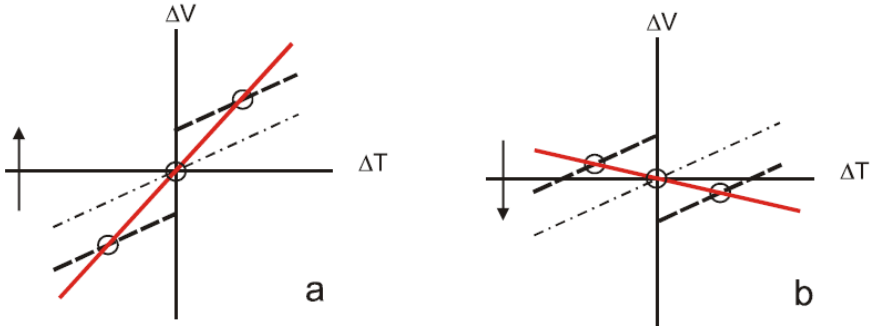

Fig. 2.8 Possible effects of the contact potential ($S_{ab} = \Delta V/\Delta T$ from measurements at two temperatures) (a) positive contact potential; (b) negative contact potential. Circles in accordance to the measured data; arrow to contact potential; broken lines to the Seebeck effect and dash-dotted line to the true Seebeck measurement that contact potential has no effect on[4]

2.6 X-ray Diffraction Methods

XRD analysis, namely X-ray diffraction analysis, has been used to conduct the phase characterization in the air under the room temperature. Cu Kα radiation is used in this process. Milling part of the bulk sample can generate the powder of the sample while electrons are used to produce characteristic X-rays in the X-ray tube. The kinetic energy of the electrons excited the electrons in the target. Afterward, the excited electrons would back to the low energy state. Crystallographic planes would diffract the X-ray beams incident over the crystalline solid, which is as shown in Fig. 2.9. Unless the relationship in below is satisfied, otherwise, the deflected waves would not be in the phase.

$$2d \sin\theta = \mathrm{n}\lambda \tag{2.15}$$

Equation (2.15) serves as the basic diffraction law, which is also called as Bragg's law. In this equation, n represents the integral number while λ = 0.15418 nm refers to the wavelength of the X-ray. "θ" represents diffraction angle and "d" represents the distance of planes.

Combing the least square method and Cohen's method[5], it can be used to predict the lattice parameters of the samples based on the Powder X-ray Diffraction Data. Through the logarithms and Bragg's equation, we can obtain:

$$\ln \sin^2\theta = \ln\left(\frac{\lambda^2}{4}\right) - 2\ln d \tag{2.16}$$

Differentiating equation (2.16) gives

$$\frac{\Delta \sin^2\theta}{\sin^2\theta} = -\frac{2\Delta d}{d} \tag{2.17}$$

Take combined systematic errors into account, we can obtain

$$\frac{\Delta d}{d} = K\cos^2\theta \tag{2.18}$$

Then combining equation (2.17) and equation (2.18) gives

$$\Delta \sin^2\theta = 2K\Delta \sin^2\theta \cos^2\theta = D\sin^2\theta \tag{2.19}$$

where D is a new constant. The true value of $\sin^2\theta$ for any diffraction is

$$\sin^2\theta\,(true) = \frac{\lambda^2}{4a_0}(h^2 + k^2 + l^2) \tag{2.20}$$

where a_0 is the true value of the lattice constant. But

$$\sin^2\theta\,(observed) - \sin^2\theta\,(true) = \Delta\sin^2\theta \tag{2.21}$$

$$\sin^2\theta\,(observed) - \frac{\lambda^2}{4a_0}(h^2 + k^2 + l^2) = D\sin^2\theta \tag{2.22}$$

or

$$\sin^2\theta\,(observed) = A\alpha + C\delta \tag{2.23}$$

where

$$A = \frac{\lambda^2}{4a_0} \tag{2.24}$$

$$\alpha = (h^2 + k^2 + l^2) \tag{2.25}$$

$$C = \frac{D}{10} \tag{2.26}$$

$$\delta = 10 \sin^2 2\theta \tag{2.27}$$

In this equation, D refers to the drift constant while Best precision has been achieved when D is in its minimal value. Equation (2.22) is presented each reflection in the x-ray diffraction pattern. Based on the theory of square of least squares, the best values of coefficients C and A refer to those whose total value of the square of the random observational errors reach to its minimum.

$$\sum (e)^2 = a\ minimum = \sum [A\alpha + C\delta - \sin^2\theta\ (observed)]^2 \tag{2.28}$$

Differentiating equation (2.28) can generate a pair of normal equation when A and C equal to zero. Therefore,

$$\sum \alpha \sin^2\theta = A\sum \alpha^2 + C\sum \alpha^2\delta \tag{2.29}$$

$$\sum \delta \sin^2\theta = A\sum \alpha\delta + C\sum \delta^2 \tag{2.30}$$

The true lattice parameter a_0 can be determined based on the value of A, which is obtained through the equations above.

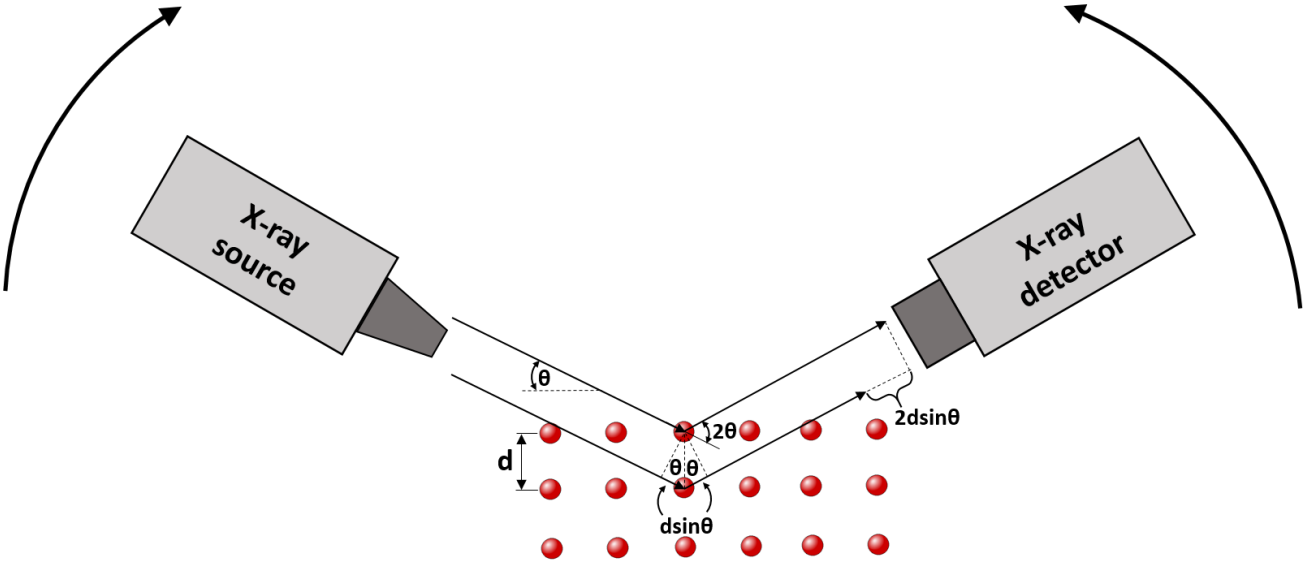

Fig. 2.9 Schematic illustration of X-ray diffraction method.

2.7 Field emission scanning electron microscopy

With the help of FE-SEM (the Field Emission Scanning Electron Microscopy), the experiment can examine the surface of the ingot sample. Additionally, SEM images are gained by JSM-6500F (JEOL Ltd.) microscope.

Through SEM, an electron beam can be generated in virtue of an electron gun and multiple condenser lenses. In the 1st batch of electromagnetic scan coils, beam rays can be shown from different angles. However, the beam can be shifted back by 2nd batch of scan coils, which is across the optic axis. Finally, there is no one exception of rays that misses final lens' aperture and all of them come to the simple on different positions at a same time. The followings are some signals marking the end: high-energy back scattered electrons, secondary and backscattered electrons with low energy, X-rays and luminescent radiation which is UV, visible or infrared. In virtue of a scanning electron image detector, it is not difficult to get scanning electron micrographs and energy dispersive X-ray spectra. In Fig. 2.10 is the schematic diagram of SEM.[6]

In FE-SEM, the electron gun applies a cathode of field emission to take place of a filament. Besides, the cathode not only offers narrower probing beams but also provides high electron energy, which leads to the optimized spatial resolution.

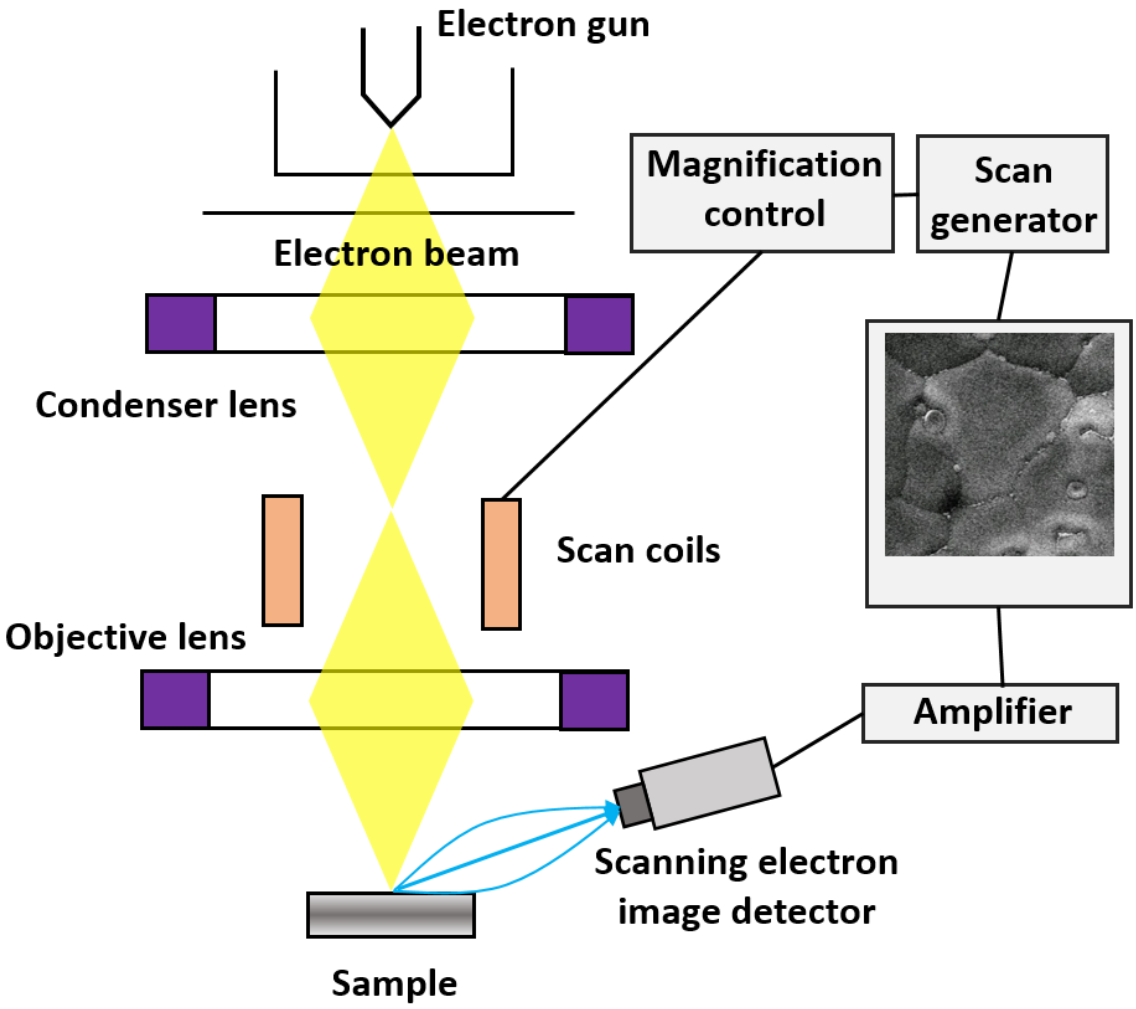

Fig. 2.10 Schematic illustration of SEM apparatus.

2.8 Electron backscatter diffraction

Electron backscatter diffraction operates through the arrangement of the highly polished flat sample in a shallow angle to the incident beam of electrons (Fig. 2.11). The free port over the SEM chamber has been attached with EBSP detector. In the ideal condition, the free port should be orthogonal to the stage tilt axis when the samples might be tilted easily to the detector at ~70˚, even though there are other possible orientations. The crystal lattice low energy loss backscattered electrons were later channeled when interacts with the primary beam. An electron EBSP would be formed through the network of diffraction lines. Intersecting bands would lead to bright spots on EBSD. Therefore, the EBSDs can recognize the elements of symmetry. [7]

EBSD maps can be adopted to deliver the microstructure of the material with 2D information regarding the shape and size of the grain visually as with the optical imaging techniques and conventional SEM. However, as it has already known the orientation and phase at each pixel, EBSD data analysis software then can lead to many types of analytical and visual information, including grain size distribution and pole figure, which are as shown in Fig. 2.12.

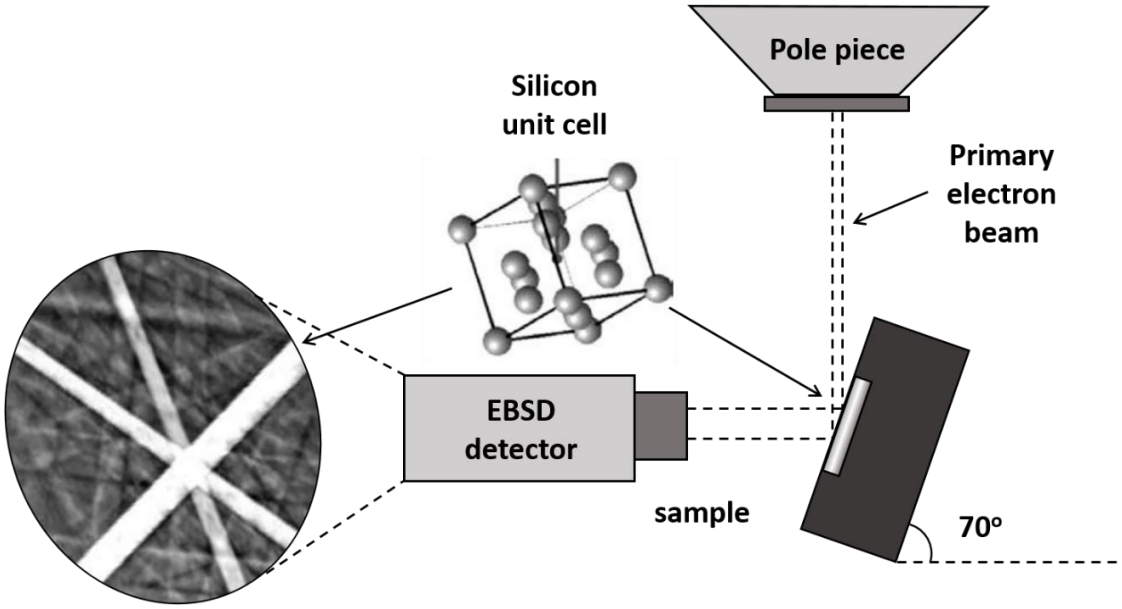

Fig. 2.11 Schematic illustration of electron backscatter diffraction.

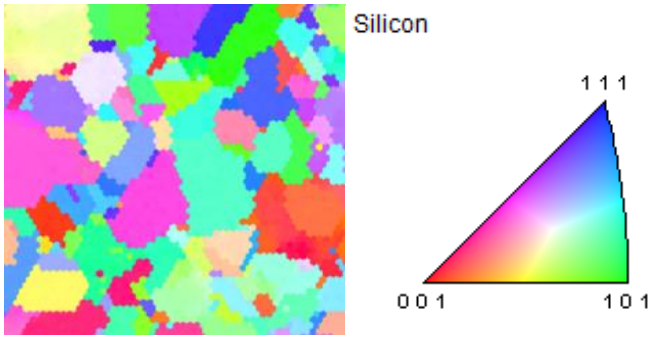

Fig. 2.12 Schematic illustration of electron backscatter diffraction.

2.9 Transmission electron microscopy

Transmission Electron Microscopy (TEM) is employed to image a thin region of planar sample from the transmitted electrons. Interactions between electron and various areas planar the planar sample result in the formation of contrast in the TEM image, which can be attribute to different crystal structure, phase and/or orientation. Schematic diagram of TEM is shown in Fig. 2.13. For atomic-scale defect like nanodots, dislocations, stacking fault and strain fields, high resolution TEM (HRTEM) is employ to obtain detailed structural information, which is closely related to the resultant thermoelectric properties. The elemental analysis or chemical characterization data can also be obtained by TEM with an energy dispersive X-ray spectroscope (EDS).

For planar TEM sample preparation, we cut the sample into 2 mm × 1mm then using mechanical polishing to ~ 100 μm followed by subsequent ion beam milling to ~ 100 nm using the JEOL EM-09100 IS as presented in Fig. 2.14

.

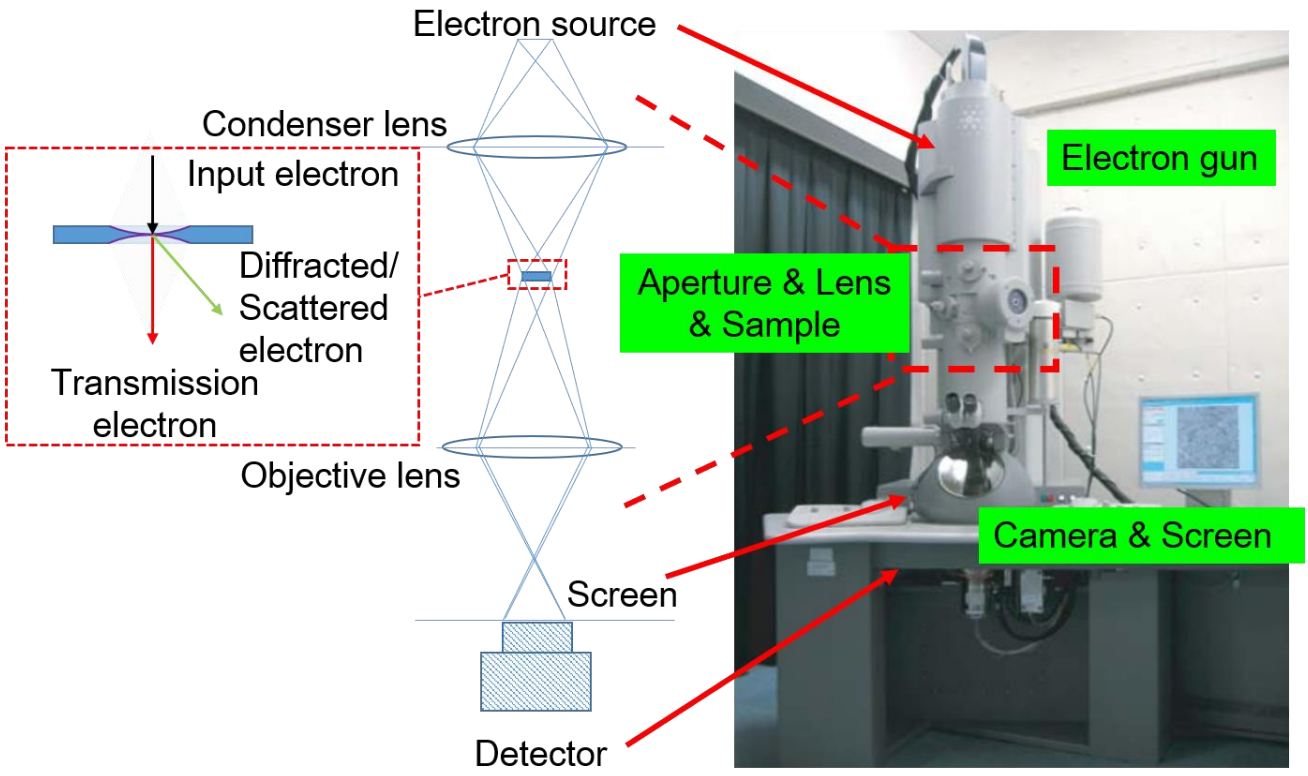

Fig. 2.14 Schematic diagram of TEM (model: FEI Tecnai G2 F20).

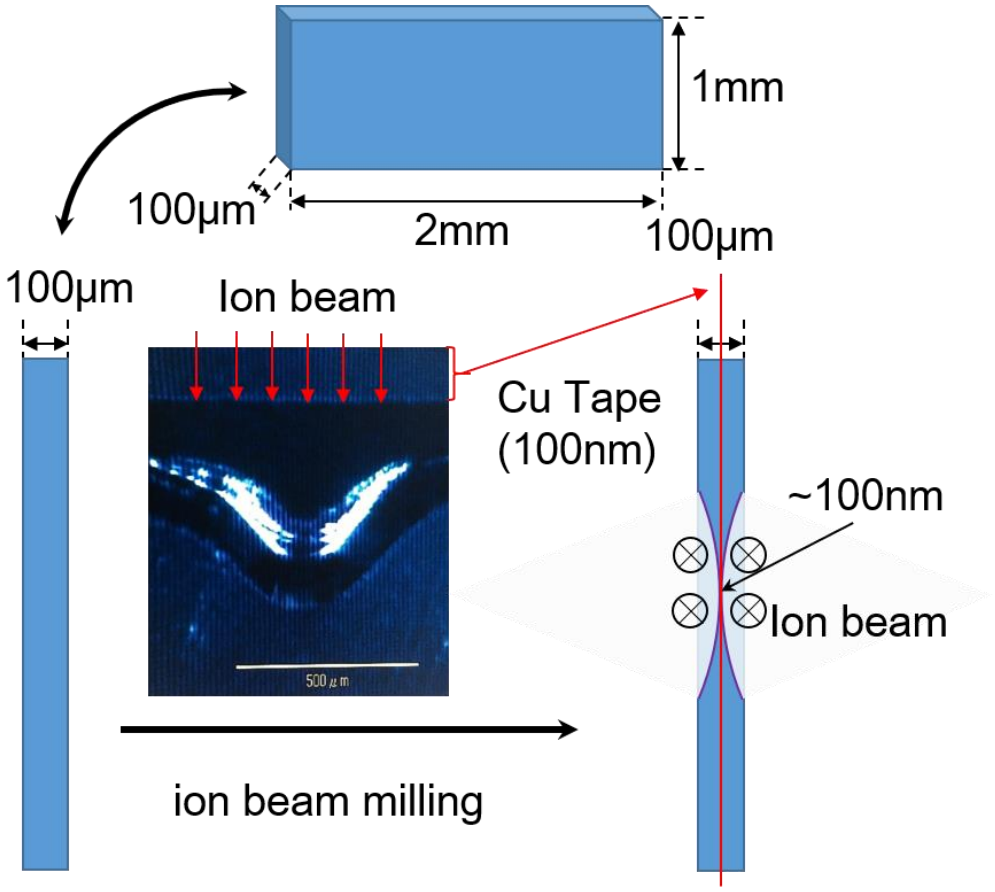

Fig. 2.15 A schematic diagram of procedure to prepare a typical planar TEM specimen.

2.10 Reference

[1] W. J. Parker, R. J. Jenkins, C. P. Butler, G. L. Abbott, *J. Appl. Phys.* **1961**, *32*, 1679.

[2] J. A. Koski, in *Proc. 8th Symp. Thermophys. Prop.*, The American Society Of Mechanical Engineers, **1981**, p. 125.

[3] D. M. Rowe, *CRC Handbook of Thermoelectrics*, CRC Press, **1995**.

[4] J. Martin, T. Tritt, C. Uher, *High Temperature Seebeck Coefficient Metrology*, American Institute Of Physics, **2010**.

[5] B. D. Cullity, S. R. Stock, **2001**.

[6] T. G. Rochow, P. A. Tucker, in *Introd. to Microsc. by Means Light. Electrons, X Rays, or Acoust.*, Springer US, Boston, MA, **1994**, pp. 297–327.

[7] W. Zhou, Z. L. Wang, *Scanning Microscopy for Nanotechnology : Techniques and Applications*, Springer, **2007**.

3. Thermoelectric properties of heavily boron- and phosphorus-doped Si

3.1 Introduction

To understand the effect of nanostructure on thermoelectric properties, it is necessary to compare the thermoelectric properties of the nanostructured Si with that of the single crystal Si. However, the experimental data of single crystal Si with a similar order of doping level to that of the nanostructured Si is presently lacking, especially for results measured at elevated temperature. There is only one study that exhibits dopant concentrations dependent TE properties of the single crystal Si. However, the doping concentrations in that study are lower than 1.4×10^{19} cm^{-3} and 8.1×10^{19} cm^{-3} respectively for n-type and p-type, which is insufficient as reference data for nanostructured Si.

In this section, we explore thermoelectric properties of the heavily doped (from $10^{18}cm^{-3}$ to $10^{20}cm^{-3}$) p-type and n-type single crystal Si with the temperature shifting from room temperature to above 1000K. A simple theoretical model is proposed for the estimation of temperature dependent thermoelectric properties of bulk Si samples at different doping levels.

3.2 Experimental procedures

The present research mainly used monocrystalline Si wafers. A ResiTest 8340 system (Toyo Co.) was used to determine the concentration and mobility of the charge carrier through Hall measurement in the magnetic field of 0.5 T in the van der Pauw geometry. Table 3.1 shows the resistivity and carrier density as well as the information of the samples. Moreover, we used the four-point current-switching method to measure the electrical conductivity. The static DC method was adopted to obtain the Seebeck coefficient on the basis of the slope of temperature-difference versus voltage curve. The Seebeck coefficient and electrical conductivity were measured through a bar-type sample cut from the Si wafer by employing commercial equipment (ZEM-3, Ulvac Inc.). The sample was about 2mm wide and 15mm long.

According to the density, thermal diffusivity and heat capacity, we could calculate the thermal conductivity. The laser flash technique was employed to measure the thermal diffusivity. To be specific, P1 was measured through TC-7000 (Ulvac Inc.) from the indoor temperature to 1073 K, and N1, N2, N3, P2 and P3 were measured through LFA 457 (Netzsch) from indoor temperature to 1073 K. Si wafers was bonded through spark plasma sintering (SPS). Because more than 95% heat is carried through phonons with the average free path smaller than 100 μm in the nondoped monocrystalline Si based on the molecular dynamics simulation by Henry et al[1]. Therefore, the influence of phonon scattering on the bonded interface can be ignored.

The samples were bonded as below. Firstly, we cut the Si wafers into squares of one centimeter, and washed the surface in acetone and 2% HF for one minute. In this way, four or five chips were prepared, set in a graphite die and sintered through the SPS system (Dr. Sinter SPS-515A, Sumitomo Coal Mining Co., Ltd.). The specific conditions were as below: the pressure was 34 MPa, the peak temperature was 1000 °C, and the heating rate was 80 °C/min in the Ar flow atmosphere. The formation of dislocation in sintering was minimized by keeping the holding time for 1 minute. The SEM (scanning electron microscopy) image of the cross section of the sintered sample is as shown in Figure 3.1. The bonded interface can hardly be seen, which indicates that the wafers were tightly bonded.

Table 3.1 Information of samples used in the present study.

Sample code	Manufacturer	Sample	Dopant	Thickness (mm)[a]	Thickness (mm)[#]
N1	Miyoshi Ltd.	Si wafer <1 0 0>	P	0.38	1.57
N2	Axt inc.	Si wafer <1 1 1>	P	0.52	1.94
N3	Nilaco Co.	Si wafer <1 0 0>	P	0.52	2.06
P1	Miyoshi Ltd.	Si wafer <1 0 0>	B	0.75	0.75
P2	Sumco Co.	Si wafer <1 0 0>	B	0.61	2.36
P3	Axt inc.	Si wafer <1 1 1>	B	0.42	1.95

[*] The thickness of the samples which were used to measure the electrical properties.

[#] The thickness of the sintered samples which were used to measure the thermal diffusivity.

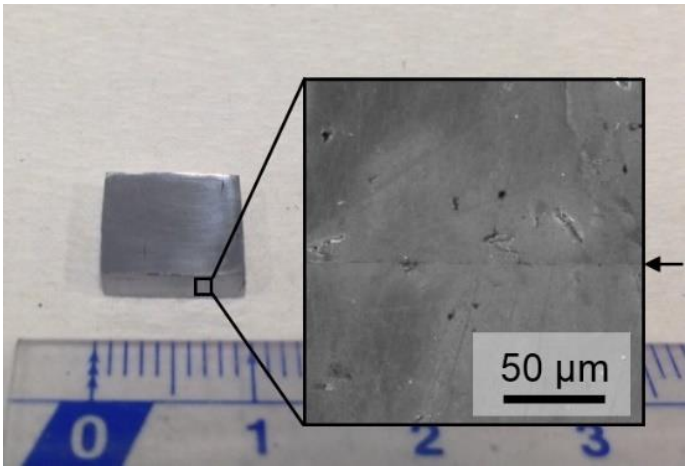

Fig. 3.1 SEM image of the cross section of the bonded Si wafer. The arrow shows the interface.

3.3 Model for thermoelectric transport in Si

3.3.1 Electron modeling

From the standard formulation based on the Boltzmann transport equation under the relaxation time approximation, the electrical conductivity and Seebeck coefficient of bulk materials are given by[29)]

By the standard formulation on the basis of Boltzmann transport equation with the relaxation time approximation, the electrical conductivity σ and Seebeck coefficient S of bulk materials can be calculated through[2]

$$\sigma = -\frac{1}{3}\int q^2\tau(E)v(E)^2\frac{\partial f(E_F,E)}{\partial E}D(E)dE \tag{3.1}$$

$$S = \frac{1}{3}\int q\frac{E-E_F}{T}\tau(E)v(E)^2\frac{\partial f(E_F,E)}{\partial E}D(E)dE \Big/ \sigma \tag{3.2}$$

Where, D is the density of the electronic states, f is the Fermi–Dirac distribution function, v is the group velocity of the charge carriers, τ is the energy-dependent momentum relaxation time, q is the charge of electrical carriers, E_F is the Fermi level, and E is the electron energy. Electrons are scattered through acoustic phonons and ionized impurities in crystalline Si. Therefore, this model mainly considered the two scattering mechanisms. Table 3.2 shows the function forms of momentum relaxation time for the specific scattering mechanisms and the parameters of the band structure.

To calculate TE properties of Si–Ge and Si alloys, similar approaches have also been proposed[3][4][5][6]. This research used the same model as those proposed by Minnich et al. [5] and Lee et al.[6] who proposed the three-band transport, namely, the conduction band at near Point X and L as well as one effective valence band. The L band is of great importance at high doping levels and temperature. A parabolic band approximation was used to modeling the valence band and a nonparabolicity of the conduction bands was considered through the approximation of the conduction bands:

$$E(1+\alpha E) = \frac{\eta^2 k^2}{2m^*}, \tag{3.3}$$

Where, m^* is the effective mass at the valence band maximum (or conduction band minimum), and α is the nonparabolicity coefficient. We determined the effective mass m^* by fitting it to the experimental data in the research. Table 3.2 summarizes the parameters related to the band structure.

Table 3.2 Electron modeling parameters.

Property	Value	Note
Dielectric constant	$\varepsilon = 11.7$	Ref. [7]
Effective mass of electrons at X point	$m_X^* = 2.0 \cdot m_e$	Fitted parameter
Effective mass of electrons at L point	$m_L^* = 1.4 \cdot m_e$	Fitted parameter
Effective mass of holes in valence band	$m_v^* = 1.4 \cdot m_e$	Fitted parameter
Longitudinal acoustic velocity	$v_l = 9040$ (m/s)	Ref. [7]
Transverse acoustic velocity	$v_s = 5340$ (m/s)	Ref. [7]
Mass density	$\rho = 2329$ (kg/m^3)	Ref. [7]
Bulk moduli	$Cl = v_l^{\,2} \cdot 2\rho$ (Pa)	Ref. [7]
Energy gap	$E_g = 1.17 - \frac{4.73 \cdot 10^{-4} \cdot T^2}{T + 636}$ (eV)	Ref. [6]
Nonparabolicity	$\alpha = 0.5$	Ref. [6]
Screening length	$L_D = \sqrt{\varepsilon \varepsilon_0 k_B T / q^2 N}$	Ref. [7]
Ionized impurity scattering rate	$\tau_i = \frac{16\sqrt{2m^*}\pi\varepsilon^2\varepsilon_0^2}{Nq^4}\left(\ln(1+\gamma^2) - \frac{\gamma^2}{1+\gamma^2}\right)^{-1} E^{3/2}$ $\gamma^2 = 8m^* E L_D^2 / \eta^2$	Ref. [7]
Electron-phonon scattering potential	$D_A = -9.5$ (electron), 5.0 (hole)	Ref. [7]
Electron-phonon scattering rate	$1/\tau_{e-p} = \frac{\pi D_A^2 k_B T}{\eta Cl} \frac{D_c(E)}{6}$	Ref. [7]
Hole-phonon scattering rate	$1/\tau_{h-p} = \frac{\pi D_A^2 k_B T}{\eta Cl} D_v(E)$	Ref. [7]

3.3.2 **Phonon modeling**

The model developed by Wang[2] was used to calculate the thermal conductivity of the lattice on the basis of Boltzmann transport equation. According to equation (3.4) and Boltzmann transport equation with the approximation of relaxation time, the thermal conductivity of the lattice is:

$$k = \frac{1}{3}\int_0^{\omega_{\max}} C(\omega)v(\omega)\Lambda(\omega)d\omega, \tag{3.4}$$

A sine-type function, $\omega = \omega_{max}\sin(\pi\kappa/2\kappa_0)$ was used to approximate the dispersion relation for the acoustic mode. The optical modes that are not significant for heat transport were ignored. The wave vector parameter κ_0 and frequency parameter ω_{max} were[3]:

$$\kappa_0 = \left(6\pi^2/V\right)^{1/3}, \tag{3.5}$$

$$\omega_{\max} = \frac{w}{\pi}v_s\left(6\pi^2/V\right)^{1/3}, \tag{3.6}$$

$$\frac{1}{v_s^2} = \frac{1}{3}\left(\frac{1}{v_{sL}^2} + \frac{2}{v_{sT}^2}\right), \tag{3.7}$$

Where, V is the volume of a primitive cell, v_{sT} and v_{sL} represent the transverse and longitudinal sound velocity.

Combined with Matthiessen's rule, this research considered the phonon scattering mechanisms, including umklapp scattering Λ_{umkl} and impurity/defect scattering Λ_{imp}, as shown below:

$$\Lambda_{eff}^{-1}(\omega,T) = \Lambda_{imp}^{-1}(\omega) + \Lambda_{umkl}^{-1}(\omega,T). \tag{3.8}$$

The specific scattering mechanism can be written through

$$\Lambda_{imp}^{-1}(\omega) = A\omega^4/v, \tag{3.9}$$

$$\Lambda_{umkl}^{-1} = B_1\omega^2 T\exp\left(-B_2/T\right)/v. \tag{3.10}$$

B_1 and B_2 a, namely, the umklapp scattering parameters, are expressed as[8]

$$B_1 \approx \frac{\eta\gamma^2}{Mv^2\theta} \tag{3.11}$$

$$B_2 = \frac{\theta}{3} \tag{3.12}$$

Where, γ is Grüneisen parameter, and M presents the average mass of atom in the crystal. θ is the Debye temperature calculated through

$$\theta = \frac{\eta\omega_{\max}}{k_B}. \tag{3.13}$$

By fitting γ to the literature data of nondoped monocrystalline Si, we obtained a γ value of 0.9[9]. It is assumed that the impurity scattering parameter A is linearly related to the concentration of impurity.

$$A = A_i x_i \tag{3.14}$$

Where, x_i is the impurity concentration of dopant i. We can determine the proportionality factor A_i by fitting it to the experimental data in this research. Table 3.3 summarizes the parameters that are used to calculate the thermal conductivity of the lattice.

Table 3.3 Phonon modeling parameters for Si.

Quantity	Value
v_{sL} (m/s)	8973[8]
v_{sT} (m/s)	5398[8]
v_s (m/s)	6084
V (prim. cell) (10^{-30}m^3)	40
K_0 (10^{-10}m^{-1})	1.14
ω_{max} (THz)	43.8
γ	0.9
A_B, A_P (10^{-70} s^{3}m^3)	8.62
B_1 (10^{-19} s/K)	1.47
B_2 (K)	112

3.4 Results and discussion

3.4.1 Carrier transport property

Assuming complete ionization of the dopants, the carrier density was considered to be equal to the impurity concentration. Figures 3.2(a) and (b) show the measured electrical conductivity and Seebeck coefficient, respectively, at room temperature as a function of impurity concentration. Data from references[8-10, 16] are plotted together, showing that the data observed in the present study agrees well with the literature data at room temperature.

The dopants are assumed to be completely ionized, and carrier density was the same as the concentration of the impurity. The Seebeck coefficient and electrical conductivity measured at room temperature as the function of impurity concentration are presented in Figures 3.2(a) and (b). The data collected from references[10][11][12][13] are plotted, which are consistent with those observed in this research at indoor temperature.

Figures 3.3(a) and (b) show the temperature dependent electrical conductivity and Seebeck coefficient for n-type Si, and (c) and (d) for p-type Si, respectively. Note that the model can qualitatively reproduce the temperature dependences of electrical conductivity and Seebeck coefficient of the samples, including heavily doped Si. Although the theoretical curve deviates from the experimental curve of the lightly doped samples, the model can be used to predict thermoelectric properties of Si because a higher doping concentration is favorable for higher thermoelectric performance bulk Si.

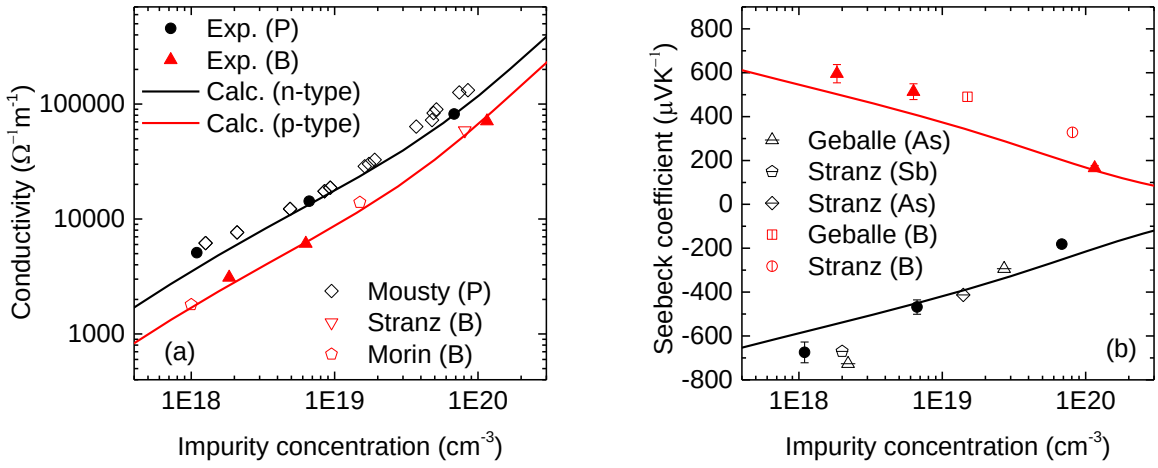

Fig. 3.2 Impurity concentration dependence of electrical conductivity and Seebeck coefficient of Si obtained experimentally (filled symbols) and calculated (curves). Reference data[10][11][12][13] agree well with the fitting curves. The dopant atoms are represented by the characters in blankets, such as P, B, As and Sb.

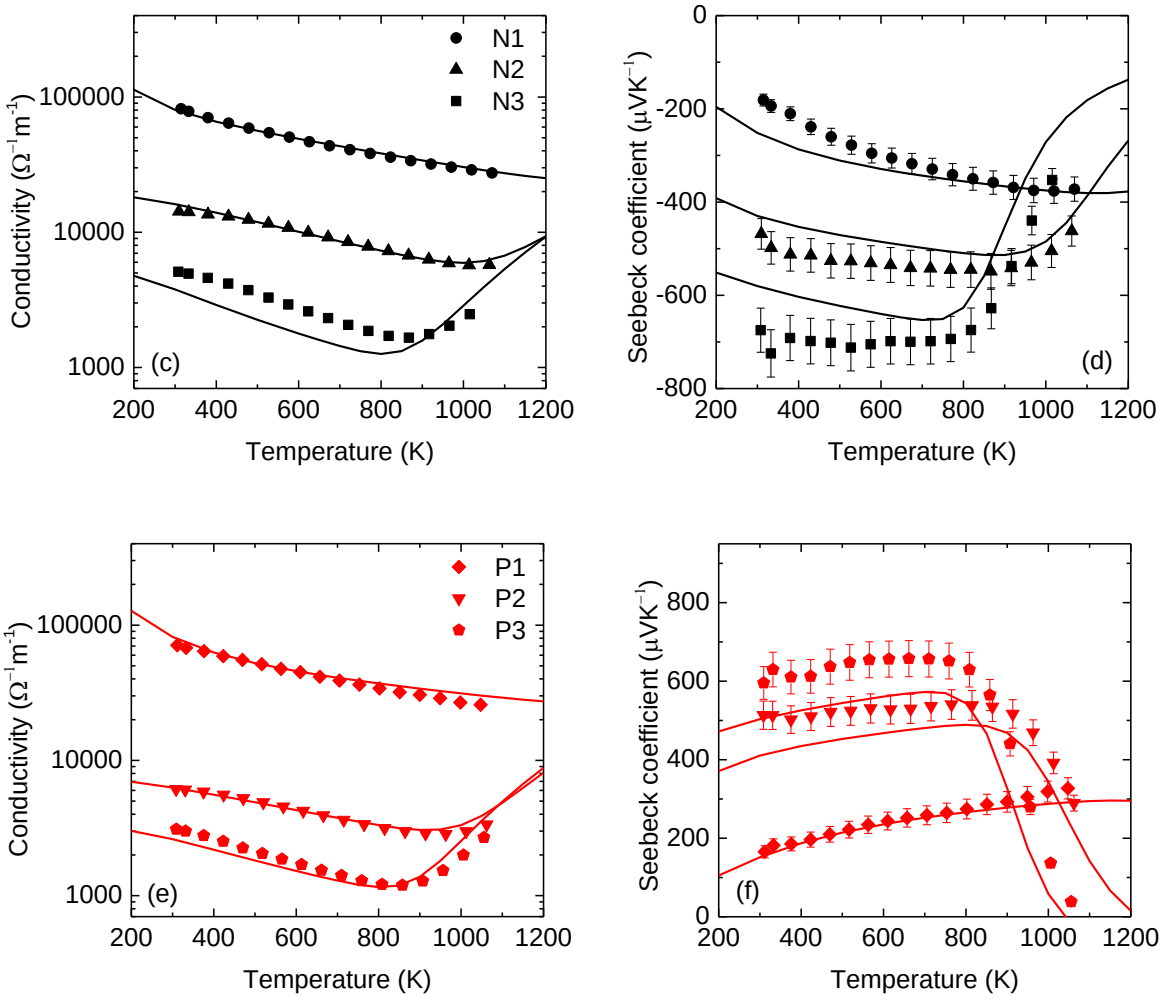

Fig. 3.3 Temperature dependence of the electrical properties of experimental data (filled symbols) and calculated data (curves) of Si.

3.4.2 Thermal transport properties

The thermal conductivities in this research are presented in Figure 3.4. Figure 3.4 (a) shows the impurity concentration dependence. The data collected from references[10][14][15][16] show that the current data are in good agreement with those reported at indoor temperature. Figures 3.4 (b) and (c) show the temperature dependence.

The thermal conductivity κ is composed of the lattice thermal conductivity κ_{lat} the electrical thermal conductivity κ_e. According to the Wiedemann–Franz law the electronic thermal conductivity can be calculated through $\kappa_e = LT\sigma$, where L is Lorenz factor (~2.44×10^{-8} $J^2 K^{-2} C^{-2}$). The electronic thermal conductivity is estimated for all samples smaller than 0.8 W $m^{-1} K^{-1}$ in the whole temperature range, which is can be ignored when compared with lattice thermal conductivity of Si, revealing the phonon contribution plays a dominate role for κ. As shown in the Figure 3.4, the thermal conductivity decreases with the temperature and impurity concentration, which indicates that the thermal conductivity are scattered by phonons and impurities. Based on the comparison of thermal conductivity of the non-bonded and bonded samples, the deviations are proved to be small, which shows that the thermal conduction is less affected by bonding. Therefore, the bonding effect can be negligible in this research.

The experimental data and calculated data of lattice thermal conductivity are also compared in Figure 3.4. The theoretical curve is quantitatively consistent with experimental data. A same value of impurity scattering parameters of B-doped sample and P-doped sample are estimated as A_B and A_P by fitting the experimental data because there was no significant difference on impurity-concentration-dependent thermal conductivities between B- and P- doped Si. In addition, through molecular dynamics simulations, Lee et al.[15] reported that the thermal transport in Si can be suppressed more effectively by B doping in Si compared with P doping. According to the model proposed by Abeles[4], this is resulted from the differences between the matrix atom and the dopant atoms in atomic radius and/or atomic radius. Since B and Si have greater difference in atomic radius and atomic radius than P and Si, the phonon scattering should be increased by B doping. In this research, there was no obvious difference because the impurity concentration of samples(< 1.5×10^{20} cm^{-3}) are lower than that employed in Lee's simulation (5×10^{20} cm^{-3}).

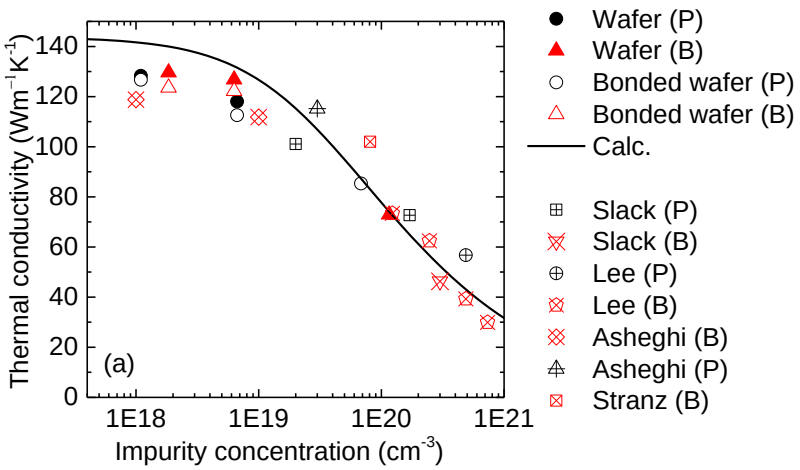

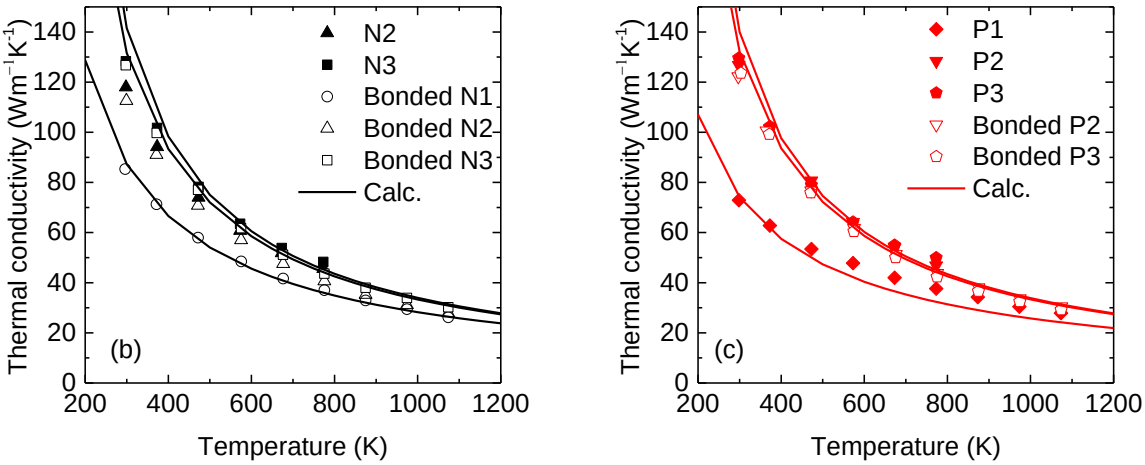

Fig. 3.4 (a) The calculated (curve) and experimental (filled symbols) thermal conductivity of Si. The reference data were collected from the experiments[10][14][15][16] as well as the results of molecular dynamics simulation[15]. (b) and (c) represent the thermal conductivity as the function of temperature of p-type and n-type monocrystalline Si.

3.4.3 **Thermoelectric properties**

Figures 3.5(a) and (b) show *ZT* and power factor at 570 K, which is the function of impurity concentration.

Based on Wiedemann–Franz law, the electrical thermal conductivity can be calculated through the electron transport model. We added the electrical thermal conductivity to calculate the total thermal conductivity. As shown in Figure 3.5 (a), the power factor observed experimentally at 570 K increases with the impurity concentration. The power factor was predicted to decrease in the case that the concentration of the impurity was greater than 2×10^{20} cm^{-3} because of the decrease of the Seebeck coefficient. *ZT* showed no peak when the impurity concentration lower than 3×10^{20} cm^{-3}. This indicates that TE properties of doped sample with a higher impurity concentration should be measured so as to determine the optimum concentration of impurity for monocrystalline Si.

Fig. 3.6 shows the theoretically and experimentally predicted values of *ZT* as the function of temperature. The calculation results conformed to the data observed in experiments, which indicated that *ZT* of the samples was linearly increased with the temperature under linearly. If the temperature was higher than 900 K, the *ZT* of the lightly doped samples decreased because of the bipolar effect. Table 3.4 summarizes TE properties of the samples at 300 and 570 K.

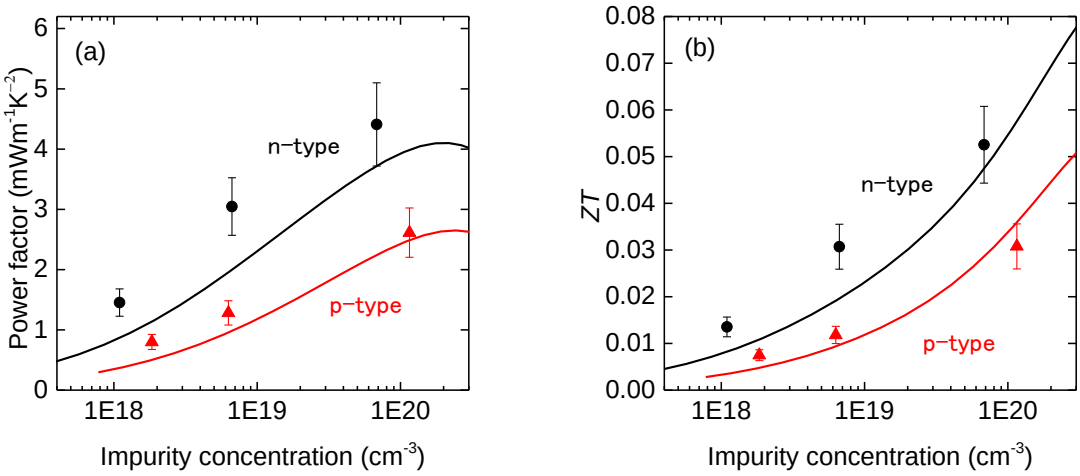

Fig. **3.5** Impurity concentration dependent (a) Power factor; and (b) *ZT* of Si at 570 K. The curves and symbols show the calculated results and experimental data, respectively.

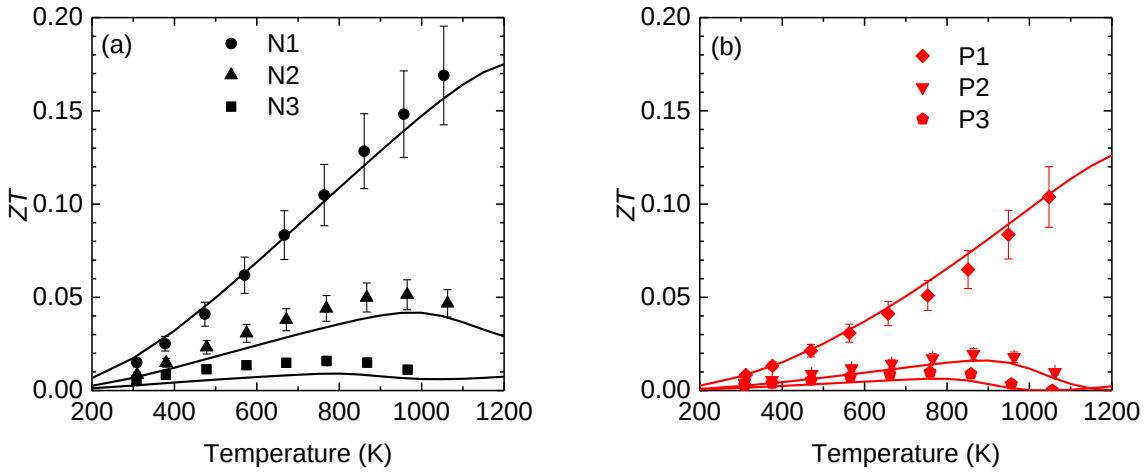

Fig. **3.6** *ZT* of (a) n-type Si and (b) p-type Si as a function of temperature. The curves and symbols show the calculated results and experimental data, respectively.

Table 3.4 Thermoelectric properties of all samples at 300K and 570K.

Sample	Carrier density (cm^{-3})	Dopant	*Tc* (K)	σ ($10^3 \cdot \Omega^{-1} \cdot m^{-1}$)	*S* (μV/K)	κ (W/m·K)	*ZT*
N1	6.8×10^{19}	P	300	82 ± 6	-180 ± 10	85	0.010 ± 0.002
			570	51 ± 4	-300 ± 20	48	0.053 ± 0.008
N2	6.7×10^{18}	P	300	14± 1	-470 ± 30	113	0.009 ± 0.001
			570	11 ± 1	-530 ± 40	57	0.031 ± 0.005
N3	1.1×10^{18}	P	300	5.1 ± 0.4	-680 ± 50	127	0.006 ± 0.001
			570	2.9 ± 0.2	-710 ± 50	62	0.014 ± 0.002
P1	1.2×10^{20}	B	300	71 ± 5	170 ± 10	73	0.008 ± 0.001
			570	48 ± 3	230 ± 20	48	0.031 ± 0.005
P2	6.3×10^{18}	B	300	6.1 ± 0.4	510 ± 40	122	0.004 ± 0.001
			570	4.6 ± 0.3	530 ± 40	62	0.012 ± 0.002
P3	1.8×10^{18}	B	300	3.1 ± 0.2	600 ± 40	124	0.0028 ± 0.0004
			570	1.9 ± 0.1	660 ± 50	60	0.007 ± 0.001

3.5 Conclusions

This research measured the TE properties dependent on temperature of the heavily doped (10^{18}–10^{20} cm^{-3}) p-type and n-type monocrystalline Si from the room temperature up to 1000 K. Based on Boltzmann transport equation, the TE properties of Si were predicted by establishing a theoretical model. It is found that the calculation on the basis of the model can demonstrate the data of the heavily doped Si observed in the experiment, which proves that the TE properties of highly doped Si can be predicted through the model. The *ZT* values calculated from the measured data increased with the concentration of impurity. Therefore, the optimal doping concentration should be determined in the research on the TE properties of more heavily doped Si. Moreover, the influence of nanostructures on the TE properties, especially the thermal conductivity, of Si can be estimated through the newly-developed theoretical model by adding new component of scattering mechanisms via Matthiessen's rule, which laid the groundwork for our following researches to design and fabricate high-performance Si TE composites.

3.6 Reference

[1] T. Ackbarow, J. Buehler, *J. Comput. Theor. Nanosci.* **2008**, *5*, 1193.

[2] Z. Wang, J. E. Alaniz, W. Jang, J. E. Garay, C. Dames, *Nano Lett.* **2011**, *11*, 2206.

[3] C. Dames, G. Chen, *J. Appl. Phys.* **2004**, *95*, 682.

[4] B. Abeles, *Phys. Rev.* **1963**, *131*, 1906.

[5] J. Minnich, H. Lee, W. Wang, G. Joshi, S. Dresselhaus, F. Ren, G. Chen, D. Vashaee, *Phys. Rev. B* **2009**, *80*, 155327.

[6] H. Lee, D. Vashaee, D. Z. Wang, M. S. Dresselhaus, Z. F. Ren, G. Chen, *J. Appl. Phys.* **2010**, *107*, 1.

[7] M. Lundstrom, *Fundamentals of Carrier Transport, 2nd Ed.*, Cambridge University Press, Cambridge, United Kingdom, **2000**.

[8] T. Morelli, P. Heremans, A. Slack, *Phys. Rev. B* **2002**, *66*, 195304.

[9] R. Shanks, D. Maycock, H. Sidles, C. Danielson, *Phys. Rev.* **1963**, *130*, 1743.

[10] A. Stranz, J. Kähler, A. Waag, E. Peiner, *J. Electron. Mater.* **2013**, *42*, 2381.

[11] F. Mousty, P. Ostoja, L. Passari, *J. Appl. Phys.* **1974**, *45*, 4576.

[12] J. Morin, P. Maita, *Phys. Rev.* **1954**, *96*, 28.

[13] T. H. Geballe, G. W. Hull, *Phys. Rev.* **1955**, *98*, 940.

[14] A. Slack, *J. Appl. Phys.* **1964**, *35*, 3460.

[15] Y. Lee, G. S. Hwang, *Phys. Rev. B* **2012**, *86*, 75202.

[16] M. Asheghi, K. Kurabayashi, R. Kasnavi, K. E. Goodson, *J. Appl. Phys.* **2002**, *91*, 5079.

4. Thermoelectric properties of Si/Silicide sub-micro composite prepared by melt-spinning technique

4.1 Introduction

Although a very accurate control of the nanoparticle size is not essential in order to produce the desired lowering of thermal conductivity, a length scale of <100 nm is favorable to achieve a high figure of merit *ZT*, which is difficult to be formed in a conventional solidification process. There is the free-energy-change-associated nucleation on discussion, which provides a generally applicable way for controlling resultant length scale. As shown in Fig. 4.1, precipitation reaction can be described as $\alpha' \rightarrow \alpha + \beta$. α' points the supersaturated α phase from the quenching of a high temperature phase. When free energy changes lower, which leading to a negative value of ΔG, β phase will start nucleate. ΔG can be calculated by the following equation:

$$\Delta G = -V(\Delta G_V - \Delta G_S) + A\sigma \tag{4.1}$$

V is nuclei volume. ΔG_V means volumetric free energy. ΔG_S represents misfit strain energy. Nuclei surface area is *A*. σ indicates surface free energy. It is almost the same for σ on solid/liquid interfaces. However, σ for the nucleation in solid, changes in a broad range widely from very low values to high values, respectively, for coherent interfaces and incoherent interfaces. Under the assumptions that the variation of σ with interface orientation can be ignored and there is a radius of curvature r of the spherical nucleus, equation 4.1 will be transformed as follows:

$$\Delta G = -\frac{4}{3}\pi r^3(\Delta G_V - \Delta G_S) + 4\pi r^2\sigma \tag{4.2}$$

It is represented as a function of r in Fig. 4.1. Any nucleus shape can generate similar curves as a function of the nuclei size. The differentiation of Equation 4.3 yields

$$\Delta G^* = \frac{16\pi\sigma^3}{3(\Delta G_V - \Delta G_S)^2} \tag{4.3}$$

$$r^* = \frac{2\sigma}{\Delta G_V - \Delta G_S} \tag{4.4}$$

"ΔG^*" means the nucleation barrier for nucleation while "r^*" refers to the critical nucleus size. This can be shown in Fig. 4.1, when $r^* > r$, dissolution of the precipitate will occur to reduce the free energy. When $r^* < r$, on the contrary, precipitate will grow.

In the equation formula of 4.4, ΔG_V represents the chemical driving force of precipitation, which dominantly affect the value of ΔG^*. A higher ΔG_V can contribute to a lower ΔG^*, which results in a high nucleation rate for precipitation[1]. It is therefore attractive since a lower ΔG^* can lead in a refined size of precipitates[2][3].

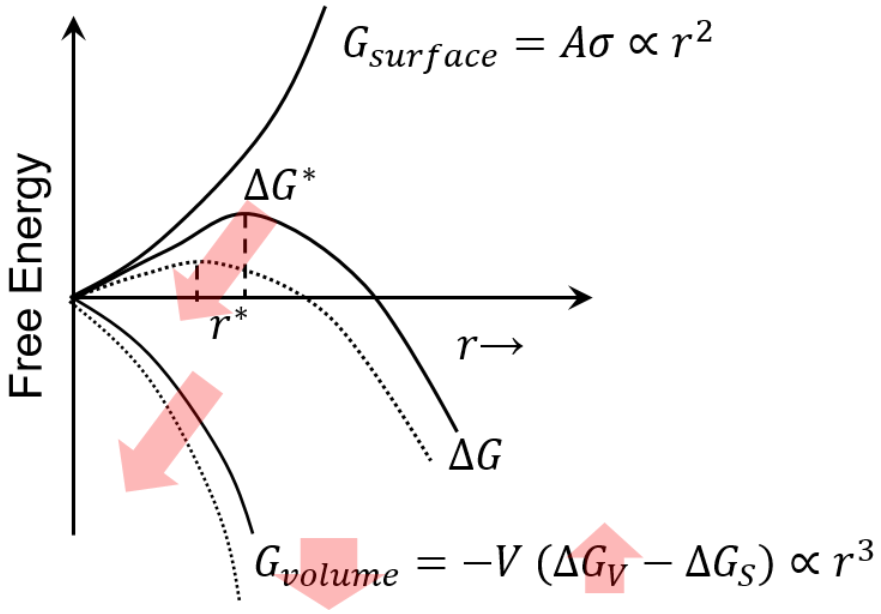

Fig. 4.1 The free energy change associated with homogeneous nucleation of a sphere of radius r.

To be more specific, the solution will be supersaturated with B when the composition $x_{B,0}$ of atom B drops from temperature T_h to T_l. In this case, ΔG_n serves as the driving force of nucleation of β, as demonstrated in the Fig. 4.2. The free energy change by nuclei formed per mole is listed in below:

If a phase α is dissolved in a material containing nucleus composition ($x_{B,\beta}$), a certain amount of free energy ΔG_1 will be decreased in the system.

$$\Delta G_1 = \mu^0_{A,\alpha} x_{A,\beta} + \mu^0_{B,\alpha} x_{B,\beta} \tag{4.5}$$

Here, Point P in Fig. 4.2 (a) is marked to show the quantity of ΔG_1.

The increase of the total free energy can be calculated as follows when the B atoms are rearranged into the β crystal structure:

$$\Delta G_2 = \mu^e_{A,\alpha} x_{A,\beta} + \mu^e_{B,\alpha} x_{B,\beta} \tag{4.6}$$

The quantity of ΔG_2 is shown as Q point. Thus, to calculate the driving force for nucleation, it needs to calculate as follows:

$$\Delta G_n = \Delta G_2 - \Delta G_1 \tag{4.7}$$

which refers to the length PQ shown in Fig. 4.2 (a). Therefore, the volume free energy decrease due to the nucleation event can be calculated through:

$$\Delta G_V = \frac{\Delta G_n}{V_m} \tag{4.8}$$

In this equation, V_m means the molar volume of β. Therefore, with the increase of undercooling, the chemical driving force increases correspondingly (ΔG_V for ΔT and $\Delta G_V'$ for $\Delta T'$). The higher ΔG_n would lead to an intense precipitate number density with the same B concentration, which is as illustrated in the Fig. 4.2(b). There are several thermoelectric systems have been observed with the expected trend of finer microstructure, such as PbTe/Sb_2Te_3, Bi_2Te_3/In_2Te_3 and $MnSi_{1.75}$/MnSi composites[4][5][6].

According to the thermodynamic equations calculating the undercooling, it is assumed that the undercooling can be increased arbitrarily in this way, which would further lead to the proportional increase of nucleation. This might be true for long annealing times. However, when it comes to the low-temperature undercooling, it might lead to the suppression of microstructure formation because of lacking of diffusion. In fact, the fasted nucleation rate can be obtained at an intermediate undercooling rate in most cases because of the balancing of thermodynamics and kinetics[7].

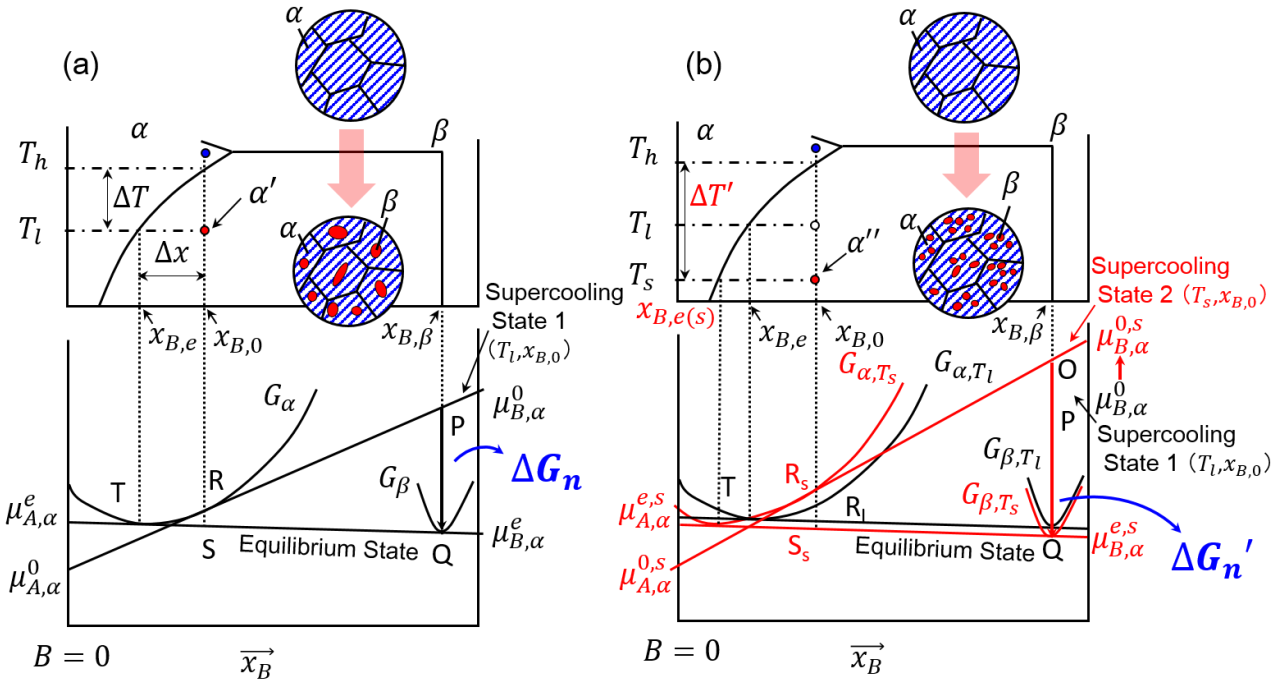

Fig. 4.2. Free energy changes during precipitation depends on different cooling speed.

However, as mentioned in charter 1.2.4, except for germanium the solubility of other atoms in Si is quite low. Under such a case, the phase transformations demonstrate none or limited temperature dependence (line compound, extreme cases). Normal preparation methods described above will then become invalid to lead to a second phase. For such kind of phase systems, metastable non-equilibrium processing, for instance mechanical alloying and rapid solidification, were assumed as a possible approach for introduction of nanostrucures. According to Turnbull[8], these methods have been described as the routes to quench and energize the metastable states. During the rapid solidification process, the state has been energized into the liquid state. To be more specific, after the quenching, amorphous solid state can be formed immediately. Then, the rapid cooling would attempt to stay away from the equilibrium state, which is as illustrated in the Fig. 4.3. Through short diffusion, it follows with a short range lattice relaxation from $G_{\alpha,RS}$ to G_α. Therefore, as the rapid solidification process extends the solubility to $x_{B,1}$, the formation of the precipitates then can be expected because of the increase of the chemical driving force ΔG_V.

On the other hand, the shortcomings of ball-milling process addressed in chapter 1.2.4 still reminded us to attach more attention on the rapid solidification techniques in the research, even though it has been demonstrated that mechanical alloying is an effective route in terms of solubility extension.[2] Besides, even though the solidification rate has been severely limited by the thermal conductivity, it is possible to achieve the cooling rates necessary to

increase the solubility in a rapid solidification process for Si owing to their relatively high thermal conductivities among thermoelectric materials.

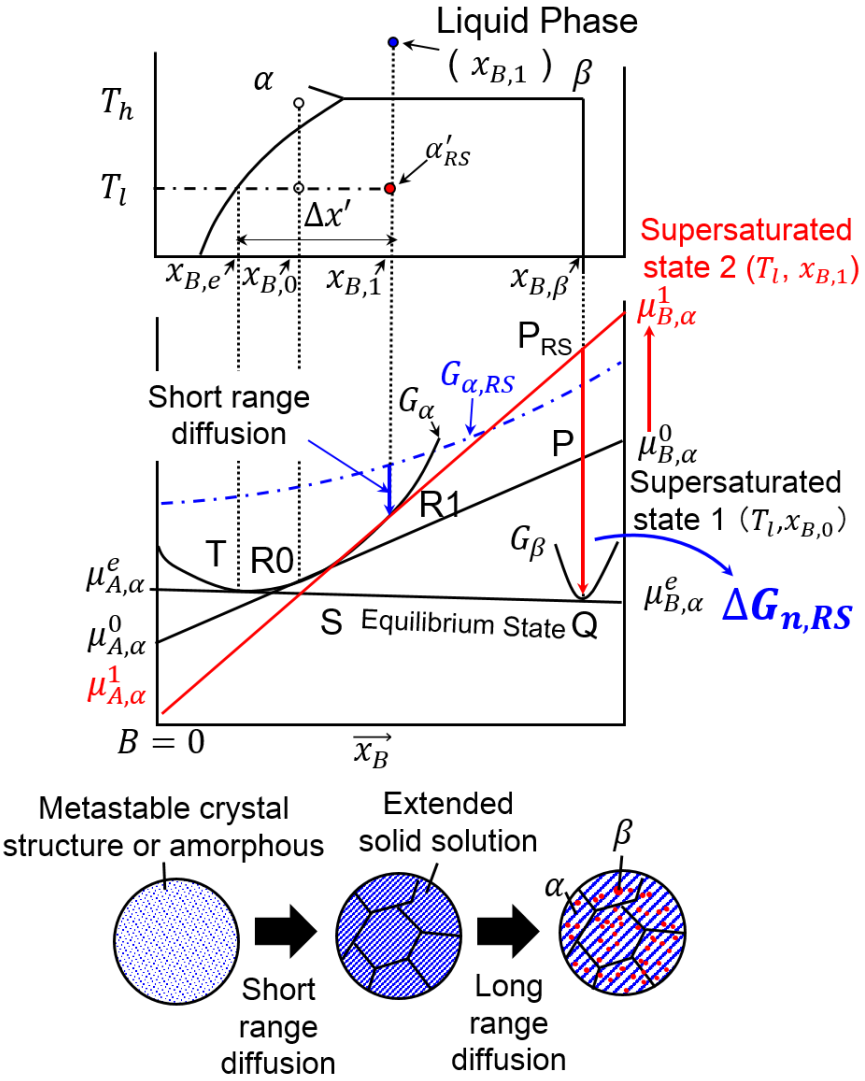

Fig. 4.3. Free energy changes during precipitation for a nonequilibrium process.

4.2 Experimental procedures

4.2.1 Synthesis

A series of samples with nominal compositions of $Si_{100-x}B_x$(x = 0, 1, 2, 4, 8) and $(Si_{0.99}B_{0.01})_{95}Co_5$ were firstly prepared with arc melting (Arc) in Ar atmosphere by using a stoichiometric amount of Si (chunks, 11N purity), Co (chunks, 3N purity), and B (chunks, 4N purity). The obtained ingot was put into a BN tube with a 0.35mm diameter nozzle, and under the protection of an argon atmosphere, the ingots were melted and ejected under a pressure of 0.02 MPa Ar onto copper roller rotating at a linear speed of 21 m/s, 42 m/s and 63 m/s, to obtain a supersaturated solid solution. The obtained samples, $Si_{99}B_1$-Arc, $Si_{92}B_8$-Arc, $Si_{92}B_8$-MS, $(Si_{0.99}B_{0.01})_{95}Co_5$-Arc and $(Si_{0.99}B_{0.01})_{95}Co_5$-MS were then crushed into powders and placed in a graphite die for spark plasma sintering (SPS) at 1373 K for 2 min under an axial pressure of 100 MPa in an Ar atmosphere. The sintered samples, of which the calculated relative density from the measured weight and dimensions were found to be over 94%, are marked as $Si_{99}B_1$-Arc-SPS, $Si_{92}B_8$-Arc-SPS, $Si_{92}B_8$-MS-SPS, $(Si_{0.99}B_{0.01})_{95}Co_5$-Arc-SPS and $(Si_{0.99}B_{0.01})_{95}Co_5$-MS-SPS.

4.2.2 Structural and thermoelectric characterizations

Phase characterization was conducted using powder X-ray diffraction (XRD) analysis in air at room temperature using Cu Kα radiation. Whole-powder-pattern decomposition method[9] combined with the least square method were used to estimate the lattice parameters of the samples from Powder X-ray Diffraction Data. The microstructures of the fine polished sample surface were investigated using field emission scanning electron microscopy (FE-SEM; JEOL JSM-6500F) under vacuum at room temperature. The electron backscattering diffraction (EBSD) experiments were performed in the FE-SEM equipped with a TSL OIM system. Microstructural observations were performed using a scanning electron microscope (SEM; JSM-6500F, JEOL) and transmission electron microscope (TEM, Tecnai G2 20ST, FEI) equipped with an energy dispersive X-ray spectroscope (EDS), operated at 20 and 200 kV, respectively. The Hall coefficient (R_H) was measured using Toyo Resitest8340 instrument at room temperature under a magnetic field of 0.5 T by the Van der Pauw method. The thermal conductivity (κ) was calculated by using $\kappa = DCd$, where the thermal diffusivity D was measured by a laser flash method on Netzsch LFA457 instrument at from room temperature to 1073K under an Ar atmosphere. The heat capacity C was estimated from those of pure Si, SiB_3 and $CoSi_2$, obtained from the FACT53 database and literature data[10], respectively. d was calculated from each sample's geometry and mass. A 4-point-technique and a static direct-current method were employed to measure the ρ and the S of the samples respectively by using ZEM-3 (ULVAC-RIKO, Inc., Japan) from 300K to 1073K under a He atmosphere. All experiments were repeated a few times, and the data are within the measurement errors (4% for electrical conductivity, thermal diffusivity, 3% for κ, and 4% for S).

4.3 Si-B system

4.3.1 Introduction

The binary Si-B system was selected for two main reasons: (1) as a semiconductor commonly used in semiconductor industry, the properties and technology of Si are well studied, making it easy to be compared with reference data understand on the size effect of precipitates; (2) to avoid complexity in ternary system, where B acted as alloy component as well as dopant.

Boron is a well-known dopant for p-type Si. The research results of Si–B binary phase diagram show maximum solubility limit from ~3 to 3.5 at. % at the eutectic temperature, which decreased to ~1 at. % at 1200 °C sharply, as shown in Figure. 4.4. When the solubility limit is lower than B concentration, excess B atoms can form Si boride phase. Among all the Si-B intermetallic compounds, SiB_3 is found to be a metastable phase, which only forming when boron is supersaturated in Si. Illustration of the crystal structure of SiB_3 is shown in Figure. 4.5.

In according to T. Aselage et al.[11], when the B concentration is between 3 at. % and 14 at. %, most of the precipitates are observed to be SiB_3 phase. Thus, a B-rich compositions of $Si_{92}B_8$ is presented in this work to ensure a sufficient amount of SiB_3 precipitates without introducing other precipitates.

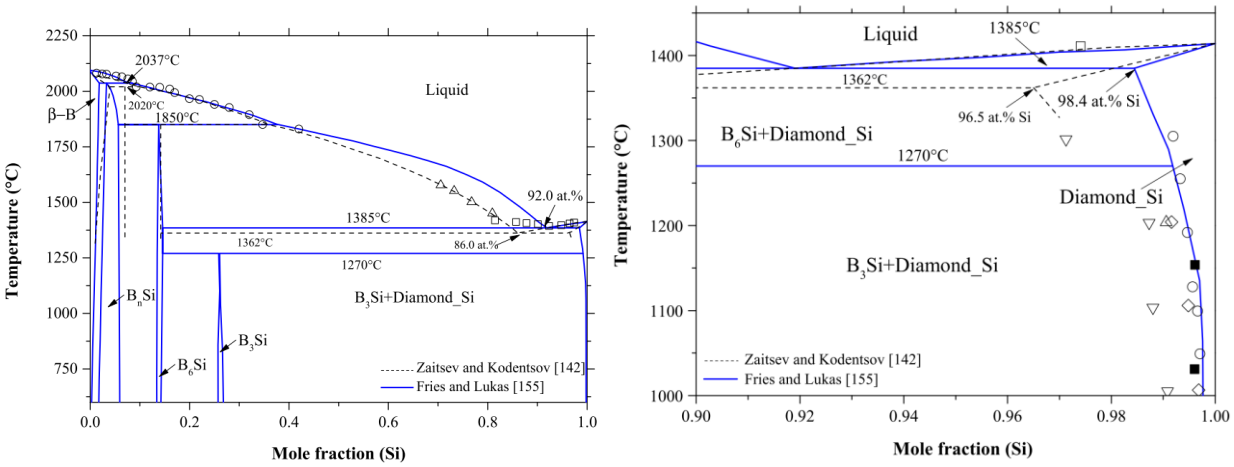

Fig. 4.4 Phase diagram of Si-B binary system.[12]

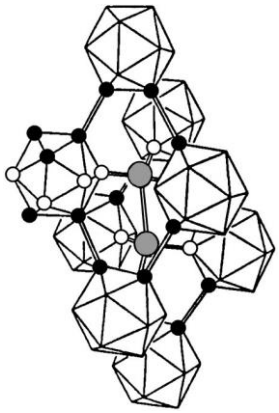

Fig. 4.5 Illustration of the crystal structure of SiB_3.[11]

4.3.2 Results and discussion

I. Microstructural characterization

Figure 4.11 shows the XRD patterns of the samples, and Fig. 4.6 shows the lattice parameters calculated from the observed XRD patterns. No peak other than those assigned to Si was observed for the $Si_{99}B_1$-Arc sample, which indicates that the additional B dissolved into the Si matrix in this sample. On the other hand, weak peaks associated with the trigonal borides SiB_3 are observed in the B-rich $Si_{92}B_8$-Arc sample. Although Si and SiB_6 are expected to be formed in the eutectic alloy based on the Si-B phase diagram, SiB_3 is known to be generated from B-rich Si-B melts.[11][13] This generation can be attributed to the relative ease of nucleation and growth of the metastable SiB_3 phase.[11] Although SiB_3 slowly decomposes into equilibrium over time, the reaction speed is relatively slow since this process relies on solid-state diffusion. Thus, SiB_3 alone was observed in the eutectic alloy.

The solution limit of B into Si can be estimated from the composition dependence of the lattice parameter, which is given in Fig. 4.7. The lattice parameters of $Si_{100-x}B_x$-Arc decrease with increasing B content since the covalent radius of B is smaller than that of Si, and they remain nearly unchanged for $x \geq 2$, indicating that the solubility limit of B into Si is x = 1–2. This result is consistent with the phase diagrams of Si-B systems[26] and also agrees with the previous experimental results.[11][14] On the other hand, the XRD pattern of the melt-spun $Si_{92}B_8$-MS shows that the sample still maintains a single phase without noticeable formation of SiB_3. The lattice parameter of $Si_{92}B_8$-MS is 5.403 Å, as shown in Fig. 4.7, which is much smaller than that of the arc-melted sample, suggesting that excessive B is dissolved in the Si phase. This result indicates that a supersaturated Si-B solid solution was obtained successfully by using the MS technique. In order to obtain the supersaturated solution, the linear speed of the Cu roller was quite important. We performed the experiment with linear speeds of 21 m/s, 42 m/s, and 63 m/s and chose 42 m/s since the lowest lattice parameter was obtained with that linear speed.

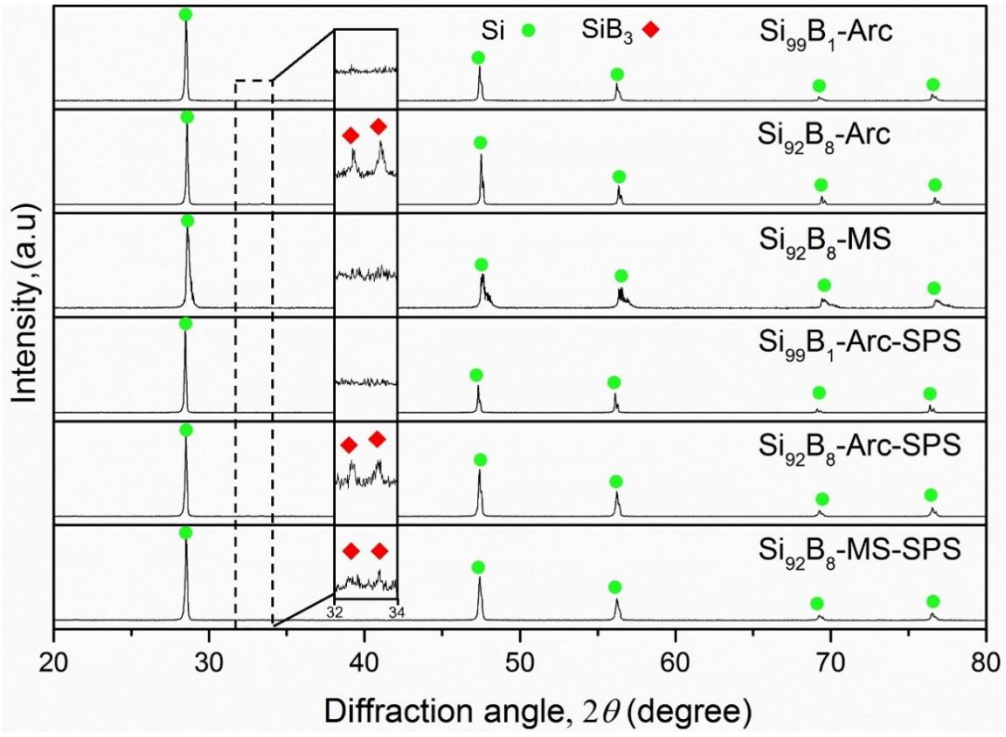

Fig. 4.6 XRD patterns of the $Si_{100-x}B_x$(x = 1, 8) samples prepared by different methods.

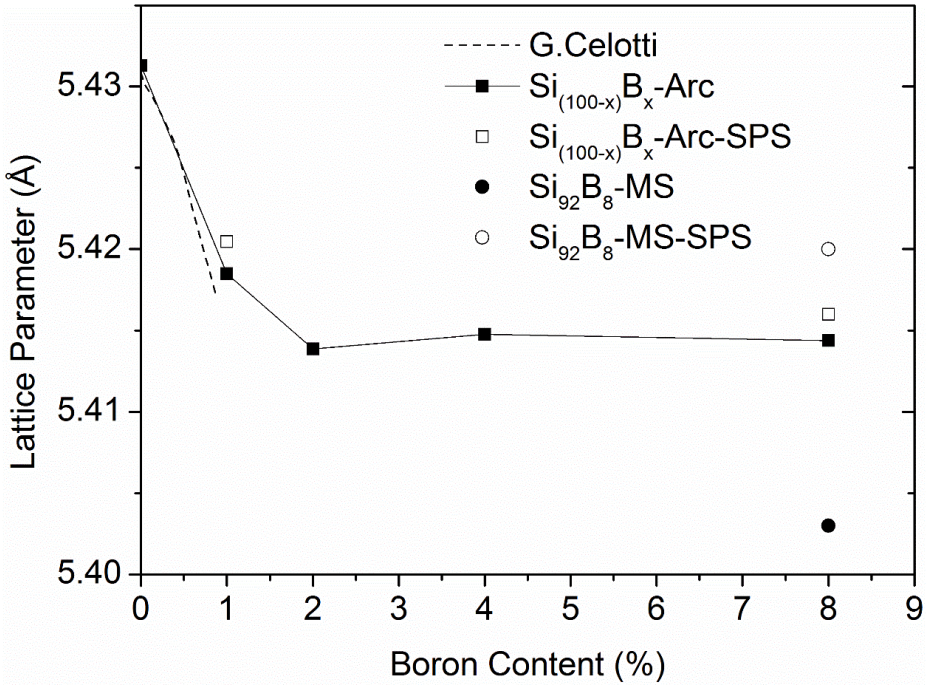

Fig. 4.7 Composition dependence of lattice parameter of $Si_{100-x}B_x$(x = 0, 1, 2, 4, 8) samples prepared by different methods at 300K.

Figure 4.8 shows the SEM images of $Si_{92}B_8$-MS. By melt spinning, ribbon-like samples are obtained of which surfaces are divided into the contact surface (where the melts touch the Cu roller) and the free surface. While no precipitates were observed on the contact surface, fine bright particles were observed around the grain boundaries on the free sur- face. Taking into account that no impurity peaks were detected in the XRD pattern of the $Si_{92}B_8$-MS, these particles are considered to be amorphous compound. This result suggests that a part of the excessive B was precipitated as amorphous Si-B particles on the free surface, since the cooling rate on the contact surface is lower than that on the free surface.

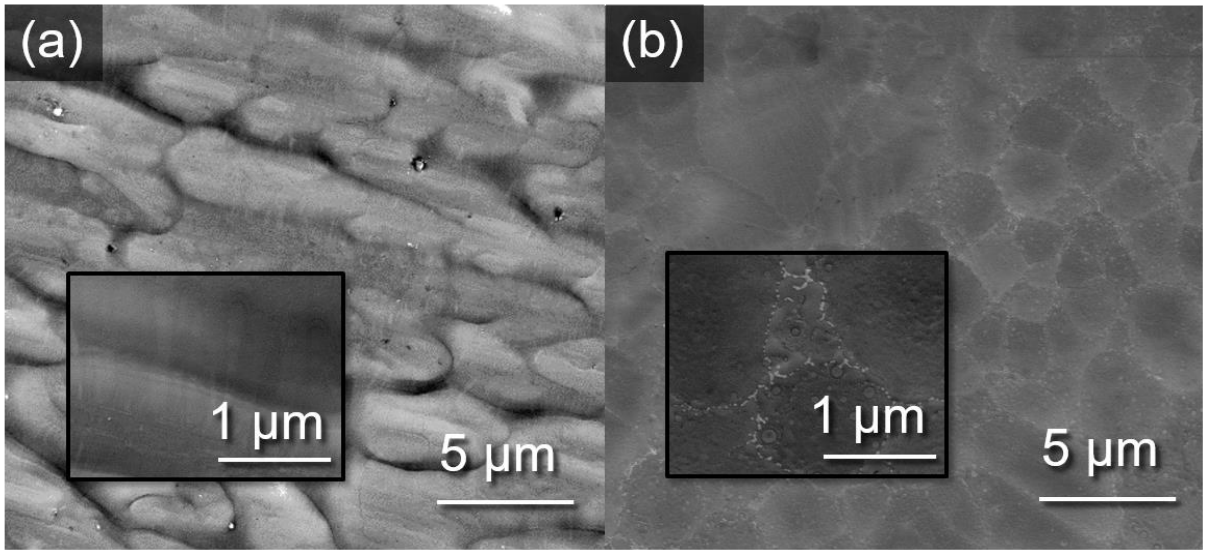

Fig. 4.8 Scanning electron micrographs of $Si_{92}B_8$-MS: (a) contact surface and (b) free surface.

$Si_{99}B_1$-Arc and $Si_{92}B_8$-Arc were sintered by SPS, and $Si_{99}B_1$-Arc-SPS and $Si_{92}B_8$-Arc-SPS were prepared. No obvious change was observed in the XRD patterns or lattice parameters of these samples, indicating that the SPS treatment did not affect the phase states of the arc-melted samples. However, significant changes were found in the XRD patterns and lattice parameter of $Si_{92}B_8$-MS-SPS, which was prepared from $Si_{92}B_8$-MS by SPS. The XRD patterns of $Si_{92}B_8$-MS-SPS and $Si_{92}B_8$-MS show that SiB_3 was precipitated by SPS. The increase of the lattice parameter in $Si_{92}B_8$-MS-SPS also suggests that supersaturated B was segregated from the Si matrix. This segregation can be attributed to the solid-state phase transition from the nonequilibrium to equilibrium state during SPS treatment. In addition, SEM images of melt-spun ribbon $Si_{92}B_8$-MS shown in Fig. 4.8 have revealed that amorphous precipitates or a small amount of crystalline precipitates possibly present after melt spinning and couldn't be detected in the XRD. However, considering the greatly decreased lattice parameter, which indicates the excessive B is predominantly dissolved in the Si matrix, the effects on thermoelectric properties introduced by such precipitates are considered to be not significant in this work.

The microstructure of the precipitated SiB_3 was observed by SEM. Figure 4.9 shows the SEM images obtained from the fine polished surfaces of $Si_{99}B_1$-Arc-SPS, $Si_{92}B_8$-Arc-SPS, and $Si_{92}B_8$-MS-SPS. A homogeneous phase is observed in the $Si_{99}B_1$-Arc-SPS in Fig. 4.9(a), which evidences the complete dissolution of B in the Si phase. In contrast, the SEM images of $Si_{92}B_8$-Arc-SPS and $Si_{92}B_8$-MS-SPS given in Figs. 4.9(b) and 4.9(c) show the presence of precipitates. These precipitates are considered to correspond to the SiB_3, which was demonstrated by the XRD analysis. Smaller precipitates (100–500 nm) are observed in $Si_{92}B_8$-MS-SPS compared with those in $Si_{92}B_8$-Arc-SPS (0.5–4 μm). Similar resultant size of precipitates is also confirmed by transmission electron micrograph of $Si_{92}B_8$-MS-SPS in Fig. 4.9(d). This difference was caused because the precipitates in $Si_{92}B_8$-MS-SPS were formed by solid-state phase transformation, which relies on solid-state diffusion.[3][15] The precipitates in $Si_{92}B_8$-Arc-SPS, meanwhile, were formed by liquid-solid phase transformation, which depends on liquid-state diffusion. It is thought that since diffusion in the solid state is considerably slower than that in the liquid state, a finer structure was formed in $Si_{92}B_8$-MS-SPS than in $Si_{92}B_8$-Arc-SPS.

In addition to the precipitation, the crystal grain size of the matrix phase is known to have a strong impact on the TE properties, especially on the thermal conductivity. Thus, the grain sizes in the Si matrices of the samples were studied by EBSD. Figs. 4.10(a) - (f) show the inverse pole-figure-mapping images and grain size distributions of the $Si_{99}B_1$-Arc-SPS, $Si_{92}B_8$-Arc-SPS, and $Si_{92}B_8$-MS-SPS samples, respectively, that were obtained from the EBSD analysis. The average grain sizes and geometric standard deviations were estimated from these images and found to be 13 μm ± 3 μm, 7 μm ± 2 μm, and 3 μm ± 1 μm for $Si_{99}B_1$-Arc-SPS, $Si_{92}B_8$-Arc-SPS, and $Si_{92}B_8$-MS-SPS, respectively. The grain size reductions may be attributed to the presence of SiB_3 since precipitates are known to pin grain boundaries and suppress grain growth. The rapid solidification may also have caused the grain size reduction for $Si_{92}B_8$-MS-SPS since rapid solidification tends to reduce the grain size.[16][17]

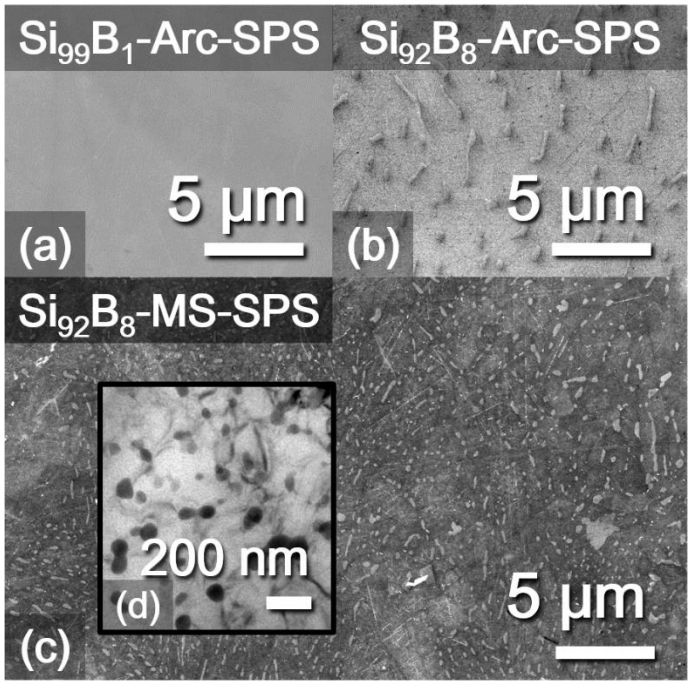

Fig. 4.9 Scanning electron micrographs of (a) $Si_{99}B_1$-Arc-SPS, (b) $Si_{92}B8$- Arc-SPS, and (c) $Si_{92}B_8$-MS-SPS. (d) Transmission electron micrograph of $Si_{92}B_8$-MS-SPS with a similar precipitates size.

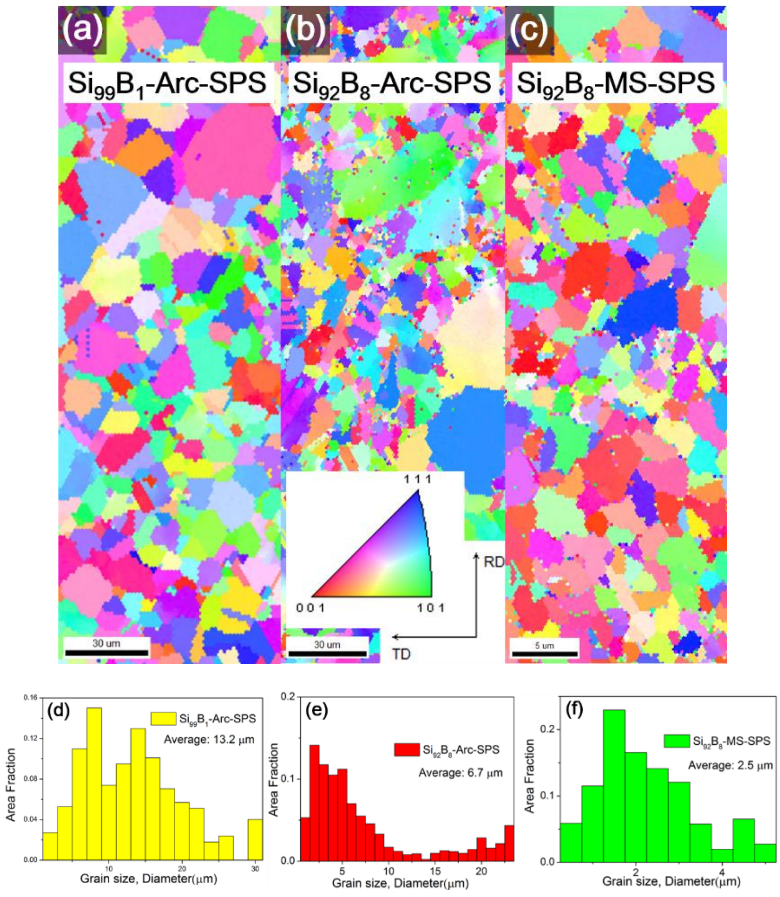

Fig. 4.10 Color-coded orientation maps and inverse pole figure of (a) $Si_{99}B_1$-Arc-SPS, (b) $Si_{92}B_8$-Arc-SPS and (c) $Si_{92}B_8$-MS-SPS sample. Grain size distribution of these samples are shown in (d), (e), (f), respectively.

II. Thermoelectric transport properties

To reveal the effects of the SiB_3 precipitation on the electrical transport properties of bulk Si-B composites, the Hall coefficients at RT were measured, and the carrier concentrations n_H and carrier motilities μ_H were calculated and are presented in Table 4.1. Assuming that all of the additional B atoms acted as dopants, the carrier concentration $Si_{99}B_1$ sample was estimated to be 5.0×10^{20} cm^{-3}. The carrier concentration of $Si_{99}B_1$-Arc was found to be 4.7×10^{20} cm^{-3}, which is almost identical to that of the completely dopant-activated $Si_{99}B_1$ (5.0×10^{20} cm^{-3}), indicating that almost all of the additional B atoms in $Si_{99}B_1$-Arc-SPS acted as dopants. The carrier concentrations of $Si_{92}B_8$-Arc-SPS and $Si_{92}B_8$-MS-SPS are almost equal to that of $Si_{99}B_1$-Arc-SPS. The carrier mobility of the $Si_{99}B_1$-Arc sample was found to be 36.5 $cm^2 \cdot V^{-1} \cdot s^{-1}$, which is comparable to the carrier mobility of single-crystal Si with the same impurity concentration (36 $cm^2 \cdot V^{-1} \cdot s^{-1}$).[18][19] The carrier mobilities of $Si_{92}B_8$-Arc-SPS and $Si_{92}B_8$-MS-SPS are slightly lower than that of $Si_{99}B_1$-Arc, possibly due to the presence of Si/SiB_3 interface.

The temperature dependences of the electrical resistivities of the $Si_{99}B_1$-Arc-SPS, $Si_{92}B_8$-Arc-SPS, and $Si_{92}B_8$-MS-SPS samples are shown in Fig. 4.11(a). The electrical resistivity of the $Si_{99}B_1$-Arc-SPS sample is 3.80 μΩ·m at RT and increases with temperature, reaching a value of 10.8 μΩ·m at 1073 K. This temperature dependence of the electrical resistivity is typical of a heavily doped semiconductor. While $Si_{92}B_8$-Arc-SPS shows an electrical resistivity similar to that of $Si_{99}B_1$-Arc-SPS, $Si_{92}B_8$-MS-SPS possesses an electrical resistivity slightly higher than that of $Si_{99}B_1$-Arc-SPS due to the reduction of the carrier mobility as well as the slightly lower carrier concentration. Figure 4.11(b) presents the temperature-dependent Seebeck coefficients of these samples. All samples show positive Seebeck coefficients across the whole temperature range, which indicates that all of the samples are p-type semiconductors. Nearly identical Seebeck coefficients are observed for all of the samples.

Figure 4.11(c) shows the temperature-dependent thermal conductivities of the samples. The lattice thermal conductivities were calculated from the thermal conductivities and electrical resistivities by the Wiedemann-Franz law. The Lorenz number for degenerate semiconductors, namely, 2.45×10^{-8} $W \cdot \Omega / K^2$, was used to evaluate the electronic contribution to the thermal conductivities. Figure 4.11(d) presents the lattice thermal conductivities corrected to 100% theoretical density using Shult's equation.[20] Since the electrical contribution was quite small compared to the lattice contribution, the density-corrected lattice thermal conductivities become slightly higher than the total thermal conductivities, as shown in Figs. 4.11(c) and 4.11(d). At 300 K, the $Si_{99}B_1$-Arc-SPS sample shows a κ_{lat} value of 36 $W \cdot m^{-1} \cdot K^{-1}$, while the values of κ_{lat} of the $Si_{92}B_8$-Arc-SPS and $Si_{92}B_8$-MS-SPS samples are 28 $W \cdot m^{-1} \cdot K^{-1}$ and 20 $W \cdot m^{-1} \cdot K^{-1}$, respectively, which correspond to 22% and 44% reductions in κ_{lat} compared to that of the $Si_{99}B_1$-Arc-SPS sample.

In heavily doped single-crystal semiconductors, heat transport is mainly dominated by phonon-phonon, phonon-electron, and impurity scattering. In Si-B composites, phonon transport is additionally affected by Si-Si grain boundary scattering and scattering due to the SiB_3 precipitates, which cause the differences between the lattice thermal conductivities of the samples shown in Fig. 4.11(d). In order to reveal the effects of the SiB_3 precipitates and Si-matrix grain size on the reduction of the lattice thermal conductivity, we calculated the thermal conductivity of the heavily B-doped Si by considering solely the Si-matrix grain size effect based on the Boltzmann transport equation. The effects of the precipitates can be evaluated by comparing the calculated and observed thermal conductivities.

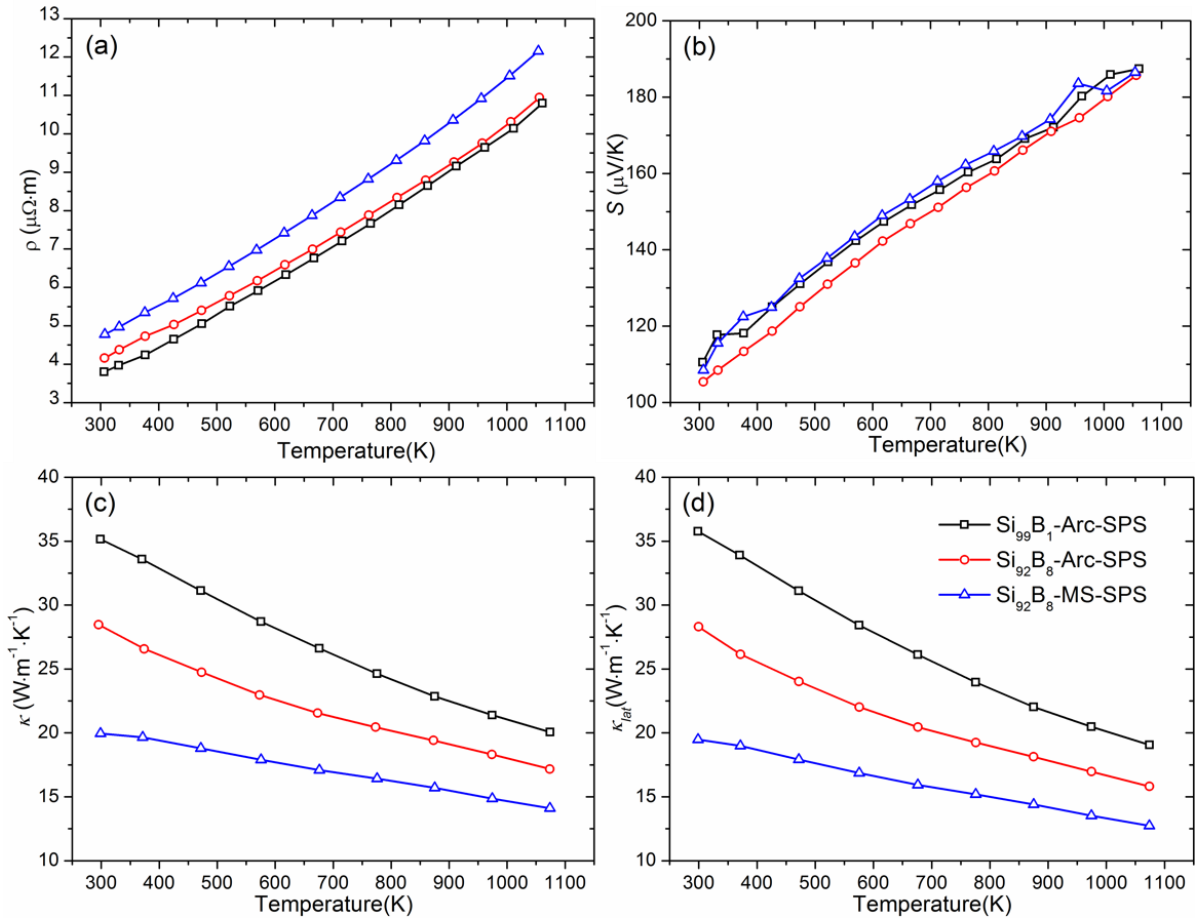

Fig. 4.11 Electrical and thermal transport measurements of $Si_{99}B_1$-Arc-SPS, $Si_{92}B_8$-Arc-SPS, and $Si_{92}B_8$-MS-SPS samples: (a) electrical resistivity ρ, (b) Seebeck coefficient S, (c) total thermal conductivity κ, and (d) lattice thermal conductivity κ_{lat} corrected to 100% theoretical density using Shult's equation.

Table 4.1 Density d, Relative density, Carrier concentration n_H, and Mobility μ_H of bulk Si-B composites at 300 K.

Sample name	d (g/ cm^3)	Relative density (%)	n_H (1/cm^3)	μ_H (cm^2·V^{-1}·s^{-1})
$Si_{99}B_1$-Arc-SPS	2.23	95.6	4.72×10^{20}	36.5
$Si_{92}B_8$-Arc-SPS	2.27	96.6	4.81×10^{20}	35.1
$Si_{92}B_8$-MS-SPS	2.28	96.9	4.63×10^{20}	32.2

The calculations were performed by adding the impurity, grain-boundary, and phonon-electron scattering terms to the model proposed by Morelli[21] that is based on the Debye-Callaway formalism[22] and can quantitatively reproduce the thermal conductivity of pure single-crystal Si. In this model, the lattice thermal conductivity is expressed by

$$\kappa_{lat} = \sum_i \frac{1}{3} C^i T^3 \int_0^{\theta^i/T} \frac{\tau_C^i(x) x^4 e^x}{\left(e^x - 1\right)^2} dx + \frac{1}{3} C^i T^3 \frac{\left(\int_0^{\theta^i/T} \frac{\tau_C^i(x) x^4 e^x}{\tau_N^i(x) \left(e^x - 1\right)^2} dx \right)^2}{\int_0^{\theta^i/T} \frac{\tau_C^i(x) x^4 e^x}{\tau_N^i(x) \tau_R^i(x) \left(e^x - 1\right)^2} dx} \tag{4.9}$$

where C^i is the lattice heat capacity, v^i is the phonon group velocity, θ^i is the Debye temperature, $(\tau_N)^{-1}$ is the scattering rate for normal phonon processes, $(\tau_c)^{-1}$ is the sum of all resistive scattering processes, and $(\tau_c)^{-1} = (\tau_N)^{-1} + (\tau_c)^{-1}$. The superscript notation i represents the phonon branch: one longitudinal (L) and two degenerate transverse (T) phonon branches. C^i and x are given by

$$C^i = \frac{k_B^4}{2\pi^2 \eta^3 v^i} \tag{4.10}$$

and

$$x = \frac{\eta \omega}{k_B T} \tag{4.11}$$

where η is the Planck constant, k_B is the Boltzmann constant, ω is the phonon frequency, and v^i is the phonon velocity of branch i. For a pure single crystal, the resistive scattering rate is assumed to be the sum of the scattering rates due to phonon-phonon umklapp scattering $\left(\tau_U^i\right)^{-1}$, point defect scattering $\left(\tau_{PDiso}^i\right)^{-1}$ due to the presence of isotopes, and scattering from the boundaries $\left(\tau_B^i\right)^{-1}$:

$$\left(\tau_R^i\right)^{-1} = \left(\tau_U^i\right)^{-1} + \left(\tau_{PDiso}^i\right)^{-1} + \left(\tau_B^i\right)^{-1}. \tag{4.12}$$

The functional forms of these scattering rates and the required parameters for pure single-crystal Si are given in Ref. s1 and are not reproduced here. In the present study, we added the scattering rates due to phonon-electron, grain-boundary scattering, and impurity scattering in order to calculate the thermal conductivity of the heavily B-doped polycrystalline Si:

$$\left(\tau_R^i\right)^{-1} = \left(\tau_U^i\right)^{-1} + \left(\tau_{PDiso}^i\right)^{-1} + \left(\tau_B^i\right)^{-1} + \left(\tau_{PDim}^i\right)^{-1} + \left(\tau_{GB}^i\right)^{-1} + \left(\tau_{pe}^i\right)^{-1} \tag{4.13}$$

where[23]

$$\left(\tau_{PDim}^i\right)^{-1} = \frac{V k_B^4 \Gamma}{4\pi \eta^4 v_i^3} x^4 T^4 \tag{4.14}$$

$$\left(\tau_{GB}^i\right)^{-1} = \frac{v_i}{D} \tag{4.15}$$

and[24]

$$\left(\tau_{pe}^i\right)^{-1} = \frac{E_{def}^2 m^{*3} v_i}{4\pi \eta^4 d} \left(\frac{k_B T}{\frac{1}{2} m^* v_i^2} \right) \left(\frac{\eta \omega}{k_B T} - \ln \frac{1 + \exp\left(\left(\frac{1}{2} m^* v_i^2 - E_F \right) \Big/ k_B T + \eta^2 \omega^2 / 8 m^* v_i^2 k_B T + \eta \omega / 2 k_B T \right)}{1 + \exp\left(\left(\frac{1}{2} m^* v_i^2 - E_F \right) \Big/ k_B T + \eta^2 \omega^2 / 8 m^* v_i^2 k_B T - \eta \omega / k_B T \right)} \right) \tag{4.16}$$

where V is the volume per atom, D is the grain size, E_{def} is the electron-phonon deformation potential, m^* is density-of-states effective mass, d is the density, and E_F is the Fermi energy. Γ is the phonon-scattering parameter which is expressed by[23]

$$\Gamma = \sum_j f_j \left\{ \left(\frac{M - M_j}{M} \right)^2 + \varepsilon \left[\frac{\delta - \delta_j}{\delta} \right]^2 \right\} \tag{4.18}$$

where M is the averaged atomic mass, M_j is the atomic mass of impurity j, f_i is the fractional concentration of the impurity, δ is the averaged cube root of the atomic volume, and δ_j is the cube root of the atomic volume of impurity j. Generally, ε is regarded as an adjustable parameter. We used literature or slightly modified values for all parameters other than ε, which was determined by fitting to the experimental value of $Si_{99}B_1$-Arc. The parameters used in the present study are summarized in Table 4.2

The calculated results are shown in Fig. 4.12, which indicates that the grain size does not affect the thermal conductivity when the grain size is larger than 1 μm. This result implies that the reductions of the lattice thermal conductivities of $Si_{92}B_8$-Arc-SPS and $Si_{92}B_8$-MS-SPS can be attributed mainly to the SiB_3 precipitates. The difference between the thermal conductivities of $Si_{92}B_8$-Arc-SPS and $Si_{92}B_8$-MS-SPS is considered to result from the different sizes of the SiB_3 precipitates.

The dimensionless figures of merit *ZT* of the Si-B composites are presented in Fig. 4.13. The $Si_{99}B_1$-Arc-SPS sample shows a linearly increasing *ZT* with rising temperature, reaching a value of 0.17 at 1073 K. While only a slight increase of *ZT* was observed for $Si_{92}B_8$-Arc-SPS, obvious improvement was achieved in the *ZT* value of $Si_{92}B_8$-MS-SPS compared to that of $Si_{99}B_1$-Arc-SPS. This result indicates that the TE performance increases with decreasing precipitate size. This increase is mainly due to the reduced thermal conductivity. The *ZT* value reaches 0.23 at 1073 K for $Si_{92}B_8$-MS-SPS.

The experimental data measured during both heating and cooling thermal cycles is shown in the Fig. 4.14. As can been seen, resistivity, Seebeck coefficient and total thermal conductivity obtained during heating and cooling cycles do not change significantly. Although it is probably that all the samples are doped beyond the solubility point of B in the measured temperature range, which indicates that equilibrium state was not reached, it is apparent from our results that these samples remain stable under 1073K.

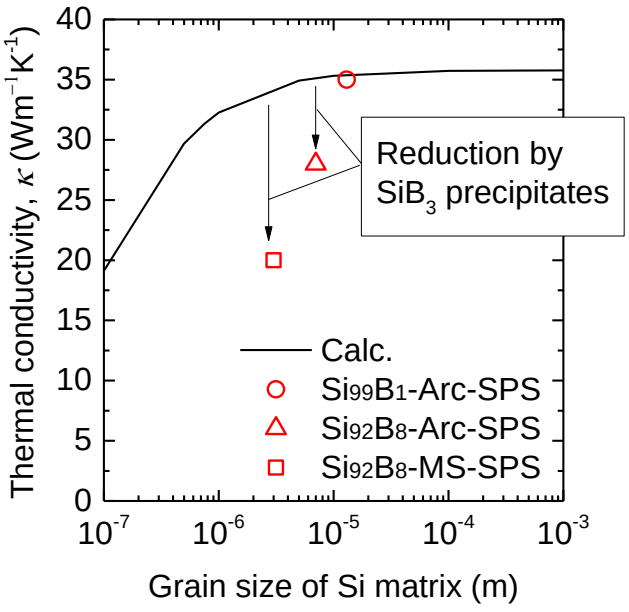

Fig. 4.12 Si-matrix grain-size dependence of lattice thermal conductivity of B-doped (5.0×10^{20} cm^{-3}) Si. Lattice

thermal conductivities of Si-B composites are shown together, and grain sizes were estimated by EBSD analysis.

Table 4.2 Electron-modeling parameters.

Property	Parameter	Value	Note
Sound velocity	v^L	8340 (m/s)	Ref.[21]
	v^T	5840 (m/s)	Ref.[21]
Debye temperature	θ^L	586 (K)	Ref.[21]
	θ^T	240 (K)	Ref.[21]
Volume per atom	V	9.47 (Å^3)	Evaluated from the lattice parameter 4.231 Å, which is estimated from the lattice parameter of B-doped Si.
Grain size	D	13 (μm)[a] 7 (μm)[a] 3 (μm)[a]	This study
Electron-phonon deformation potential	E_{def}	3 (eV)	Ref.[25]
Density-of-states effective mass	m^*	0.81· m_e (kg)	Ref.[26]
Fermi energy	E_F	0.28 (eV)	Estimated from the carrier density of 5×10^{20} cm^{-3} and the effective mass.
Density	d	2318 (kg/m3)	Estimated from the lattice parameter and averaged atomic mass of $Si_{99}B_1$.
Parameter relevant to impurity scattering	ε	6	Fitted to the experimental value of $Si_{99}B_1$-Arc-SPS.

[a] 13 μm for $Si_{99}B_1$-Arc-SPS, 7 μm for $Si_{92}B_8$-Arc-SPS, and 3 μm for $Si_{92}B_8$-MS-SPS.

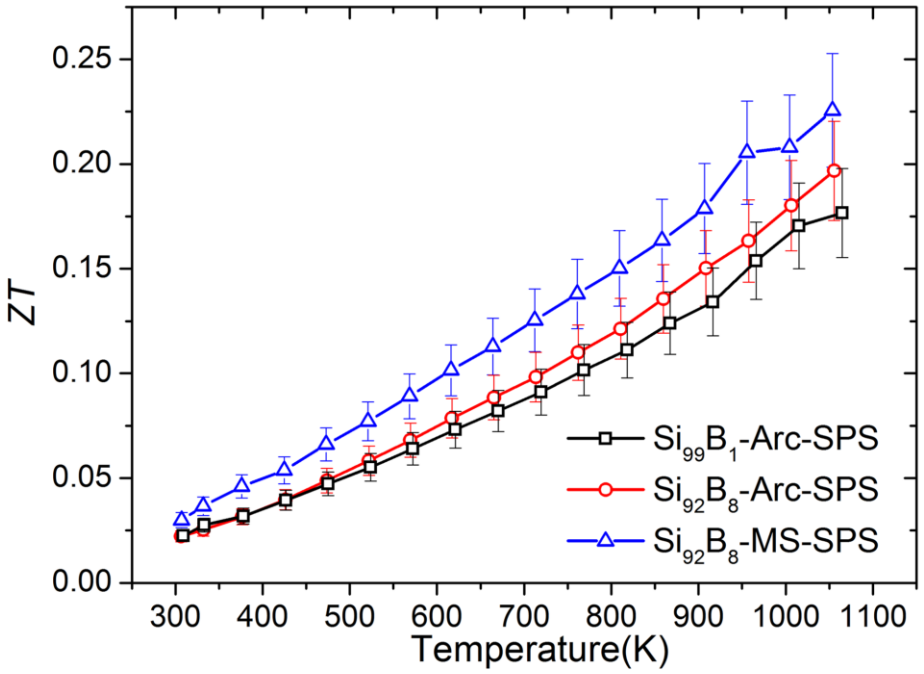

Fig. 4.13 Temperature dependence of *ZT* value of Si-B composites.

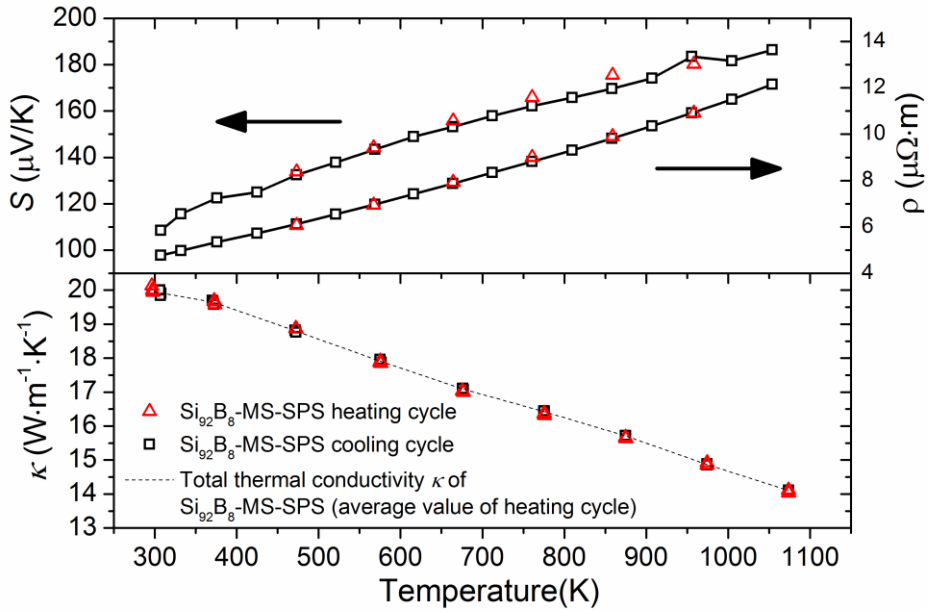

Fig. 4.14 The experimental data of $Si_{92}B_8$-MS-SPS measured during both heating and cooling thermal cycles. Total thermal conductivity κ was calculated by $\kappa = D \cdot d \cdot C$, where thermal diffusivity α is measured three times for every 100 K. Electrical resistivity ρ, Seebeck coefficient S and κ obtained during heating and cooling cycles do not change significantly.

4.3.3 Conclusion

We fabricated a Si-SiB_3 sub-micro composite by decomposing a Si-B supersaturated solid solution (Si:B = 92:8), which was prepared by rapid solidification followed by sintering. In this composite, sub-micro-sized SiB_3 precipitates (100–500 nm) were formed, which were significantly smaller than those formed by eutectic reaction, whose sizes were 0.5–4 μm. The Hall measurement revealed that the carrier concentration of the composite was around 5×10^{20} cm^{-3} and that the carrier mobility was slightly lower than that of single-crystal Si with the same carrier concentration. The electrical resistivity was slightly increased, and the Seebeck coefficient was not affected by the SiB_3 precipitates. In contrast to the electrical resistivity and the Seebeck coefficient, 44% reduction was observed in the lattice thermal conductivity when the sub-micro-sized SiB_3 precipitates were generated. The *ZT* increased with decreasing SiB_3 precipitate size, and a maximum *ZT* of 0.23 was obtained at 1073 K, which is 28% higher than that without SiB_3 precipitates. If smaller precipitates were generated, further improvement in the TE performance could be expected.

4.4 Si-Co system

4.4.1 Introduction

In this chapter, we attempted to synthesize Si/$CoSi_2$ composites. The phase diagram of Si-Co binary system is present in Fig. 4.15. Although $CoSi_2$ is a metallic silicide, which is not favorable for its use as a TE material, the similarity in crystal structures (See Fig. 4.16) and lattice parameters (mismatch within 1.2 % at RT and 0.5 % at more than 973 K based on the thermal expansion[27]) may reduce the density of interfacial dislocations[28] and result in the formation of a connected network for electron transport[29][30] when compared to complex icosahedra borides like SiB_3[11]. By using a rapid cooling technique, such as melt-spinning, a greater degree of supercooling can be achieved, leading to an increased nucleation rate and thereby possibly resulting in a fine microstructure[3].

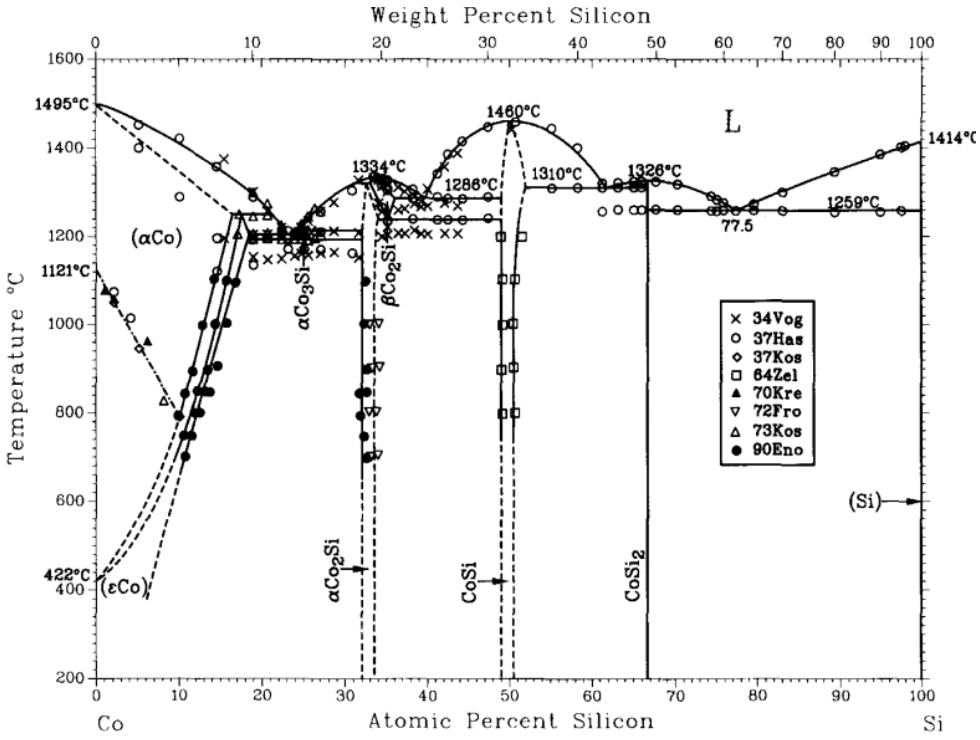

Fig. 4.15 Phase diagram of Si-Co binary system.[31]

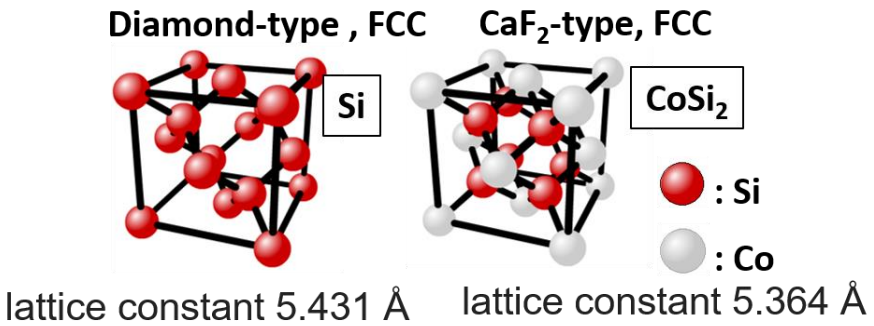

Fig. 4.16 Lattice structure of Si and $CoSi_2$.

4.4.2 Results and discussion

I. Phase-state and microstructure characterization

Figure 4.17 shows the powder X-ray diffraction patterns for the Si/$CoSi_2$-Arc, Si/$CoSi_2$-MS, Si/$CoSi_2$-Arc-SPS and MS-SPS samples from 20 to 80°. Very sharp Si peaks and week $CoSi_2$ peaks are identified, as expected from the Si-Co phase diagram. The XRD pattern of melt-spun ribbons shows a broad $CoSi_2$ peak, which suggests a smaller size of $CoSi_2$ precipitates. For all the as-sintered samples, very similar values of the lattice parameters were estimated from the XRD data (a=5.4205Å±0.0002Å for Si/$CoSi_2$-Arc-SPS, a =5.4207Å±0.0001Å for Si/$CoSi_2$-MS-SPS), which are in good agreement with a homogeneous B-doped Si ($Si_{0.99}B_{0.01}$-Arc-SPS, a=5.4205Å±0.0001Å) synthesized by a similar method in the previous study[32] as shown in Table 4.3. This result indicates the B-doped Si/$CoSi_2$ composites were successfully synthesized, which possibly possess a similar doping density considering the extremely low solubility of Co in Si.

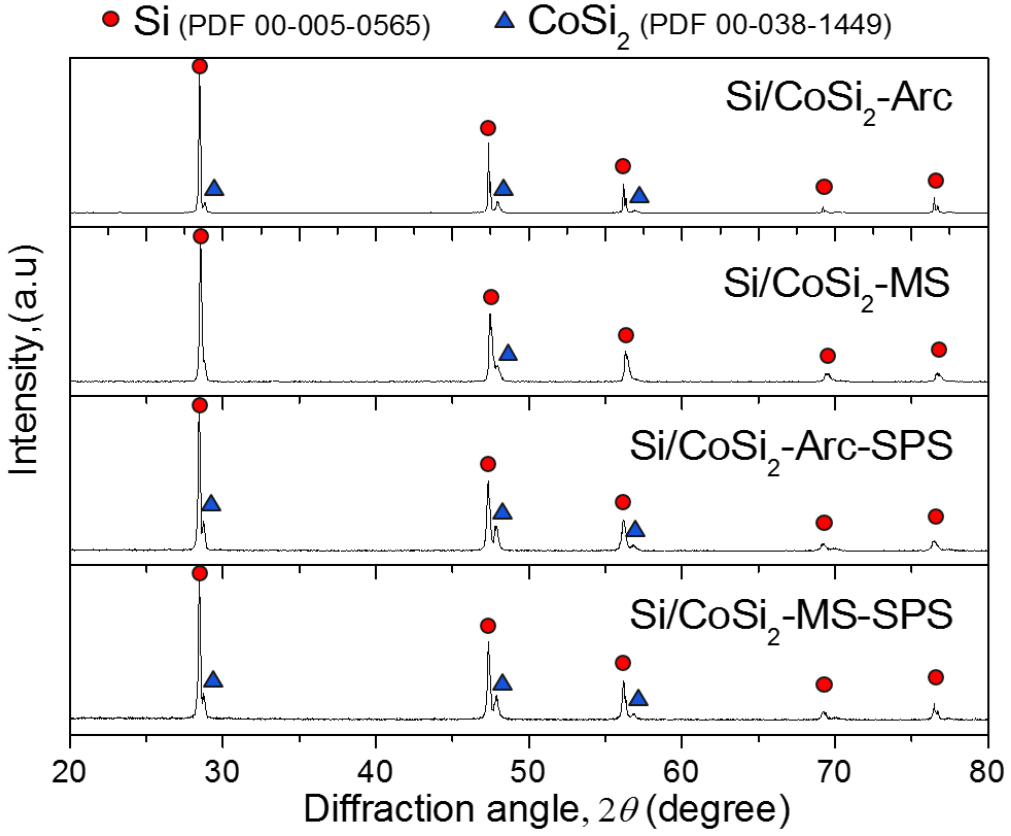

Fig. 4.17 XRD patterns of $(Si_{0.99}B_{0.01})_{95}Co_5$ samples prepared by different methods.

Table 4.3 Lattice parameter *a*, Density *d*, Relative density, Carrier concentration n_H, Mobility μ_H and lattice thermal conductivity κ_{lat} of bulk samples at 300 K.

Sample name	*a* (Å)	*d* (g/ cm^3)	Relative density (%)	n_H (10^{20}/cm^3)	μ_H (cm^2·V^{-1} ·s^{-1})	κ_{lat} (W·m^{-1} ·K^{-1})
$Si_{99}B_1$-Arc-SPS[32]	5.4205	2.23	95.6	4.72	36.5	35.8
Si/SiB_3-Arc-SPS[32]	5.4160	2.27	96.6	4.81	35.1	28.3
Si/SiB_3-MS-SPS[32]	5.4200	2.28	96.9	4.63	32.2	19.5
Si/$CoSi_2$-Arc-SPS	5.4205	2.43	93.8	4.87	35.2	38.8
Si/$CoSi_2$-MS-SPS	5.4207	2.44	94.4	4.83	33.1	30.0

Scanning electron micrographs of $(Si_{0.99}B_{0.01})_{95}Co_5$ samples are shown in Fig. 4.18. Phase separation can be clearly seen, namely the dark and light regions, in all samples. According to the XRD analysis, these dark and light regions are considered to correspond to the Si and $CoSi_2$ precipitates, respectively. This also will be studied by TEM-EDS analysis, as shown later. Significant different sizes and morphologies of the precipitates are observed in the Arc sample and the MS ribbon. Nano-scale precipitates (<100 nm) were formed in the MS compared with the large lamellar structures found on the grain boundary in the Arc sample. The structural refinement of the melt-spun ribbon is the consequence of the high cooling rate of MS technique which can enhance the nucleation, as demonstrated previously [3]. For the as-sintered samples, the growth of the $CoSi_2$ are found in both Si/$CoSi_2$-Arc-SPS and Si/$CoSi_2$-MS-SPS, which leads to final precipitates sizes of 1-10 μm and 50-200 nm , respectively. Since the growth kinetics of precipitates in solid at high temperature is well understood as a diffusion-controlled process[33], the quite high diffusion coefficient of Co atom in Si (>10^{-5} cm^2/s at the sintering temperature in this study[34]) may result in a high growth rate of those precipitates compared to that of B atom(<10^{-10} cm^2/s at the sintering temperature in this study[35]) during SPS process. Although the grain growth of $CoSi_2$ in MS-SPS shown in the Fig. 4.18 seems more obvious than that in Si/$CoSi_2$-Arc-SPS, the precipitate size is still much smaller in the Si/$CoSi_2$-MS-SPS. Thus, lower thermal conductivity is expected for Si/$CoSi_2$-MS-SPS than Si/$CoSi_2$-Arc-SPS via phonon scattering by these sub-micro precipitates.

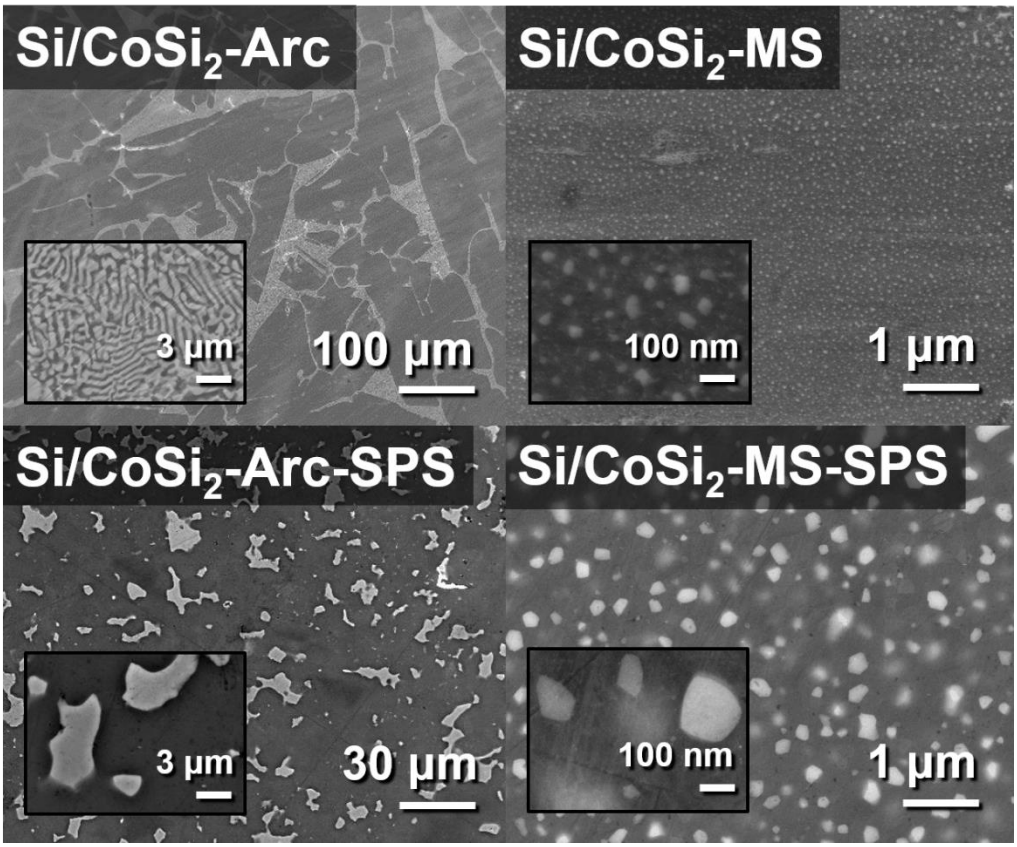

Fig. 4.18 Scanning electron micrographs of $(Si_{0.99}B_{0.01})_{95}Co_5$ samples.

In order to verify the size and composition of precipitates in MS-SPS determined previously, a brief TEM analysis was performed, as shown in Fig. 4.19, the TEM bright-field image shown in Fig. 4.19(a-c) revealed the precipitates size of several dozes nm to 500 nm. Strains and dislocations were occasionally observed in Si matrix around the $CoSi_2$ precipitates (Fig. 4.19(b)). The relatively large areal dislocation density can be attribute to the large difference in the thermal expansion coefficient between Si ($2.6\sim4.5 \times 10^{-6}K^{-1}$, RT~1373K)[36] and $CoSi_2$ (about $14 \times 10^{-6}K^{-1}$, 400K~1050K)[37], which may result in strong stress to generate dislocations during cooling [38]. However, due to the low overall dislocation density, as shown in Fig. 4.19(a), the influence of strains and dislocations on carrier/phonon transport was considered to be ignorable in the present work. TEM-EDS analysis reveals that the precipitates consists of a considerable amount of both Si and Co, as shown in Fig. 4.19(d). Although quantitative analysis of composition is difficult since we couldn't find a region where only precipitate exists, this result confirms the precipitates observed by SEM and TEM are Co-Si compound, which can be specifically inferred as $CoSi_2$ from XRD analysis.

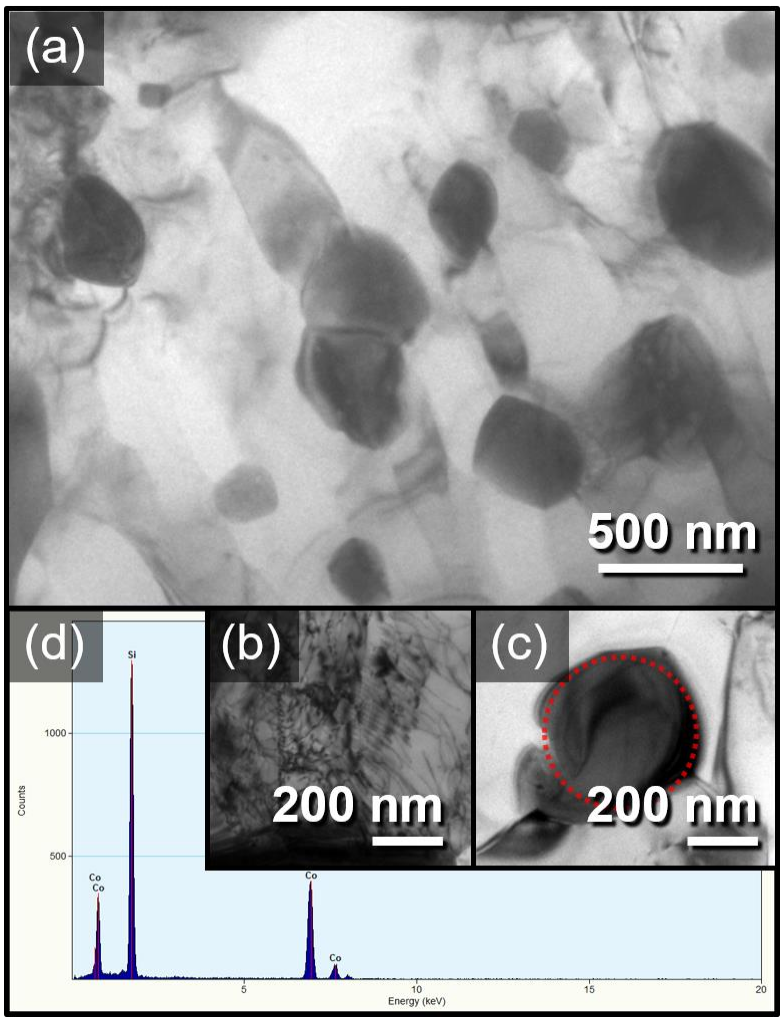

Fig. 4.19 (a, b, c) Bright-field TEM image and (d) EDS spectrum of MS-SPS. The region surrounded by a red dashed circle in Fig. 4.19 (c) corresponds to the $CoSi_2$ precipitates, where the EDS analysis was conducted.

II. Thermoelectric transport properties

Table 4.3 lists the carrier concentrations n_H and carrier motilities μ_H of the bulk Si/$CoSi_2$ composites together with the literature values for 1% B-doped Si ($Si_{99}B_1$-Arc-SPS) and Si/SiB_3 composites prepared by Arc-SPS and MS-SPS (Si/SiB_3-Arc-SPS and Si/SiB_3-MS-SPS, respectively) [32]. Notice that Si/$CoSi_2$ composites have n_H of ~4.8 × 10^{20} cm^{-3}. Those values are slightly higher than the literature value of ~4.7 × 10^{20} cm^{-3} for the homogeneous $Si_{99}B_1$-Arc-SPS and very close to that of the completely dopant-activated $Si_{99}B_1$ with an estimated carrier concentration of 5 × 10^{20} cm^{-3}. Thus, most of the B atoms in these composites are considered to act as dopants. For μ_H, all the Arc-SPSed sample show comparable values (36.5 $cm^2V^{-1}s^{-1}$ for $Si_{99}B_1$-Arc-SPS, 35.1 $cm^2V^{-1}s^{-1}$ for Si/SiB_3-Arc-SPS and 35.2 $cm^2V^{-1}s^{-1}$ for Si/$CoSi_2$-Arc-SPS) to that of single-crystal Si with a same doping level (36 $cm^2V^{-1}s^{-1}$)[19]. Yet, a slightly lower μ_H of 33.1 $cm^2V^{-1}s^{-1}$ was found in Si/$CoSi_2$-MS-SPS. This possibly attribute to the presence of sub-micro $CoSi_2$ precipitates. On the other hand, compared to that of the Si/SiB_3 sub-micro composite (μ_H = 32.2 $cm^2V^{-1}s^{-1}$, as shown as Si/SiB_3-MS-SPS in Tab. I) with a lower n_H of 4.6 × 10^{20} cm^{-3} and a similar precipitates size of 100 - 500 nm, the reduction of μ_H in the Si/$CoSi_2$ sub-micro composite was found to be

mitigated. Compared to the very different structure of Si and SiB_3, the structural similarity of Si and $CoSi_2$ probably result in a suppression of carriers scattering due to the reduction of interfacial defects at their interfaces, as mentioned previously.

The temperature dependence of σ and S for the $Si_{99}B_1$-Arc-SPS [32], Si/$CoSi_2$-Arc-SPS and Si/$CoSi_2$-MS-SPS are shown in Figs. 4.20 (a) and (b), respectively. As the temperature increased, the value of σ decreased and S increased, showing a typical behavior of *p*-type heavily-doped semiconductor. Compared to the $Si_{99}B_1$-Arc-SPS, the Seebeck coefficients in both Si/$CoSi_2$-Arc-SPS and Si/$CoSi_2$-MS-SPS slightly decreased (the Si/$CoSi_2$-Arc-SPS having $S = 1.7 \times 10^2$ μV/K compare to the homogeneous $Si_{99}B_1$-Arc-SPS $S = 1.9 \times 10^2$ μV/K at 1073K), while the electrical conductivities of the composites slightly increase at high temperature (1.2×10^5 S/m for the Si/$CoSi_2$-Arc-SPS compared to 9.3×10^4 S/m for the $Si_{99}B_1$-Arc-SPS at 1073K). Such behavior can be explained by the higher n_H in Si/$CoSi_2$-Arc-SPS and Si/$CoSi_2$-MS-SPS sample than that of $Si_{99}B_1$-Arc-SPS.

The lattice thermal conductivities κ_{lat} were calculated from the thermal conductivity and measured electrical conductivity by using the Wiedemann-Franz law, i.e., $\kappa_{lat} = \kappa - LT\sigma$, where L is the Lorenz number ($L = 2.45 \times 10^{-8}$ $W \cdot \Omega \cdot K^{-2}$). Fig. 4.20 (c) shows the temperature-dependent lattice thermal conductivities κ_{lat} of the samples. As shown in Fig. 4.20 (c), the κ_{lat} of Si/$CoSi_2$-Arc-SPS is higher than the $Si_{99}B_1$-Arc-SPS. Since $CoSi_2$ possesses a high thermal conductivity of over 40 $W \cdot m^{-1} \cdot K^{-1}$ in the certain temperature range[39], the presence of the $CoSi_2$ is considered to be responsible for the increased κ_{lat} in the Si/$CoSi_2$-Arc-SPS. When compared to the κ_{lat} of Si/$CoSi_2$-Arc-SPS, over 20% reduction was found in Si/$CoSi_2$-MS-SPS, which can be attributed to the enhanced phonon scattering due to sub-micro $CoSi_2$ precipitates. It is also found that the κ_{lat} of Si/$CoSi_2$ composites show considerably higher κ_{lat} than Si/SiB_3 composites by both Arc-SPS and MS-SPS, as shown in Table 4.3. This can be explained by the difference in thermal conductivity between metallic $CoSi_2$ and nonmetallic SiB_3 with an extremely low thermal conductivity (<2 $W \cdot m^{-1} \cdot K^{-1}$ from RT to 973K)[40]

Fig. 4.20 (d) presents the temperature dependence of the dimensionless figure of merit *ZT*. For the Si/$CoSi_2$-Arc-SPS, the *ZT* shows a comparative value to that of the $Si_{99}B_1$-Arc-SPS, while about 16% enhancement of *ZT* was achieved in the Si/$CoSi_2$-MS-SPS, showing a maximum value of 0.21 at 1073K. This result suggests that the TE performance of the Si/$CoSi_2$ composites increases with size reduction of precipitates. Compared to Si/SiB_3 composites, although the high intrinsic thermal conductivity of metallic $CoSi_2$ may partially compensate the size effect of itself on the phonon transport, a considerable enhancement in *ZT* can be still achieved owing to the suppression of mobility degradation.

The experimental data measured during both heating and cooling thermal cycles is shown in the Fig. 4.21. As can been seen, resistivity, Seebeck coefficient and total thermal conductivity obtained during heating and cooling cycles do not change significantly.

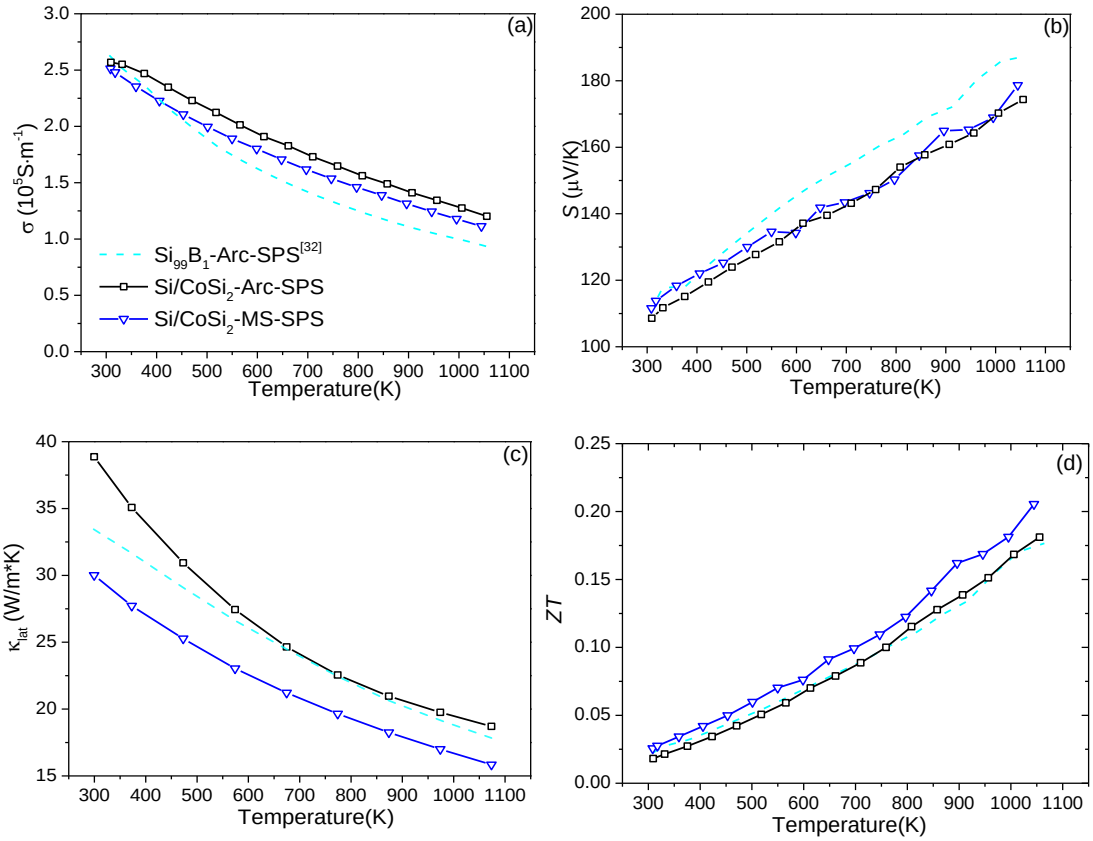

Fig. 4.20 Electrical and thermal transport measurements of $Si_{99}B_1$-Arc-SPS, Si/$CoSi_2$-Arc-SPS, and Si/$CoSi_2$-MS-SPS samples: (a) electrical conductivities σ, (b) Seebeck coefficient S, (c) lattice thermal conductivity κ_{lat} and (d) the dimensionless figure of merit ZT.

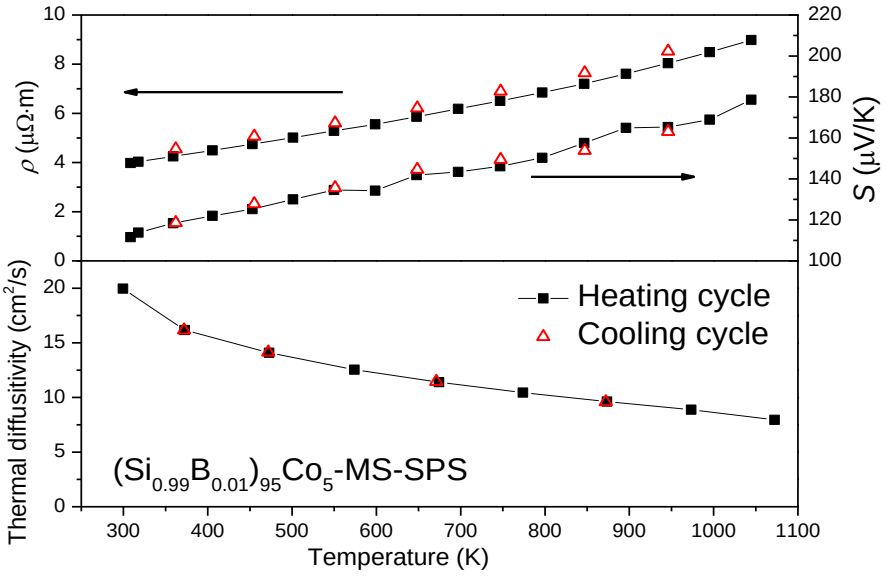

Fig. 4.21 The experimental data of $Si_{92}B_8$-MS-SPS measured during both heating and cooling thermal cycles.

4.4.3 Conclusion

In conclusion, we have herein presented a simple self-assembly process to synthesize $(Si_{0.99}B_{0.01})_{95}Co_5$ sub-micrometer-sized composites. Via rapid cooling by melt spinning (MS) followed by spark plasma sintering (SPS), sub-micrometer $CoSi_2$ inclusions spontaneously formed within bulk Si by precipitation. Compared to the coarse $CoSi_2$ phase (1-10 μm) in samples prepared by arc melting and SPS, these sub-micrometer precipitates (50-500 nm) were found to more effectively reduce thermal conductivity through enhanced phonon scattering on the precipitate/matrix interfaces. We also showed that the synthesized $Si/CoSi_2$ system could retain the electrical performance of the composites. Thus, despite the negative impact of the metallic inclusions on the controlled reduction in thermal transport, an increase in the figure of merit of about 16 % was achieved in the $Si/CoSi_2$-MS-SPS composite. We believe that further enhancement of TE performance is possible by optimization of the size and volume fraction of microstructures.

4.5 Reference

[1] K. Yee, S. LeBlanc, E. Goodson, C. Dames, *Energy Environ. Sci.* **2013**, *6*, 2561.

[2] T. Ikeda, L. Haviez, Y. Li, G. J. Snyder, *Small* **2012**, *8*, 2350.

[3] N. Heinz, T. Ikeda, Y. Pei, J. Snyder, *Adv. Funct. Mater.* **2014**, *24*, 2135.

[4] J. . Embury, R. . Fisher, *Acta Metall.* **1966**, *14*, 147.

[5] N. Heinz, T. Ikeda, J. Snyder, *Acta Mater.* **2012**, *60*, 4461.

[6] W. Luo, H. Li, Y. Yan, Z. Lin, X. Tang, Q. Zhang, C. Uher, *Intermetallics* **2011**, *19*, 404.

[7] D. Porter, K. Easterling, *Phase Transformations in Metals and Alloys*, **1992**.

[8] D. Turnbull, *Metall. Trans. B* **1981**, *12*, 217.

[9] H. Toraya, *J. Appl. Crystallogr.* **1986**, *19*, 440.

[10] M. Niranjan, *Comput. Mater. Sci.* **2014**, *95*, 517.

[11] T. Aselage, *J. Mater. Res.* **1998**, *13*, 1786.

[12] A. Mostafa, M. Medraj, *Materials (Basel).* **2017**, *10*, 676.

[13] C. Brosset and B. Magnusson, *Nature* **1960**, *187*, 1048.

[14] F. Trumbore, *Bell Syst. Tech. J.* **1960**, *39*, 205.

[15] T. Ikeda, L. A. Collins, V. A. Ravi, F. S. Gascoin, S. M. Haile, G. J. Snyder, **2007**, 763.

[16] X. Zhao, H. Chen, E. Müller, C. Drasar, *J. Alloys Compd.* **2004**, *365*, 206.

[17] B. Du, H. Li, J. Xu, X. Tang, C. Uher, *J. Solid State Chem.* **2011**, *184*, 109.

[18] Y. Ohishi, K. Kurosaki, T. Suzuki, H. Muta, S. Yamanaka, N. Uchida, T. Tada, T. Kanayama, *Thin Solid Films* **2013**, *534*, 238.

[19] G. Masetti, M. Severi, S. Solmi, *IEEE Trans. Electron Devices* **1983**, *30*, 764.

[20] B. Schulz, *High Temp. High Press.* **1981**, *14*, 649.

[21] T. Morelli, P. Heremans, A. Slack, *Phys. Rev. B* **2002**, *66*, 195304.

[22] J. Callaway, *Phys. Rev.* **1959**, *113*, 1046.

[23] B. Abeles, *Phys. Rev.* **1963**, *131*, 1906.

[24] E. Steigmeier, B. Abeles, *Phys. Rev.* **1964**, *136*, A1149.

[25] R. Shanks, D. Maycock, H. Sidles, C. Danielson, *Phys. Rev.* **1963**, *130*, 1743.

[26] M. Lundstrom, *Fundamentals of Carrier Transport, 2nd Ed.*, Cambridge University Press, Cambridge, United Kingdom, **2000**.

[27] D. Smeets, A. Vantomme, K. De Keyser, C. Detavernier, C. Lavoie, *J. Appl. Phys.* **2008**, *103*, 1.

[28] G. Stringfellow, *J. Appl. Phys.* **1972**, *43*, 3455.

[29] K. Biswas, J. He, Q. Zhang, G. Wang, C. Uher, V. P. Dravid, M. G. Kanatzidis, *Nat. Chem.* **2011**, *3*, 160.

[30] L.-D. Zhao, V. Dravid, M. Kanatzidis, *Energy Environ. Sci.* **2014**, *7*, 251.

[31] K. Ishida, T. Nishizawa, M. Schlesinger, *J. Phase Equilibria* **1991**, *12*, 578.

[32] J. Xie, Y. Ohishi, Y. Miyazaki, A. Yusufu, H. Muta, K. Kurosaki, S. Yamanaka, *J. Appl. Phys.* **2015**, *118*, 65103.

[33] F. Ham, *J. Phys. Chem. Solids* **1958**, *6*, 335.

[34] E. Weber, *Appl. Phys. A Solids Surfaces* **1983**, *30*, 1.

[35] G. Vick, K. Whittle, *J. Electrochem. Soc.* **1969**, *116*, 1142.

[36] Y. Okada, Y. Tokumaru, *J. Appl. Phys.* **1984**, *56*, 314.

[37] D. Smeets, G. Vanhoyland, J. D'Haen, a Vantomme, *J. Phys. D. Appl. Phys.* **2009**, *42*, 235402.

[38] R. Arsenault, N. Shi, *Mater. Sci. Eng.* **1986**, *81*, 175.

[39] G. Laboratories, S. Road, **1984**, *69*, 207.

[40] M. Mukaida, T. Goto, T. Hirai, *Mater. Manuf. Process.* **1992**, *7*, 625.

5. Naturally decorated dislocations capable of enhancing multiple phonon scattering in Si-based thermoelectric composites

5.1 Introduction

To further suppress κ_{lat}, one possible strategy is to introduce multi-scaled scattering centers targeting the wide-spectrum phonons. Recently, a so-called panoscopic approach has attracted increasing attention as a promising route to further suppress κ_{lat} via multi-scaled scattering centers targeting the wide-spectrum phonons with different frequency (ω), as show in Figure 5.1. Based on an all-scale hierarchical architecturing structure with various microstructural constituents, containing meso-scale grains, nanoscale precipitates and substitutional impurities, this approach has achieved a significant reduction in κ_{lat} such as PbTe/PbSe[1][2], contributing to a dramatic increases of *ZT*. Among all the potential candidates for assembling a hierarchical structure, we primarily focus on dislocations and related strain fields. The effect of them on TE properties are rarely experimentally investigated for their undesired role as carrier scattering centers in semiconductors as well as the insufficient thermal stability at the elevated temperature[3][4].

Chen proved that if the density of dislocations reaches a high degree (i.e., 10^{10}–10^{11} cm^{-2} for bulk Si at room temperature[5]), they play a prominent role in improving thermoelectric figure-of-merit *ZT*. This is due to enhanced phonon scattering, regardless of the negative impact of dislocations on carrier transport properties. The approximate frequency-dependent terms for the mean free path of dislocations ($\Lambda_{DC}^{-1} \propto \omega^3$) and related strains ($\Lambda_{DS}^{-1} \propto \omega$) have been proposed to predict their contributions to phonon scattering [6] (see 4. 12 for details). They are experimentally demonstrated as effective scattering centers for medium to high-frequency phonons, which is favorable from the viewpoint of all-scale hierarchical architectures as the target phonons are different from those of other structures. Nanoprecipitates effectively scatter low- and medium-frequency phonons, boundaries scatter low-frequency phonons, and impurities scatter high-frequency phonons[7][8][9][10]. This makes high-density dislocations attractive additional constituents for typical hierarchical architectures to accomplish a wider frequency spectrum for phonon scattering.

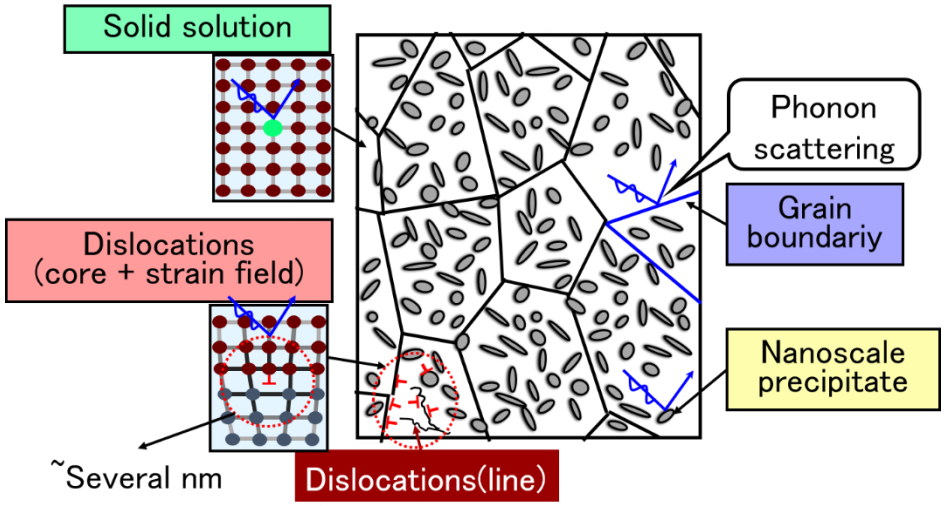

Fig. 5.1 Schematic illustration of all length-scale structures for high performance TE systems where major contributing factors for reducing the lattice thermal conductivity are indicated.

5.1.1 Impact of dislocations on the heat-carrying phonon transport

The effect of dislocations on the heat-carrying phonon transport still remains largely unclear. Although dislocations have an atomic-scale origin, their effects often extend several nanometers in length away from its core in terms of strain field. Specifically, three additional scattering centers can be simultaneously induced: (1) dislocation core-induced strain field; (2) propagating strain fields and dislocation cores associated with a dynamic interaction between dislocations (multiplication process of dislocation); (3) nanoscale inclusions due to impurities segregation along the dislocation lines. It is therefore difficult to independently study each type of dislocation-induced microstructure to obtain a widely-accepted with physically realistic parameters. Current models consider dislocation scattering as a combined mechanism including atomic- and sub-nanometer scale scattering, for example, though long-range interaction with strain field of the dislocation lines or the short-range interaction with of the dislocation cores. A specific expression for Λ_{DC}^{-1} (core of dislocation) and Λ_{DS}^{-1} (strain field of dislocation) with randomly distributed dislocations are given by[8][11]

$$\Lambda_{DC}^{-1} = N_d \frac{V_0^{4/3}}{v^3}\omega^3, \tag{5.1}$$

$$\Lambda_{DS}^{-1} = 0.6\frac{B_d^2\gamma^2\omega}{v}\left\{\frac{1}{2}+\frac{1}{24}\left(\frac{1-2r}{1-r}\right)^2\left[1+\sqrt{2}\left(\frac{v_L}{v_T}\right)^2\right]^2\right\}, \tag{5.2}$$

where N_d is dislocation density of all types, V_0 volume per atom, B_d magnitude of Burgers vector of edge dislocations, γ Grüneisen parameter and r poisson ratio. Note that the frequency dependence of phonon scattering on strain fields is $\sim\omega$ and dislocation cores is $\sim\omega^3$, making this mechanism particularly effective at scattering medium to high-frequency phonons. Although the actual frequency dependence of dislocation scattering rates still remains controversial, and the effect of the other dislocation parameters (ex. Burgers vector and dislocation line orientation) is not well understood and requires further investigation, dislocations with a density over 10^{10} cm^{-2} have been proved theoretically[5] and experimentally[7][8][9][10] to play an important role in lowering the thermal conductivity. Fig. 5.2 shows that a simplified model for the evaluation of additional phonon scattering from dislocations. Modeling predicts a noticeable effect of dislocations when their density > 10^{10} cm^{-2} and highly effective density for dislocation-induced phonon scattering is > 10^{11} cm^{-2}, which agrees well with the conclusion from the study employing first principle calculation[5].

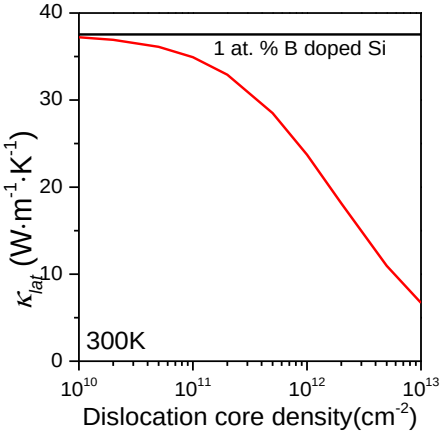

Fig. 5.2 Calculated κ_{lat} of SC Si doped with 1 at. % boron embed with dislocations as a function of dislocation core density at 300K. The calculated κ_{lat} of heavily doped Si is shown by the horizontal line for comparison.

5.1.2 Self-organization of Dislocation for thermoelectric materials

Dislocation self-organization processes can be described as the net result of the following sequential processes: (1) the generation of dislocations, (2) their movement through the crystal until they are stopped and their storage or annihilation in the latter areas such as hetero-interfaces, sub-grain and grain boundaries.

I. Generation of dislocations

The most straightforward way to introduce dislocations into a material is through plastic deformation. However, since most thermoelectrics including Si do not readily plastically deform at room temperature, simplify performing a mechanical external work may lead to a potential susceptibility to cracking or fracture.

Recent experimental works have contributed three methods that successfully introduced dislocation with a sufficient density in phonon scattering: (1) Intragranular dislocation lines formed by collapse of vacancies discs[7][9], (2) Release of plastic strain on semicoherent interface between matrix and precipitates[12][13] and (3) Dense dislocation arrays formed at low-energy grain boundaries by liquid-phase sintering[8][14]. Among these approach, intragranular dislocations are expected to have much larger strain fields than dislocations located on the interface[3], which may contribute to a stronger phonon scattering. Therefore, since the efficacy of intragranular dislocation remain uninvestigated in Si, we attempts to develop a novel strategy to self-assembly introduce dense dislocations into bulk Si.

In our case, melt-spinning technique was employed to synthesize pre-embed nanosilicides in Si matrix, instead of at grain boundary for the well-known formation mechanism by a typical liquid-phase sintering. At elevated temperature during SPS, it is possible that a liquid phase was temporarily generated by the eutectic reaction between silicides and Si matrix. The dislocations will form after the solidification of eutectic melt as a result of non-equilibrium impurity trapping in the matrix. This mechanism is explained as a lattice-deformation-induced route, because the impurity trapped by a matrix may change its lattice parameters.

Another potential route for introducing dislocation into Si is based on Si-vacancy injection. During SPS, it is possible that diffusing cobalt would react with Si probably at the Si/metal-silicide interface, to complete the metal-silicide formation and cause vacancy injection[15][16]. In addition, the vacancy supersaturations was found enhanced by increasing the density of Si/metal-silicide interface after a high temperature annealing. Therefore, as effective sources for vacancies, if high-density Si/metal-silicide interfaces can be introduced to Si, a condensation of the vacancy supersaturation may induce intragranular defects, such as stacking faults and dislocations[17]. The non-equilibrium melt spinning processing has been demonstrated in chapter 4.4 as an effective way to embed Co atom into Si matrix as uniformly-distributed nanoscale $CoSi_2$, generating a high-density Si-$CoSi_2$ interface due to a higher cooling rate. Hence, in this chapter, the Si-Co system is employed to investigate the self-assemble generation of dislocations.

II. Immobilization, Multiplication and Annihilation of dislocations

Frank–Read source is the most wildly-known mechanism for dislocation multiplication [18]. In particular, when apply stress to a gliding dislocation segment pinned at a localized source, the mobile segment moves lead to a complete loop while restoring the original configuration. This source can repeatedly emit a large amount of dislocations on the slip plane. Some other mechanism like double cross-slip[19] and Bardeen and Herring[20] can also act as the source for dislocation generation. These sources act as dislocation multiplication sites and are diffusion-limited processes.

In addition, dislocations in ionic crystals can have an electrostatic charge to interact with ionized atomic defects[3]. For instance, ionized phosphorus atoms have a very strong pinning effect on dislocations due to electrostatic interaction with acceptor sites on the dislocation in n-type Si[21]. These defects can serve the double role for the high density of residual dislocations by pinning the dislocations as the multiplication source and preventing the dislocations from annihilation with each other or storage at grain boundaries. Motivated by the above-mentioned feature phosphorus doping are chosen for further investigation.

5.1.3 Si-P system

Phosphorus is the most widely used dopant for Si-based thermoelectric material owing to (1) better thermoelectric performance in n-type Si; (2) high solubility that enables the optimization of carrier concentration (even though the actual solubility of phosphorus in Si remains an ongoing debate, as shown in figure 5.3[22][23]); (3) precipitation of P-rich phase at elevated temperature that may induce additional phonon scattering center. A previous study has presented a simple bottom-up method combing a conventional arc-melting process with subsequent spark-plasma sintering, which succeed in introducing high-density nanoscale Si monophosphate(SiP) in super-heavily P-doped Si with a nominal composition of $Si_{100}P_3$[24]. As shown in figure 5.4, these precipitates with size ranging from 5 nm to 20 nm are found uniformly distributed in the samples which strongly hindered the phonons transport and contributed to an improved *ZT* of 0.35 by lowing the lattice thermal conductivity.

In this chapter, we present a similar excess doping with 3 at.% phosphorus in the $Si/CoSi_2$ composite. Since we have presented a non-equilibrium strategy for extending the dopant solubility, a fine microstructure of SiP precipitates can be obtained. These nanoscale precipitates are also considered as an important component for assembling a hierarchical structure to hinder a wider spectrum of heat-carrying phonons.

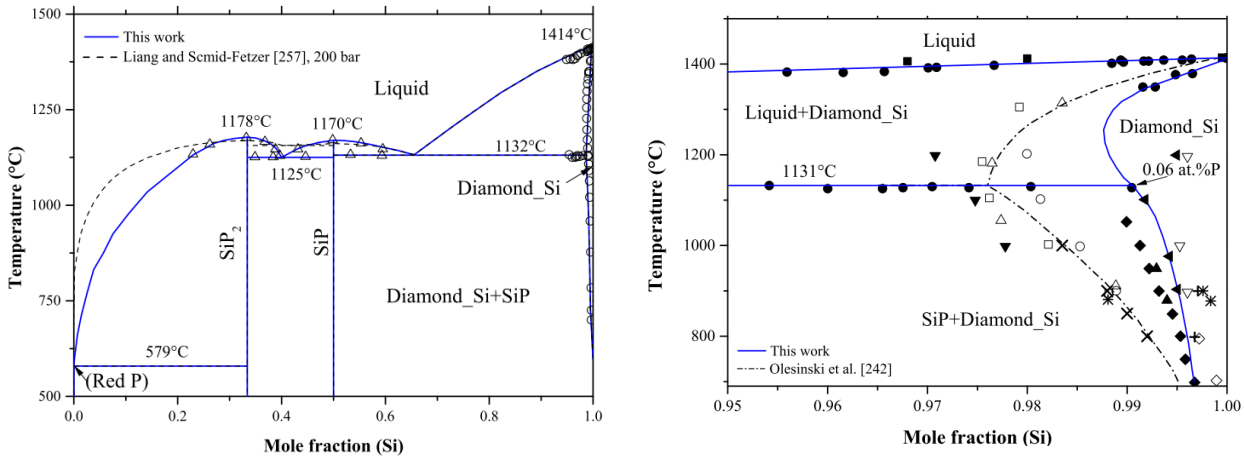

Fig. 5.3 Phase diagram of Si-P binary system. The right figure presents the enlarged area of Si-rich composition.[23]

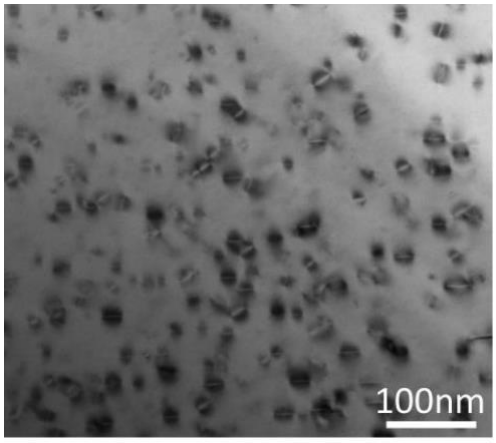

Fig. 5.4 TEM image of the SiP precipitates in the bulk $Si_{100}P_3$ sample reported by A. Yusufu.[24]

5.2 Experimental procedures

5.2.1 Synthesis

Ingots with nominal composition $(Si_{0.97}P_{0.03})_{95}Co_5$ were synthesized by Arc-melting with stoichiometric amounts of elemental Si (11N), Co (3N), and P (6N) in an Ar atmosphere. These ingots were melt spun to obtain super-cooled ribbons, which were collected in a graphite die and sintered by SPS method. The sintering temperature and time were 1323 K–1423 K and 2 min, respectively, where the lowest sintering temperature of 1323 K was necessary to prepare high-density composites. At sintering temperatures over 1393 K, $CoSi_2$ was found expelled from the graphite die, decreasing the densities d of pellet samples (from ~94% for SPS-1, SPS-2, SPS-3 and SPS-4 to ~86% for SPS-6 of theoretical value).

5.2.2 Structural and thermoelectric characterizations

The phases were characterized by XRD analysis at RT with Cu-K_α radiation using an X-ray diffractometer (Ultima IV, Rigaku Co.). The microstructure was examined by field-emission scanning electron microscopy (JSM-6500F, JEOL) and a transmission electron microscope (Tecnai G2 20ST, FEI) equipped with an energy dispersive X-ray spectroscope. The specimens for TEM were prepared by mechanical polishing followed by a conventional ion-milling method.

The thermal conductivity κ was calculated from $\kappa = dCD$, where D is the thermal diffusivity and C the specific heat. Sample density d was calculated from each sample's geometry and mass. Thermal diffusivity was measured by the laser flash method using an LFA457 system (Netzsch) under Ar gas flow. Heat capacity was estimated from that of pure Si and $CoSi_2$, as obtained from the FACT53 database and literature data[25]. Carrier concentration n_H and mobility μ_H were measured using the Van der Pauw technique under a reversible magnetic field of 0.5 T with a ResiTest 8340 system (Toyo). The electrical conductivities σ and Seebeck coefficients S were measured from 300 K to 1073 K on a ZEM-3 (ULVAC-RIKO) by a four-point probe method coupled with a static direct-current method. All measurements for temperature-dependent properties were performed during heating and cooling cycles, and no hysteresis was observed. The standard error for σ was 3%, for S, it was 5%, and for κ, it was 2%, leading to a combined standard error for the power factor and ZT of ~8%. For readability of curves, error bars are not shown in figures.

5.3 Results and discussion

5.3.1 Thermal conductivity and figure of merit

We firstly investigated the sintering temperature-depended lattice thermal conductivity κ_{lat} and the dimensionless figure of merit ZT of all as-sintered samples. κ_{lat} was obtained by subtracting measured electrical conductivity κ_{el} from the total thermal conductivity κ. Here, κ_{el} was estimated using the Wiedemann-Franz law as $\kappa_{el} = LT\sigma$, where L is the Lorenz number (2.45×10^{-8} W·Ω²·K²) corresponding to a degenerate system). The sintered samples are marked as SPS-*x* (*x* = 1-6) related to the increasing sintering temperature, as denoted in Table 5.1. Figure. 5.5(a) and (b) present the temperature-dependent κ_{lat} and ZT, where a strong sintering temperature dependency can be seen in the whole temperature region. These figures show that *ZT* increases with decreasing κ_{lat}, which indicates that the improvement of *ZT* is mainly attributed to the reduction of κ_{lat}. As shown in the inset of Figure. 5.5 (a), interestingly, a U-shaped feature of κ_{lat} was found as the sintering temperature increase. Here, as representative for the sample sintered at low, middle and high temperature, SPS-1, SPS-3 and SPS-6 are chosen for further investigations.

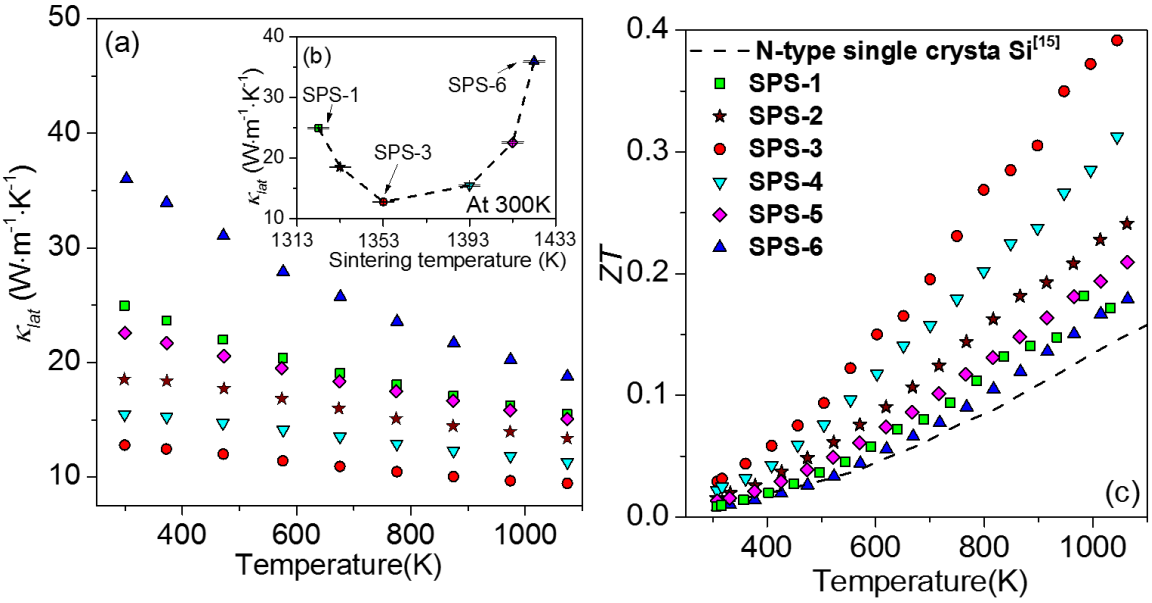

Fig. 5.5 Temperature-dependent (a) lattice thermal conductivity κ_{lat} and (b) thermoelectric figure of merit ZT of bulk $(Si_{0.99}P_{0.03})_{95}Co_5$ samples. The inset figure is the relationship between κ_{lat} and sintering temperature at 300K.

5.3.2 Phase-state and microstructure characterization

The powder XRD patterns for the melt-spun and SPS-sintered $(Si_{0.97}P_{0.03})_{95}Co_5$ samples show Si and weak $CoSi_2$ peaks in Fig. 5.6 Although the similarity of crystal structures and lattice parameters between Si and $CoSi_2$ make it difficult to clearly distinguish their XRD patterns, an enlarged view on $CoSi_2$ (111) peak shown in Figure. 5.6(b) reveals a decrease in peak intensity of $CoSi_2$ for SPS-6 sample. This can be explained by a decrease of Co composition during the high-temperature sintering, corresponding to the expelled substance which is considered to be the molten eutectic phase between Si and $CoSi_2$ (See Fig. 5.7), as well as the reduced density shown in Table 5.1. It should be mentioned that similar expelled substance was also found sticking to the surface of the SPS-3 sample. Although amount of the expelled substance is too small to apparently affect the relative peak intensity and density of SPS-3, it provide an evidence that temperature also reached its eutectic temperature during the sintering process. Note the eutectic temperature for Si-$CoSi_2$ is 1532K[26], which is higher than the sintering temperature of SPS-3(1353K). This discrepancy can attribute to two reasons: (a) temperature difference between the sample and the outer surface of the dice and (b) size effect of $CoSi_2$. Since the sintering temperature was monitored by measuring the surface temperature of the dice by a pyrometer, there would be a difference between sample temperature and the monitored temperature. As for the size effect, the size of the $CoSi_2$ precipitates in melt-spun sample is quite small. Small particles have high surface area, which results in reduction of the melting temperature. Additionally, there is no SiP peak observed within the detection limits of XRD analysis. Since the nominal content of P is beyond its maximum solubility limit in Si of about 1 at. % at 1402 K[22], the excess P possibly precipitate as SiP with a nanometer scale, based on the previous investigations in similar Si-P systems[24],[27],[28].

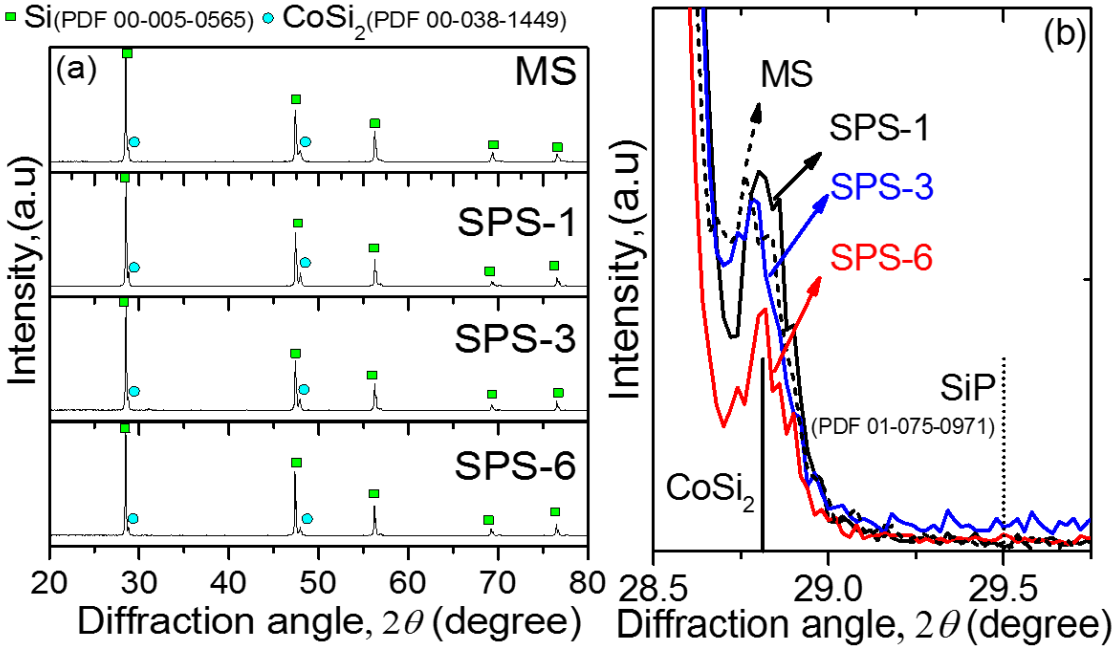

Fig. 5.6 (a) XRD patterns of $(Si_{0.99}P_{0.03})_{95}Co_5$ samples and (b) Enlarged section (in the range of 47.5° to 48.5°) of the XRD patterns.

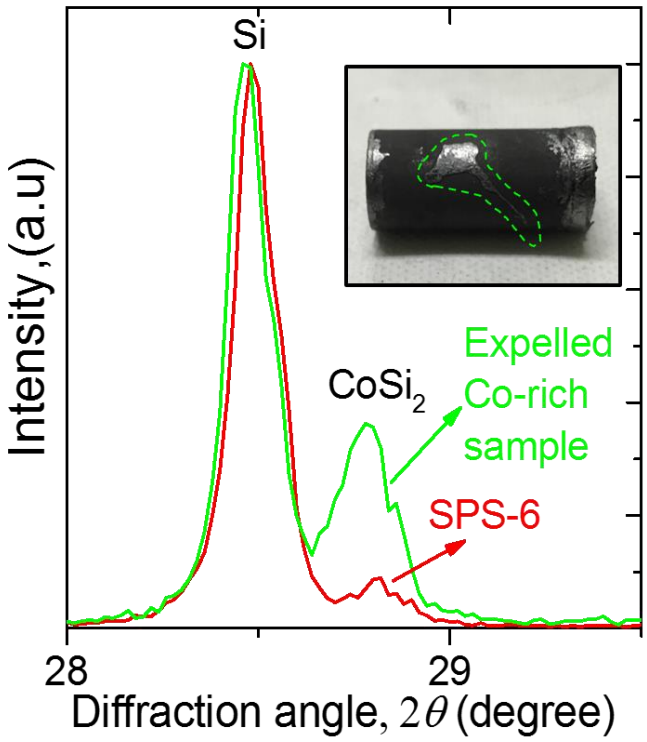

Fig. 5.7 Photograph and XRD pattern after $(Si_{0.97}P_{0.03})_{95}Co_5$ sintering at 1423 K by SPS.

Figure 5.8 shows SEM micrographs of $(Si_{0.97}P_{0.03})_{95}Co_5$ samples prepared by MS technique and SPS. All samples show two different areas due to phase separation, where the dark region correspond to the matrix phase of Si and the light region is considered to be the precipitate phase of $CoSi_2$ (See the corresponding dark area in TEM image shown in Fig. 5.10(c-d)). The precipitate sizes of both MS(<100nm) and SPS-1(~several hundred nm) in this study agree well with that of $(Si_{0.99}B_{0.01})_{95}Co_5$ processed in the same sintering condition[29]. For the as-melt-spun samples, high cooling rates clearly contribute to the large number density of precipitate by increasing the driving force for nucleation[30], whereas the high diffusion rate of Co atoms in Si leads to an unavoidable diffusion-controlled growth of $CoSi_2$ during the following SPS process for SPS-1. When compared to SPS-1, SPS-3 and 6 have the precipitates with much large size (~several μm) with concave shape, which cannot be simply explained by the normal ripening process. This result also supports the fact that the temperature reached the eutectic temperature during SPS for both SPS-3 and SPS-6. The liquid region generated by eutectic reaction around $CoSi_2$ would aggregate and result in the formation of the precipitates with concave shape. The size of the $CoSi_2$ phase in SPS-3 and SPS-6 is rather like that of an Arc-melted sample. Based our previous study[29], such coarse precipitates have negligible influence on lattice thermal conductivity and TE performance.

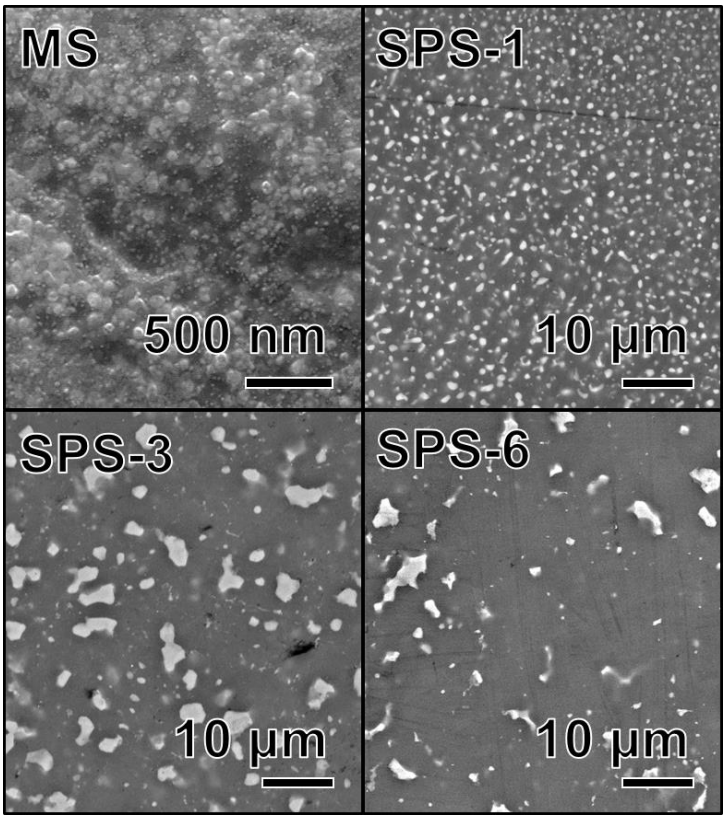

Fig. 5.8 Scanning electron micrographs of $(Si_{0.97}P_{0.03})_{95}Co_5$ samples.

In order to further explore the microstructures of $(Si_{0.97}P_{0.03})_{95}Co_5$ upon sintering temperature and their relationship with TE properties, SPS-1, SPS-3 and SPS-6 were studied by various analytical TEM techniques. Bright-field TEM images show significant different morphologies of these samples in Figs. 5.9 (a)-(c). In both SPS-1 and SPS-3, a high density of plate-like precipitates with a size of 50-100 nm were found in a matrix. As shown in Fig. 5.10(a, b) the EDS point analysis revealed that these plate-like precipitates contain higher content of P than matrix. Although it is difficult to quantitatively determine the compositions of the plate-like precipitates due to their overlap with the Si matrix, precipitates with a similar size and plate-like morphology were also found in P-supersaturated Si synthesized by arc melting followed by SPS (Arc-SPS) [24],[27], which were demonstrated as cubic SiP. Compared with the Arc-SPS sample [24], it seems that neither MS-SPS process nor Co-addition have notable effect on the self-assembled precipitation of SiP, as evident from the comparable average size and number density of ~24 nm and ~2.8×10^{10} cm^{-2}, respectively(the size and number density are evaluated from several Bright-field TEM images taken at different areas). It is also noteworthy that dislocation loops are found around the SiP precipitates with diameter <100 nm in SPS-1 and SPS-3, as shown in the insets of Fig. 5.9(a, b). These dislocation loops were not observed in the Arc-SPS sample[24]. The presence of dislocation loops, which can attribute to the precipitate-dislocation interaction during Orowan bypass process, reveals that dislocation motion is active for the samples SPS-1 and 3.

Other than these dislocation loop decorating the SiP precipitates, the density of residual dislocations in Si matrix remains at a low level in SPS-1. However, the density of residual dislocations in grains dramatically increase in SPS-3. Fig. 5.9(b) shows a typical region mixed with dislocations and SiP precipitates. These dislocations exhibit

the wavy, unstable orientations of short segments of partial dislocations, revealing a strong pinning behavior at some of the defect sites. Since the dislocation generally remains straight after the Orowan bypass process[31], the bowing feature of dislocations may be derived from trapping of strong pinning centers like P solute atoms[32],[33].

Although the origin of the generation of the high-density dislocations remains a matter of research, several possible mechanisms can be mentioned. Although residual stresses might cause the formation of dislocations, this would not be the case in this study since residual stresses are generally produced by mismatch of thermal expansion during a cooling process between matrix and precipitate, this mismatch is expected to be quite small between Si and $CoSi_2$ [34]. In our case, Co atoms left in Si matrix might attribute to the formation of dense dislocations. As mentioned above, temperature reached eutectic temperature during SPS for SPS-3. By the eutectic reaction, liquid Si-Co phase is once generated from both Si and $CoSi_2$, and it solidified to form Si and $CoSi_2$ during cooling. When the liquid phase solidified, some Co atoms may be incorporated into Si above its solubility limit. These Co atoms would generate strong local strains in Si, which might act as an origin of the dislocations. Or, the Co atoms might react with Si to form $CoSi_2$, which leads to an excess of Si-vacancies[15],[16]. Such vacancies would generate dislocations by a vacancy-assist formation process of dislocation[17]. It is should be pointed out that owing to the high-density Si-$CoSi_2$ interfaces introduced by MS technique, a higher vacancy supersaturation can be expected[15], which may also contribute to the enhanced dislocation density.

TEM image of the high-temperature sintered SPS-6 is shown in Fig. 5.9(c). In contrast to SPS-1 and 3, all of the dislocations are eliminated except very small amount of residual dislocations located near the grain boundary (see the enlarged view). Note that the SiP phase and the surrounding Orowan loops disappeared due to phosphorus evaporation at this sintering temperature, the immobilized dislocation seems released from residual SiP in SPS-6.

To clarify the possible mechanisms of pinning effect on dislocation, the microstructure of dislocation in SPS-3 were analyzed in detail. As shown in Fig. 5.11(a) numerous nanodots with a size below 10 nm are found to distribute along the dislocations. From the diffraction pattern shown in the insert of Fig 5.11(b), it can be concluded that these nanodots have similar structure and lattice parameter with Si matrix, resulting in the corresponding continuity of crystallographic planes and orientations across the interface to matrix. High-resolution TEM images of a typical nanodot shows a interplanar spacing of about 3.095 Å, which is close to that of the (111) atomic plane of $CoSi_2$ (3.096 Å, see JCPDS card 38-1149), indicating presence of $CoSi_2$ rather than cubic SiP (d_{111} = 3.026 Å, see JCPDS card 27-0608) or orthorhombic SiP. Different from the coarse $CoSi_2$ phase, $CoSi_2$ nanodots are believed to nucleate and grow during the sintering process, because distribute only around the residual dislocations. Co atoms tend to migrate to the dislocations at the sintering temperature due to the driving force arising from the interaction between the individual impurity atoms and structural defect, which consequently reduce the overall strain energy[35]. This migration of Co atoms stabilizes the dislocations and may further enhance the pining effect on dislocation by doped phosphorus, resulting in both high density and thermal stability of dislocations. Then, during subsequent cooling processes, the Co atoms at dislocations are kicked out due to the reduction of the solubility, which results in the formation of precipitates around the dislocations. Similar accumulation behavior of other type of silicide precipitates was also observed along the dislocations at a high annealing temperature (> 900 ^oC)[36],[37],[38].

To investigate the detailed microstructure features about the dislocation, a serial continuous HRTEM images are taken (see Fig. 5.12-5.14) and a representative area is shown in Fig.5.11(c). Interestingly, high-density stacking

faults are found along the [111] orientation. These nanoscale stacking faults are less than 3 layers of lattice in width and 25 nm in length. The corresponding fast Fourier transform (FFT) image show streaking (highlighted by red arrows in Fig. 5.11(c)) that connect the (111) and (200) planes. This evidence further confirms the existence of stacking fault, which is supposed to scatter medium-to-high frequency phonons[39],[40]. As for dislocation cores and corresponding strain fields, inverse fast Fourier transform (IFFT) images combined with geometric phase analysis (GPA) were introduced to analyze the HRTEM image of Fig. 5.11(c) (For the image series, see Fig. 5.12- 5.14). Fig. 5.11 (d-f) show the processed IFFT images from reflections ((111), (11-1) and (200)), respectively. As marked by red symbols in Fig. 11(d-f), it appears that a large number of dislocation cores pervasively exist around the dislocation in the all three planes. The areal dislocation core density was found over 2.0×10^{12} cm^{-2} in the region shown in Fig. 5.11 (c), while the average core density along the dislocations is estimated about 0.7×10^{12} cm^{-2} (see Fig. 5.12). Figs. 5.11 (g-i) show the strain fields map of ε_{xx}, ε_{yy} and shear strain ε_{xy} following the x-axis parallel to [111] orientation and the y-axis in the [200] orientation. The color scale corresponds to the strain from -30% to +30% in reference to the average strain of a non-defect area. Convergence regions of strains are found existing around the dislocation core, which randomly distributed in all orientation, and along stacking faults in (111) plane. In conclusion of this part, complex hierarchical microstructures composed the high-density nanodots, stacking faults and dislocation cores as well as the associated strain field were found along the dislocation, which are expected to be effective scatter source for medium-to-high frequency phonons.

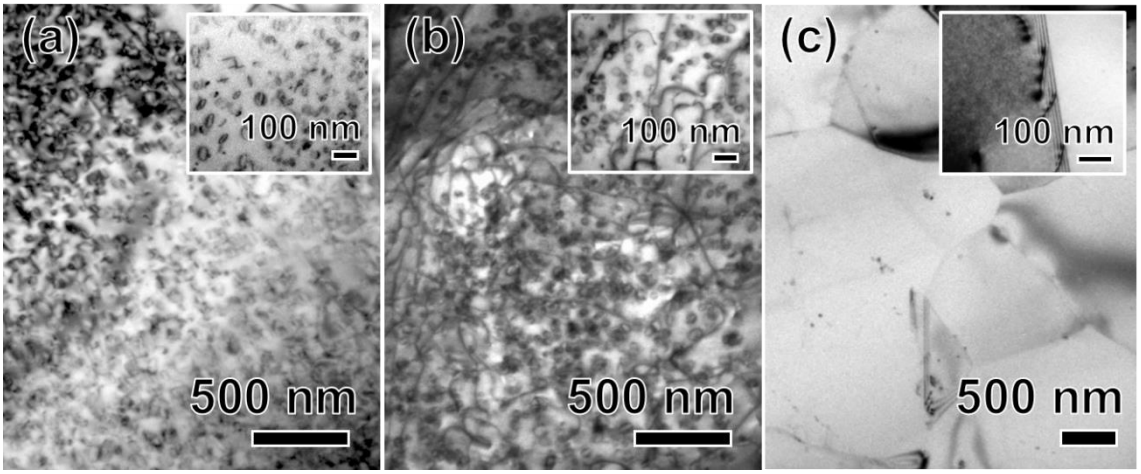

Figure 5.9 Bright-field TEM image of (a) SPS-1, (b) SPS-3 and (c) SPS-6.

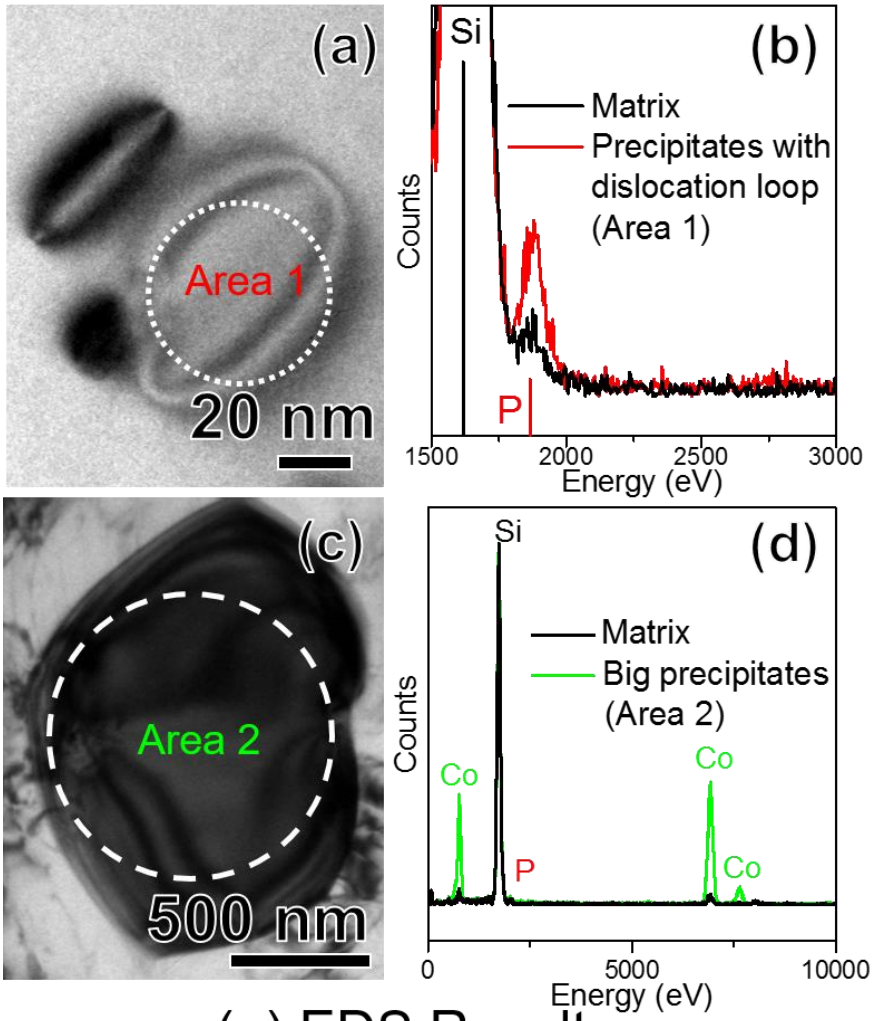

(e) EDS Results

Area	At. % Si	At. % P	At. % Co
Matrix	99.1±0.7	0.9±0.1	-
Area 1	96.9±0.9	3.1±0.2	-
Area 2	71.4±0.3	0.4±0.1	28.2±0.3

Fig. 5.10 (a, c) Bright-field TEM image of SPS-3 and (b, d) energy-dispersive spectroscopy (EDS) spectrum of selected areas in (a, c), respectively. The EDS results are given in (e).

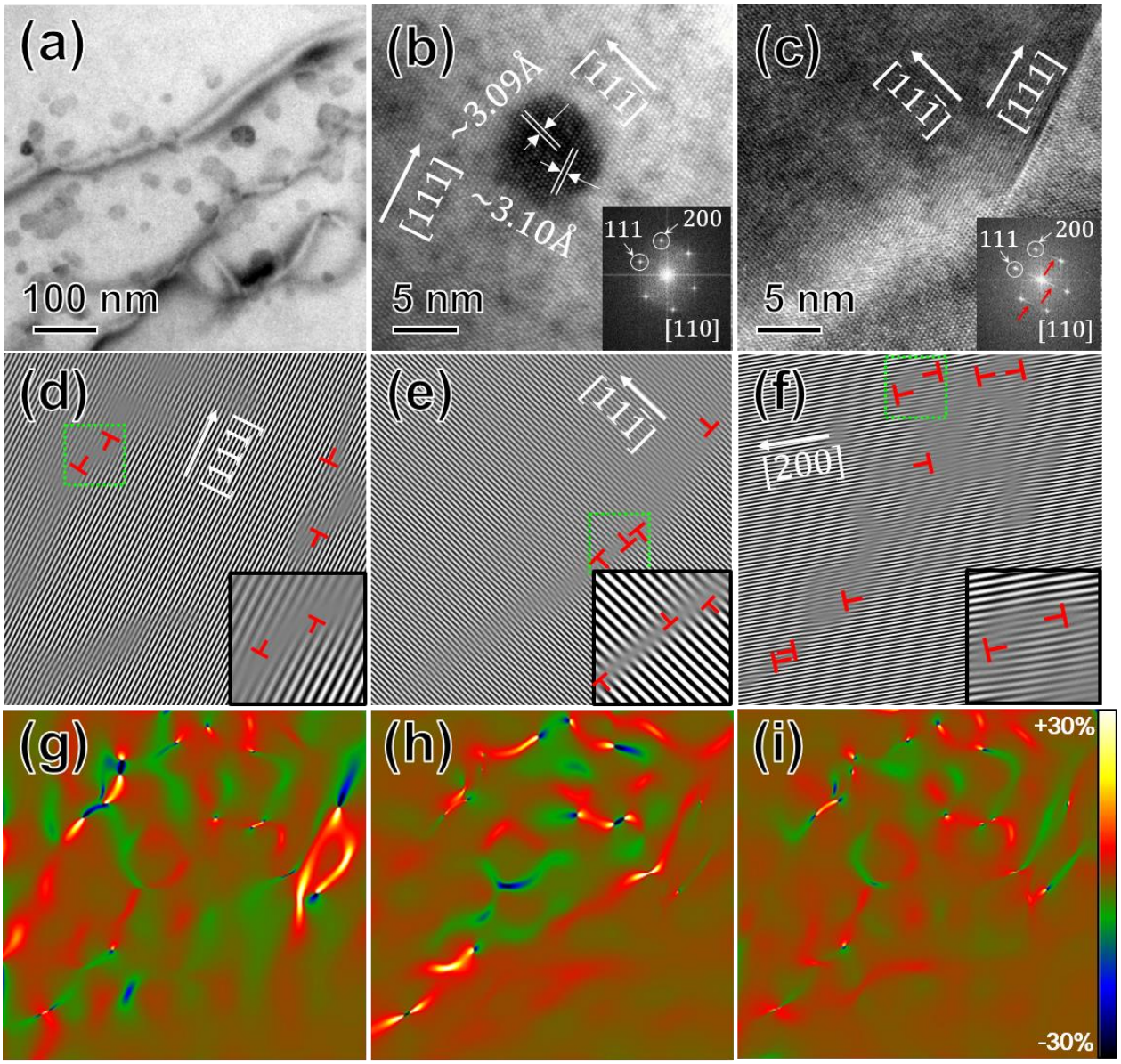

Fig. 5.11 (a) Bright-field TEM image of a typical dislocation area, HRTEM images with inserted the fast Fourier transform (FFT) pattern for (b) the nanodot and (c) the dislocation; (d-f) inverse FFT (IFFT) images of (111), (−111) and (200) atomic planes of (c) with enlarged views of dot-boxed regions; (g-i) Strain mapping of different strain terms, (g) along xx direction, (h) yy direction, and (i) xy direction between (111) and (200) of (c) in SPS-3.

Area	d_{dis} (10^{12} cm^{-2})
1	1.1
2	0.9
3	1.0
4	0.1
5	1.1
6	2.0
7	0.0
8	0.5
9	0.4
10	0.1
11	0.0
$\overline{d_{dis}}$	0.7

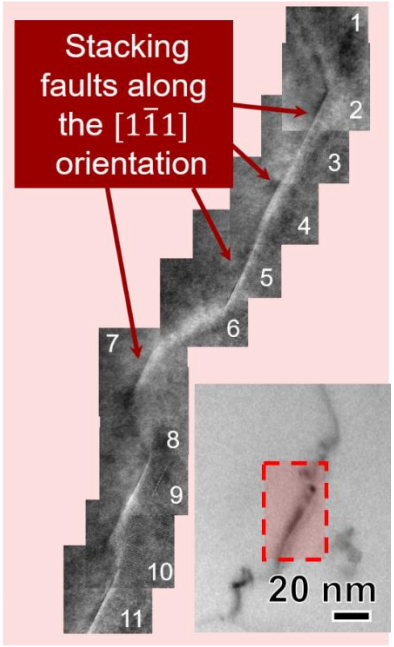

Fig. 5.12 Series of HRTEM images of short segments of dislocation. Region 6 is shown in Fig. 5.11(c), while the average core density along the dislocations was estimated to be ~0.7 × 10^{12} cm^{-2} in this area.

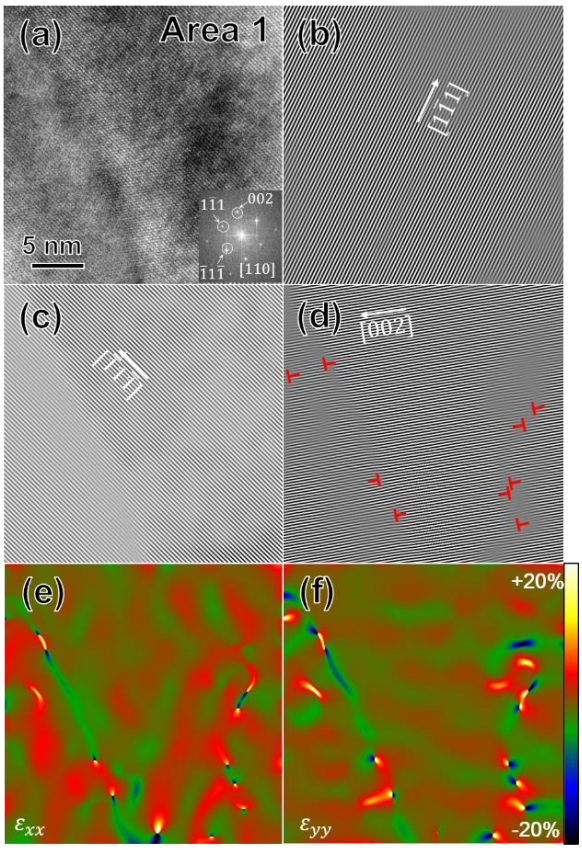

Fig. 5.13 (a) Bright-field TEM image of area 1 in Fig. 5.12. (b–d) Inverse FFT (IFFT) images of (1-11), (-11-1), and (002) atomic planes of (a). (e–f) Strain mapping of different strain terms along the (e) xx direction, (f) yy direction, and (1-11) and (002) of (a).

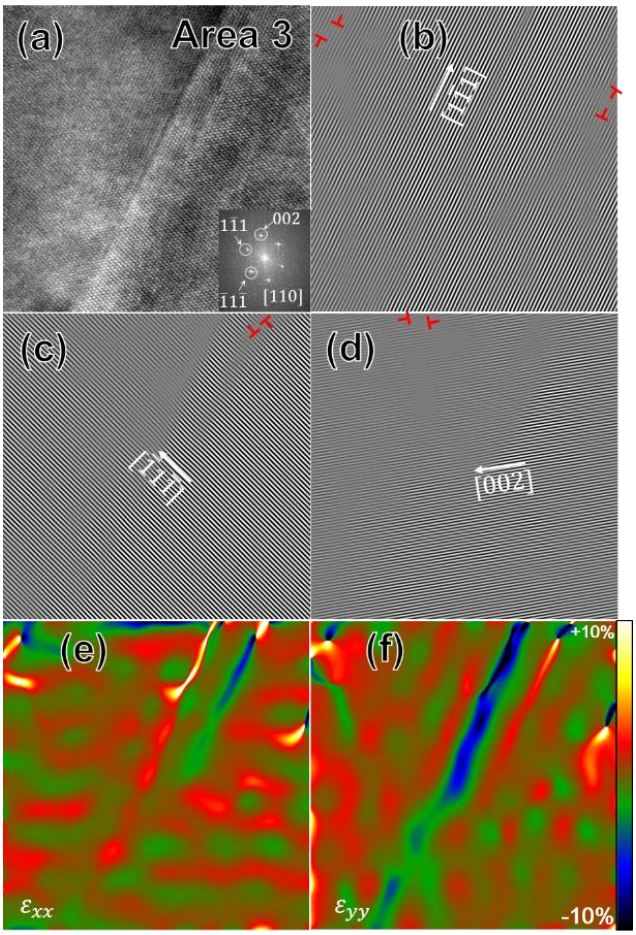

Fig. 5.14 (a) Bright-field TEM image of area 1 in Fig. 5.12. (b–d) Inverse FFT (IFFT) images of (1-11), (-11-1), and (002) atomic planes of (a). (e–f) Strain mapping of different strain terms along the (e) xx direction, (f) yy direction, and (-11-1) and (1-11) of (a).

5.3.3 Modeling of lattice thermal conductivity

To understand the effect of the hierarchical microstructures on phonon scattering, we compared our experimental data with calculated values based on the Boltzmann transport equation with frequency dependent phonon mean free path. In the model, lattice thermal conductivity is expressed as

$$\kappa = \sum_{\lambda} \frac{1}{3} \int C \cdot v \cdot \Lambda_{eff} \cdot d\omega, \tag{5.3}$$

where ω is the phonon frequency, C is the lattice heat capacity, v is the phonon group velocity, Λ_{eff} is the effective phonon mean-free path and λ is the polarization of the phonons, respectively. The details of the model has been described elsewhere[41]. Here, assuming all the phonon scattering processes were independent, Λ_{eff}^{-1} be written as a sum of the inverse of mean-free path of several scattering probabilities based on Matthiessen's rule. Here we considered (a) umklapp scattering Λ_U^{-1}, (b) alloy disorder scattering Λ_{AD}^{-1}, (c) grain boundary scattering Λ_{GB}^{-1}, (d) phonon-electron scattering Λ_{PE}^{-1}, (e) nanoparticle scattering Λ_{NP}^{-1}, (f) Λ_{DC}^{-1} dislocation core and Λ_{DS}^{-1} dislocation-induced strain field. These scattering effects are summarized as

$$\Lambda_{eff}^{-1} = \Lambda_U^{-1} + \Lambda_{AD}^{-1} + \Lambda_{GB}^{-1} + \Lambda_{PE}^{-1} + \Lambda_{NP}^{-1} + \Lambda_{DC}^{-1} + \Lambda_{DS}^{-1}. \tag{5.4}$$

Based on the parameter from previous study and TEM analysis, lattice thermal conductivity of SPS-1 and SPS-6 are estimated by this model (see the Table 5.1 and 5.2 for more details) as shown in Fig. 5.15. Line 1 agree well with the thermal conductivity of single crystal Si, indicating that umklapp scattering is dominant in single crystal Si. While line 2 is slightly lower than the thermal conductivity of single crystal Si, much higher than that of SPS-6, suggesting that grain boundary scattering effect is small due to the large grain size of Si matrix. In contrast, line 3 is in good agreement with SPS-6, which shows that heavily doped P play a vital role in the lattice thermal conductivity reduction for SPS-6. This is reasonable because the thermal conductivity of SPS-6 is quite close to that of polycrystalline Si having the same carrier concentration with SPS-6. Enhanced electron-phonon interaction, accompanied with a minor contribution of mass disorder and lattice strain, has been demonstrated theoretically[42] and experimentally[28] as the main reason for significant decreased lattice thermal conductivity in highly-doped Si. This result means that the course $CoSi_2$ particles have negligible effect on the thermal conductivity owing to the low volume fraction, high thermal conductivity of $CoSi_2$[43] close to that of Si, and relatively large size of $CoSi_2$ particles in SPS-6.

Compared with the SPS-6, the lattice thermal conductivity of SPS-1 is lower than that of SPS-6 by 30% (36.0 $W \cdot m^{-1}K^{-1}$ for SPS-6 and 25.0 $W \cdot m^{-1}K^{-1}$ for SPS-1) at 300K, and agree well with that of poly crystalline Si with SiP nanoprecipitates[24], suggesting that this reduction in lattice thermal conductivity would be ascribed to the enhanced phonon scattering due to precipitation of nanoscale SiP. In order to evaluate the effect of SiP, we introduce a simplified model given by a Mathiessen-type interpolation between the short- and long-wavelength scattering regimes[44],[45] to estimate the additional phonon scattering from SiP. The calculated value, plotted as line 4, is in fairly good agreement with the measured value of SPS-1, supporting the prediction that SiP nanoprecipitates are the main reason for the reduction of lattice thermal conductivity for SPS-1. As for SPS-3, an additional 50% reduction (13.5 $W \cdot m^{-1}K^{-1}$ for SPS-3 at 300K) in lattice thermal conductivity was achieved compared with SPS-1, which is also lower than the theoretical prediction consideration with dislocation core and corresponding strain field (line 5). Stacking faults and $CoSi_2$ nanodots originated from the migration and segregation of Co atoms at elevated temperature are considered to

be responsible for this discrepancy, suggesting the considerable degree of complex microstructure for SPS-3.

Table 5.1 Equations for mean free paths (Λ) associated with different types of scattering processes

Phonon scattering processes	Phonon mean-free path
Umklapp scattering	$\Lambda_U^{-1} = \frac{B_1 \omega^2 T e^{-\frac{B_2}{T}}}{v}$
Alloy disorder scattering	$\Lambda_{PD}^{-1} = \frac{\bar{V}\omega^4}{4\pi v^3} \sum_i f_i \left\{ \left(\frac{M - M_i}{M} \right) + \varepsilon \left(\frac{\delta - \delta_i}{\delta} \right)^2 \right\}$
Phonon-electron scattering	$\Lambda_{PE}^{-1} = \frac{E_F^2 m^{*2} \omega}{2\pi\hbar^3}$
Grain boundary scattering	$\Lambda_{GB}^{-1} = D_A$
Nanoparticle scattering	$\Lambda_{NP}^{-1} = (\Gamma_R^{-1} + \Gamma_G^{-1})^{-1} \rho$ $\Gamma_R = \pi R^2 \frac{4}{9} (\frac{d-d_i}{d})^2 (\omega R/v)^4$ $\Gamma_G = 2\pi R^2$
Dislocation-induced scattering	See chapter 5.1.1

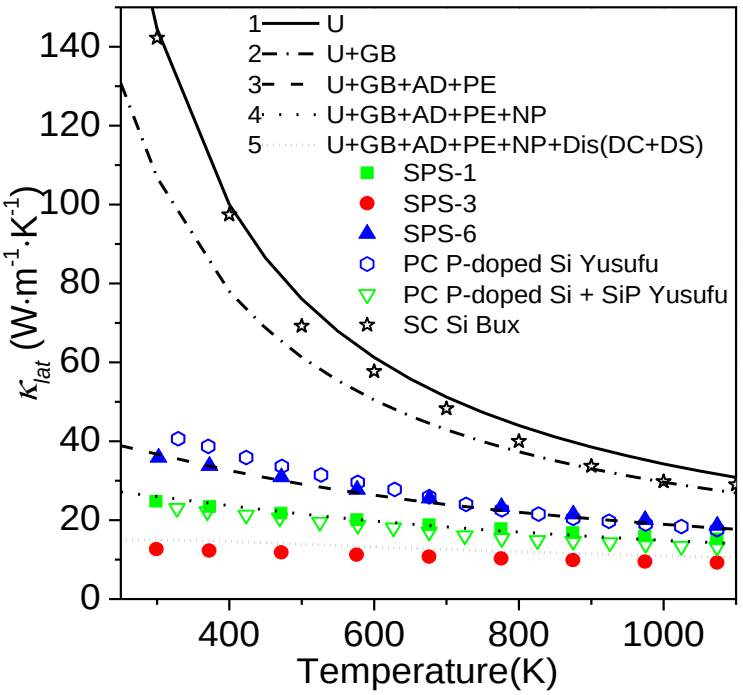

Fig. 5.15 Comparison of the experimental data and the calculated lattice thermal conductivity based on TEM observations in the whole temperature region. The reference data are taken from Yusufu et al.[24] and Bux et al.[46]

Table 5.2 Parameters for the Boltzmann transport equation with frequency-dependent phonon mean free path

Property		Parameters	Value	Note
Sound velocity		v^L v^T	8340 (m/s) 5840 (m/s)	Ref.[47]
		v	6084 (m/s)	Ref.[48]
Umklapp scattering parameters		B_1 B_2	1.47 (10^{-19}s/K) 112 (K)	Ref.[48]
Fractional concentration of the impurity (P)		f_i	0.006	Estimated from $n_H \sim 3 \times 10^{20}$ cm^{-3} under the assumption that all the dopant atoms are ionized at 300 K
Volume of a primitive cell ($Si_{0.994}P_{0.006}$)		$\bar{V}$	19.98 (10^{-30}m^3)	Estimated from the lattice parameter 4.95 Å of P-doped Si from [49]
Averaged atomic mass ($Si_{0.994}P_{0.006}$)		M	28.11 (g/mol)	
Atomic mass of impurity (P)		M_i	30.97 (g/mol)	
Averaged atomic radius ($Si_{0.994}P_{0.006}$)		δ	2.71 (Å)	
Atomic radius of impurity (P)		δ	2.48 (Å)	
Alloy disorder scattering parameter		ε	6	Ref.[50]
Electron-phonon deformation potential		E_F	3 (eV)	Ref.[51]
Density-of-stages effective mass		m^*	1.08·m_e (Kg)	Ref.[52]
Grain size	SPS-1	D_A	3.5 (10^{-6}m)	Estimated from TEM figures
	SPS-6		3.5 (10^{-6}m)	
Density	$Si_{0.994}P_{0.006}$	d	2.33 (10^3kg/m^3)	Estimated from [49]
	SiP	d_i	2.40 (10^3kg/m^3)	Ref.[53]
Radius of particles (SiP)		R_A	12.2 (10^{-9}m)	Estimated from TEM figures
Number density of particles(SiP)		ρ_A	2.8 (10^{14}m^{-2})	Estimated from TEM figures
Number density of dislocation cores		N_d	0.7 (10^{16}m^{-2})	Estimated from IFFT figures
Magnitude of Burgers vector of dislocations		B_d	3.84 (Å)	Ref.[54]
Grüneisen parameter		γ	0.9	Ref.[48]
Poisson ratio		r	0.28	Ref.[5]

5.3.4 Electrical Transport properties

In this section, the electronic transport properties of the resulting samples were investigated. Temperature dependent Seebeck coefficient S and electrical conductivity σ are shown in Figs. 5.17(a, b). In the measured temperature range, electrical conductivity is decreasing while Seebeck coefficient is increasing as temperature rises, showing the behavior of a heavily-doped semiconductor. This results are also confirmed by the Hall Effect measurements, where all the samples exhibit high carrier concentrations of about 3×10^{20} cm^{-3}. Although the carrier concentration varied from sample to sample, the variation is quite small, possibly because of the solubility limit of P in Si. The similar values of electron concentration are reported for excess P doped Si synthesized by furnace SPS[24],[28] and hot-press[55].

As shown in Table 5.3, carrier mobility of all MS-SPSed samples are lower than that of the Si/SiP composite prepared by Arc-SPS (43 $cm^2 \cdot V^{-1} \cdot s^{-1}$)[24] and single-crystal Si (47 $cm^2 \cdot V^{-1} \cdot s^{-1}$)[56] with a similar electron concentration. The degeneration of carrier mobility can be explained by the existence of higher concentration of grain boundary/lattice defects, which consequently leads to lower electrical conductivities and lower power factor in MS-SPS samples compared to the Arc-SPS samples (see Figs. 5.17(a, c)).

The relationship between Seebeck coefficient and carrier concentration can be expressed as

$$S = \frac{2k_B T}{3q\hbar^2}\left(\frac{\pi}{3n}\right)^{\frac{2}{3}} m^*(1+\lambda), \tag{5.5}$$

where k_B, q, $\hbar$, m^*, λ are the Boltzmann constant, elementary charge, Planck constant, electron effective mass and scattering parameter, respectively. Here, parameters such as $m^* = 1.08m_0$ and $\lambda = 0.65$ were used for calculation, which are taken from literature[24]. The resulting values at 300 K are plotted as the solid line shown in Fig 5.17(d). The theoretical curve provides a close fit to experimental data of P-doped Si including single crystal Si[57],[48], nanostructured Si[46],[28] and Si composites[24]. This suggests that there is no difference in the band structure and carrier scattering mechanism between our samples and P-doped bulk Si materials, which means that whose microstructures of our samples have a minor effect on the band structure and carrier scattering mechanism.

The experimental data measured during both heating and cooling thermal cycles is also shown in the Fig. 5.16. As can been seen, resistivity, Seebeck coefficient and total thermal conductivity obtained during heating and cooling cycles do not change significantly.

Table 5.3 Sintering temperature, density d, relative density, carrier concentration n_H, carrier mobility μ_H of the bulk samples at 300 K.

Sample name	Sintering temperature(K)	d (g/cm^3)	n_H (10^{20}/cm^3)	μ_H (cm^{2}V^{-1} s^{-1})
SPS-1	1323	2.52	3.6	33
SPS-2	1333	2.49	3.0	34
SPS-3	1353	2.48	2.5	39
SPS-4	1393	2.50	3.4	34
SPS-5	1413	2.43	2.8	31
SPS-6	1423	2.30	3.0	32
SC P-doped Si[56]	1353	-	3.0	56*
PC P-doped Si + SiP[24]	-	2.30	3.8	43

*taken from the fitting results of experimental data

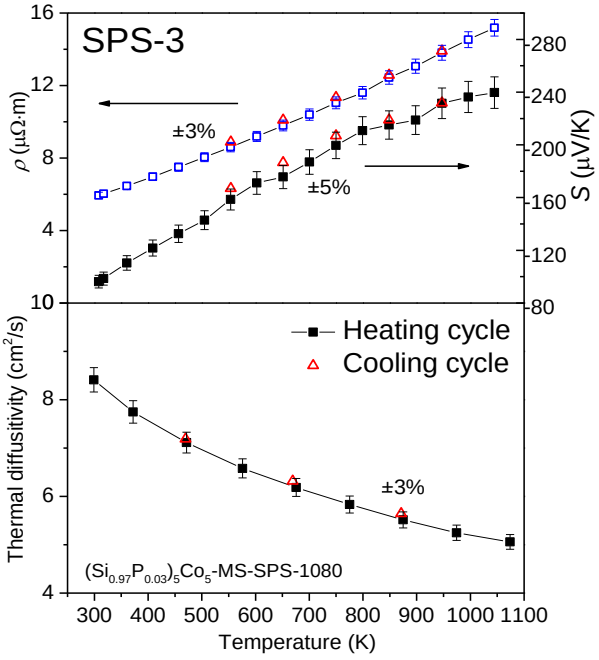

Fig. 5.16 The experimental data of $Si_{92}B_8$-MS-SPS measured during both heating and cooling thermal cycles.

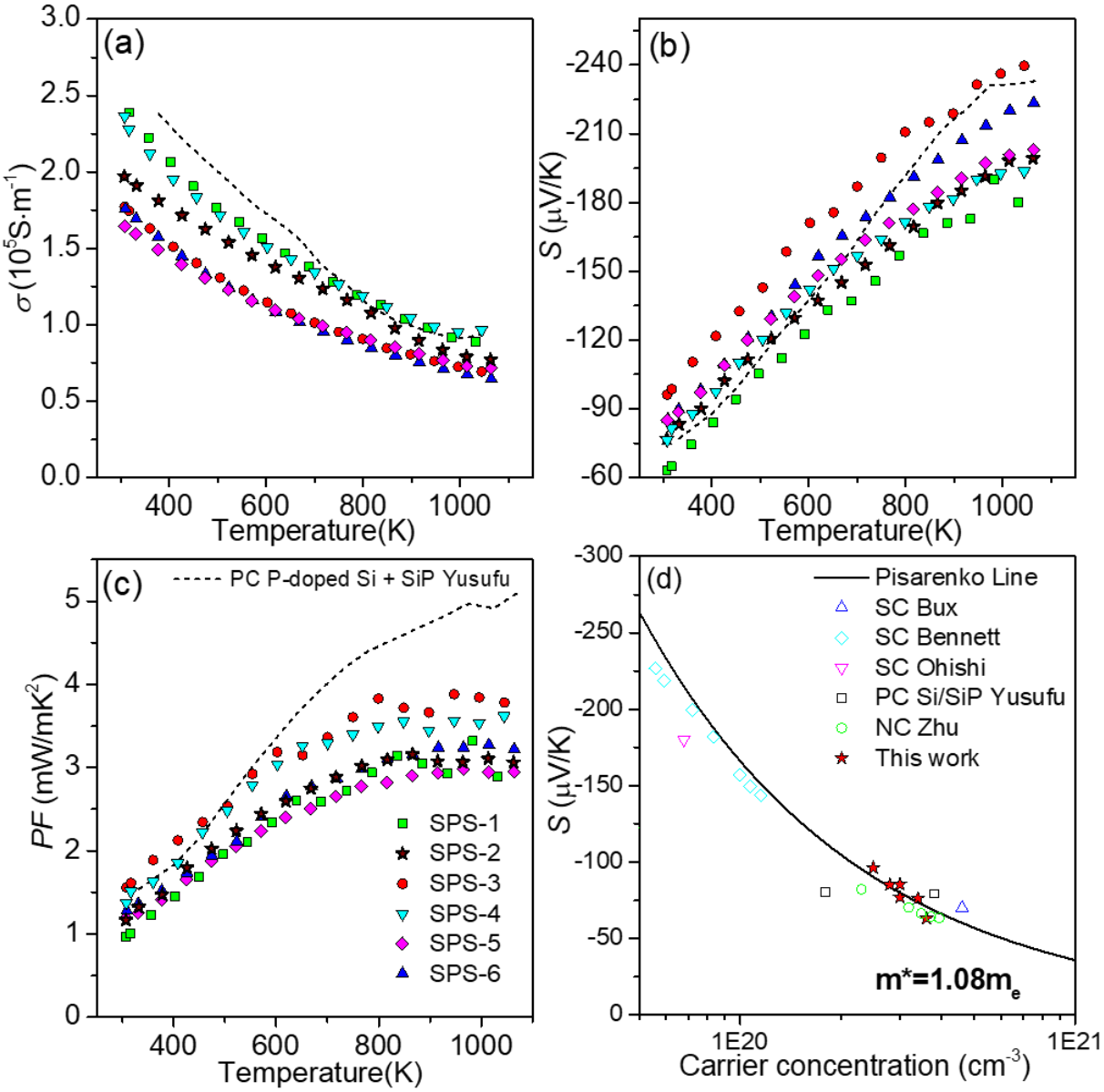

Fig. 5.17 (a-c) Temperature dependent electrical transport properties of all the bulk samples: (a) electrical conductivities σ, (b) Seebeck coefficient S and (c) power factor PF. (d) Relationships between S and n_H at 300K. The literature data are taken from reference[24][28][46][48][57].

5.4 Conclusions

We presented a novel self-assembly method to introduce complex defects throughout the grains of Si-based TE materials. High-density dislocations were formed by high-temperature sintering of excess P-doped Si/$CoSi_2$ composites. Detailed TEM investigation showed that complex nanostructures such as high-density nanodots, stacking faults, dislocation cores, and associated strain fields were formed along the dislocations. The lattice thermal conductivity was reduced by these nanostructures to 13.5 $W \cdot m^{-1}K^{-1}$, which was 1/3 that of heavily P-doped Si with the same carrier concentration. The reduction in thermal conductivity resulted in a higher figure of merit *ZT* of 0.39 at 1045 K. This work provides evidence for the efficacy of high-density dislocations as additional constituents for typical hierarchical architecture, filling the void of a full-frequency spectrum for phonon scattering. We believe that further enhancement in TE performance is possible by subsequent low-temperature annealing, aiming at the multiplication of dislocations with a thermally stable pinning source.

5.5 Reference

[1] K. Biswas, J. He, I. D. Blum, C.-I. Wu, T. P. Hogan, D. N. Seidman, V. P. Dravid, M. G. Kanatzidis, *Nature* **2012**, *489*, 414.

[2] L. Zhao, V. Dravid, M. Kanatzidis, *Energy Environ. Sci.* **2014**, *7*, 251.

[3] J. Hirth, J. Loth., *Theory of Dislocations*, John Willey & Sons, **1982**.

[4] S. Takeuchi, A. S. Argon, *J. Mater. Sci.* **1976**, *11*, 1542.

[5] T. Wang, J. Carrete, A. Van Roekeghem, N. Mingo, G. K. H. Madsen, *Phys. Rev. B* **2017**, *95*, 1.

[6] P. Klemens, *Proc. Phys. Soc. Sect. A* **1955**, *68*, 1113.

[7] Z. Chen, B. Ge, W. Li, S. Lin, J. Shen, Y. Chang, R. Hanus, G. J. Snyder, Y. Pei, *Nat. Commun.* **2017**, *8*, 13828.

[8] S. Kim, K. Lee, H. Mun, H. Kim, S. Hwang, J. Roh, D. Yang, W. Shin, X. Li, Y. Lee, J. Snyder, S. Kim, *Science (80-.).* **2015**, *348*, 109.

[9] J. Xin, H. Wu, X. Liu, T. Zhu, G. Yu, X. Zhao, *Nano Energy* **2017**, *34*, 428.

[10] J. He, M. G. Kanatzidis, V. P. Dravid, *Mater. Today* **2013**, *16*, 166.

[11] H. Kim, S. Kang, Y. Tang, R. Hanus, G. Jeffrey Snyder, *Mater. Horizons* **2016**, *3*, 234.

[12] S. Lo, J. He, K. Biswas, M. Kanatzidis, V. Dravid, *Adv. Funct. Mater.* **2012**, *22*, 5175.

[13] J. He, S. N. Girard, M. G. Kanatzidis, V. P. Dravid, *Adv. Funct. Mater.* **2010**, *20*, 764.

[14] H. Zhao, B. Cao, S. Li, N. Liu, J. Shen, S. Li, J. Jian, L. Gu, Y. Pei, G. J. Snyder, Z. Ren, X. Chen, *Adv. Energy Mater.* **2017**, *1700446*, 1.

[15] S. Herner, H. Gossmann, R. Tung, *Appl. Phys. Lett.* **1998**, *72*, 2289.

[16] R. Back, **n.d.**, pp. 261–266.

[17] F. Frank, J. Nicholas, *London, Edinburgh, Dublin Philos. Mag. J. Sci.* **1953**, *44*, 1213.

[18] F. Frank, W. Read, *Phys. Rev.* **1950**, *79*, 722.

[19] J. Koehler, *Phys. Rev.* **1952**, *86*, 52.

[20] J. Bardeen, C. Herring, *Imperfections in Nearly Perfect Crystals*, **1952**.

[21] K. Sumino, M. Imai, *Philos. Mag. A Phys. Condens. Matter, Struct. Defects Mech. Prop.* **1983**, *47*, 37.

[22] J. Safarian, M. Tangstad, *J. Mater. Res.* **2011**, *26*, 1494.

[23] A. Mostafa, M. Medraj, *Materials (Basel).* **2017**, *10*, 676.

[24] A. Yusufu, K. Kurosaki, Y. Miyazaki, M. Ishimaru, A. Kosuga, Y. Ohishi, H. Muta, S. Yamanaka, *Nanoscale* **2014**, *6*, 13921.

[25] M. Niranjan, *Comput. Mater. Sci.* **2014**, *95*, 517.

[26] S. Choi, *Calphad* **1992**, *16*, 151.

[27] A. Armigliato, P. Werner, *Ultramicroscopy* **1984**, *15*, 61.

[28] T. Zhu, G. Yu, J. Xu, H. Wu, C. Fu, X. Liu, J. He, X. Zhao, *Adv. Electron. Mater.* **2016**, 1600171.

[29] J. Xie, Y. Ohishi, S. Ichikawa, H. Muta, K. Kurosaki, S. Yamanaka, *J. Appl. Phys.* **2017**, *121*, 205107.

[30] N. Hein*ZT*. Ikeda, Y. Pei, J. Snyder, *Adv. Funct. Mater.* **2014**, *24*, 2135.

[31] Y. Xiang, D. Srolovitz, L. Cheng, E. Weinan, *Acta Mater.* **2004**, *52*, 1745.

[32] M. Imai, K. Sumino, *Philos. Mag. A* **1983**, *47*, 599.

[33] P. Taylor, M. Heggie, R. Jones, A. Umerski, **2006**, 37.

[34] G. Bai, M. Nicolet, T. Vreeland, *J. Appl. Phys.* **1991**, *69*, 6451.

[35] M. Seibt, R. Khalil, V. Kveder, W. Schröter, *Appl. Phys. A Mater. Sci. Process.* **2009**, *96*, 235.

[36] K. Sumino, *Phys. Status Solidi* **1999**, *171*, 111.

[37] I. Yonenaga, K. Sumino, *J. Appl. Phys.* **1996**, *80*, 734.

[38] J. Solberg, E. Nes, *J. Mater. Sci.* **1978**, *13*, 2233.

[39] B. K. Singh, V. J. Menon, K. C. Sood, *Phys. Rev. B - Condens. Matter Mater. Phys.* **2006**, *74*, 1.

[40] Z. Liu, Y. Wang, J. Mao, H. Geng, J. Shuai, Y. Wang, R. He, W. Cai, J. Sui, Z. Ren, *Adv. Energy Mater.* **2016**, *6*, 1.

[41] Z. Wang, J. E. Alaniz, W. Jang, J. E. Garay, C. Dames, *Nano Lett.* **2011**, *11*, 2206.

[42] B. Liao, B. Qiu, J. Zhou, S. Huberman, K. Esfarjani, G. Chen, *Phys. Rev. Lett.* **2015**, *114*, 1.

[43] B. M. Ditchek, *J. Cryst. Growth* **1984**, *69*, 207.

[44] W. Kim, S. Singer, A. Majumdar, J. Zide, D. Klenov, A. Gossard, S. Stemmer, *Nano Lett.* **2008**, *8*, 2097.

[45] N. Mingo, D. Hauser, N. Kobayashi, M. Plissonnier, A. Shakouri, *Nano Lett.* **2009**, *9*, 711.

[46] S. Bux, R. Blair, P. Gogna, H. Lee, G. Chen, M. Dresselhaus, R. Kaner, J. Fleurial, *Adv. Funct. Mater.* **2009**, *19*, 2445.

[47] T. Morelli, P. Heremans, A. Slack, *Phys. Rev. B* **2002**, *66*, 195304.

[48] Y. Ohishi, J. Xie, Y. Miyazaki, Y. Aikebaier, H. Muta, K. Kurosaki, S. Yamanaka, N. Uchida, T. Tada, *Jpn. J. Appl. Phys.* **2015**, *54*, 71301.

[49] G. Celotti, D. Nobili, P. Ostoja, *J. Mater. Sci.* **1974**, *9*, 821.

[50] J. Xie, Y. Ohishi, Y. Miyazaki, A. Yusufu, H. Muta, K. Kurosaki, S. Yamanaka, *J. Appl. Phys.* **2015**, *118*, 65103.

[51] M. Lundstrom, *Fundamentals of Carrier Transport, 2nd Ed.*, Cambridge University Press, Cambridge, United Kingdom, **2000**.

[52] H. Lee, D. Vashaee, D. Z. Wang, M. S. Dresselhaus, Z. F. Ren, G. Chen, *J. Appl. Phys.* **2010**, *107*, 1.

[53] T. Wadsten, *Chem. Scr.* **1975**, *8*, 63.

[54] R. Hull, *Properties of Crystalline Sillicon*, INSPEC(the Institution Of Electrical Engineers), **1999**.

[55] Q. Luan, Z. Ni, S. Koura, T. Zhu, D. Yang, X. Pi, *AIP Adv.* **2014**, *4*, 127108.

[56] G. Masetti, M. Severi, S. Solmi, *IEEE Trans. Electron Devices* **1983**, *30*, 764.

[57] N. Bennett, *Phys. status solidi* **2017**, *214*, 1700307.

6. Conclusion

With increasing availability of the development of nanostructure engineering technologies, bulk nanostructured materials are focused on for thermoelectricity. Si is a low-cost, earth-abundant, non-toxic material and highly available in industrial quantities. This dissertation work demonstrates a large potential of Si for high-temperature thermoelectric applications owing to a retention of its high electrical performance together with an enhanced phonon scattering via the formation of self-assembled, refined, nanoscale structures.

6.1 Modeling study

A systematic study on the thermoelectric properties of heavily doped single crystal Si was carried out. The temperature-dependent TE properties of heavily doped (10^{18}-10^{20} cm^{-3}) n-type and p-type single crystal Si were measured from room temperature to above 1000 K and a theoretical model was developed to predict the TE properties of Si on the basis of the Boltzmann transport equation. The results provide fundamental understanding the effect of specific scattering centers for both charge carriers and phonons, laying the groundwork for our following exploration to design and fabricate high-performance Si TE composite with various microstructural components.

6.2 Self-assembled composites

6.2.1 Solid-state precipitations

A simple self-assembly process using a melt-spinning technique followed by spark plasma sintering is introduced to prepare p-type Si/SiB_3 and $Si/CoSi_2$ composites. Sub-micrometer precipitates with a size ranging from several dozens of nm to 500 nm are observed distributed in Si matrix, which only slightly affect the electrical properties and greatly reduced the lattice thermal conductivity by 20% - 44% compared to a homogeneous p-type Si with a similar carrier concentration. Enhanced figure of merit *ZT* values of 0.23 for Si/SiB_3 and 0.21 for $Si/CoSi_2$ at 1073 K were achieved. The results evidence the efficacy of self-assembled precipitates in improving thermoelectric performance of Si and highlight the possibility of the further improvement in *ZT* by optimization of the size of microstructures.

6.2.2 Naturally decorated dislocations

An exploratory research on introducing dislocations in n-type Si/Silicide thermoelectric composites is carried out. Multi-scaled microstructures including high-density nanoprecipitates and dislocations are assembled together by controlling the sintering temperature of a synthesis process based on the route employed in last chapter. These dislocations are found naturally decorated with nanodots, stacking faults and dislocation cores as well as the related strain field. Calculations indicate that in addition to a 30% reduction in lattice thermal conductivity by the nanoprecipitates, while the naturally decorated dislocation contribute an additional 50% reduction, resulting a comparative high figure of merit of 0.39 at 1045K. This work offers a novel self-assembly strategy to further *ZT* enhancement in high performance thermoelectrics.

6.3 Overall comparison and consideration

Figure 6.1 shows an overall comparison of carrier and phonon transport properties of the data obtained from chapter 3 to chapter 5. All the composites prepared by MS-SPS exhibit larger reductions in thermal conductivity compared with Arc-SPSed samples with similar nominal compositions. Silicide precipitates with optimized sizes serve to decrease the thermal conductivity of p-type Si/SiB_3 and $Si/CoSi_2$ composites by increasing heat carrying phonons scattering, while dislocation complex was proved to play a critical role in the dramatic reduction in thermal conductivity of n-type $Si/CoSi_2$ composites. Although concurrent reductions in the electrical conductivity are found due to the degeneration of charge carrier mobility, therefore, limited the power factor to some extent, the overall *ZT* improvement is still achieve owing primarily to enhance phonon scattering.

A compilation of all the available *ZT* data at the time of writing for bulk Si-based material (Most of the data for single Si are excluded for readability) are shown in Figures 6.2 and 6.3. As for the n-type bulk Si thermoelectric, although several studies reported a relative high *ZT* value by consolidation of fine nanocrystals[1][2][3][4][5][6][7], developing self-assembly methods that can avoid the issues like unfavorable oxidation of nanopowders is also one of the most important topic for practical concerns about scalability and reproducibility. Herein, we exhibits a *ZT* of 0.39 at 1045K for n-type $Si/CoSi_2$ composites, which highest value for bulk Si thermoelectrics without employing nanopowders. On the other hand, we offered a unique route for introducing multi-scale microstructures. In our case, melt-spinning technique was employed to synthesize pre-embed nanosilicides in Si matrix, instead of at grain boundary for the well-known formation mechanism by a typical liquid-phase sintering[8]. By simply tuning the sintering temperature during the subsequent spark-plasma sintering, high-density dislocations decorated with various phonon scattering centers can be induced though the grain. Although the primary generation mechanism of dislocations further investigation, this work do provide a new strategy for *ZT* enhancement in high-performance thermoelectrics.

Unlike n-type materials, the thermoelectric p-type bulk Si is rarely investigated (Except for a work of B-doped Si NC where the reported *ZT* is about 3-fold higher than estimated value from the given transport properties[9]). Bux et al.[10] reported that conventional nanostructuring approach do not exhibit as significant a decrease in thermal conductivity in p-type Si, while largely degenerating the carrier mobility. A possible explanation given for the invalid of "bulk Si nanocrystals" method for p-type Si is that overestimation of the solubility of P in Si might to be misleading for determining a proper doping concentration for n-type bulk Si (for most cases, P at. % > 1 %), which lead to an underestimation of the effect of SiP precipitations and consequently an overestimation of grain-size refinement on κ_{lat}. It is reasonable, however, the cubic SiP phase is difficult to distinguish from Si matrix because (a) it is perfectly coherent with the Si matrix, and to be very small in size[11]; and (b) for the case of nanocrystalline Si, most of the excess P tend to segregate in high-density grain boundary.

As stated above, both n- and p-type materials are required in thermoelectric modules. Considering the possible discrepancy of thermal expansion mismatch of different materials, alternative nanostructruing approaches for p-type bulk Si are therefore required to bring about a substantial improvement in over-all thermoelectric performance. In this dissertation, we have herein presented a simple self-assembly process to introduce sub-microscale precipitates for improving *ZT* value of p-type Si (see Figure 6.3). Although we couldn't achieve a considerable high value of *ZT* in the present work, it could be an important design aspect that would allow further exploration to fabricate high-

performance TE composite.

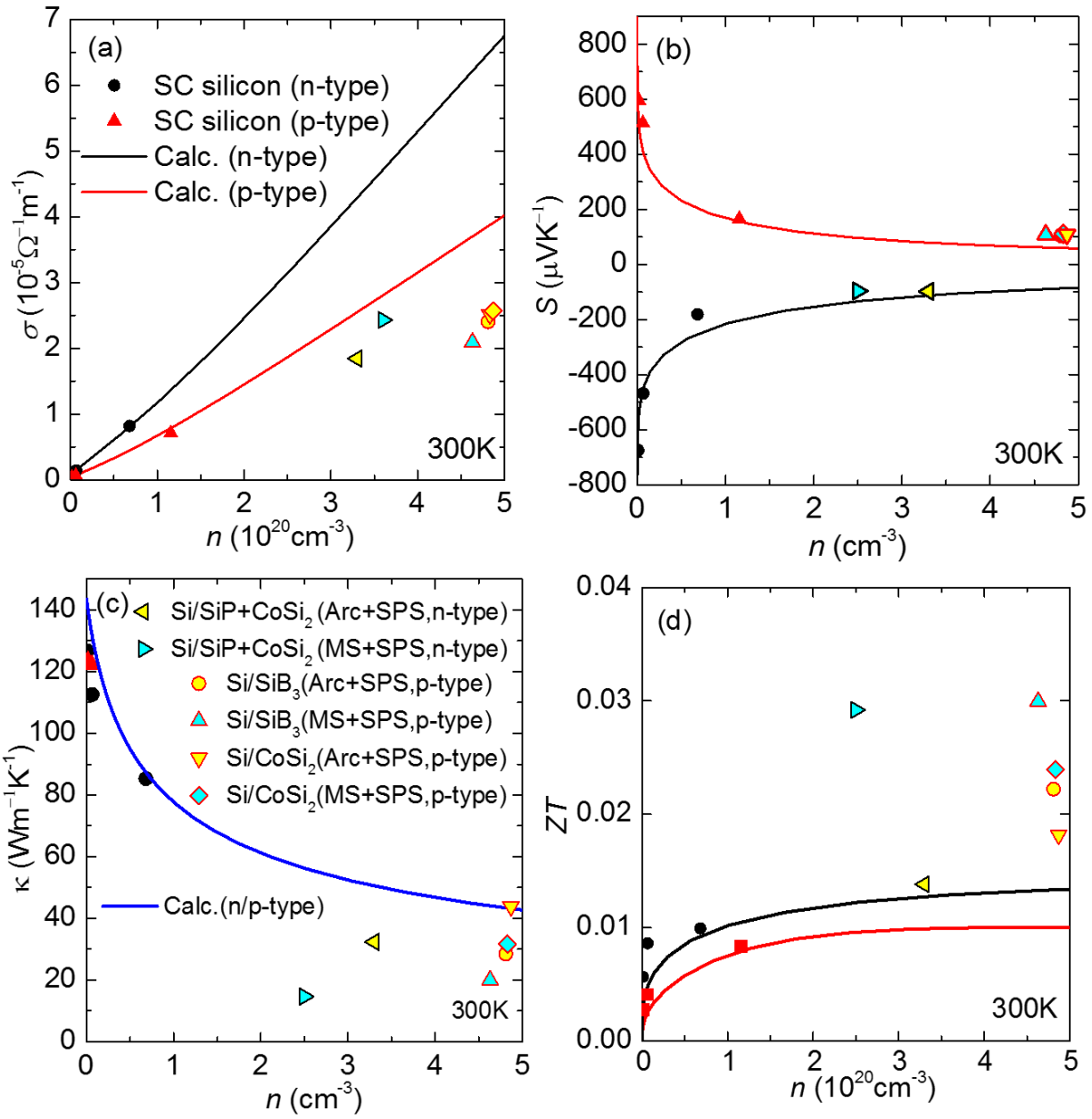

Fig 6.1 Thermoelectric transport properties of Si/Silicide composites as a function of carrier concentration at 300 K: (a) electric conductivity σ, (b) Seebeck coefficient *S*, (c) thermal conductivity κ and (d) *ZT* at room temperature.

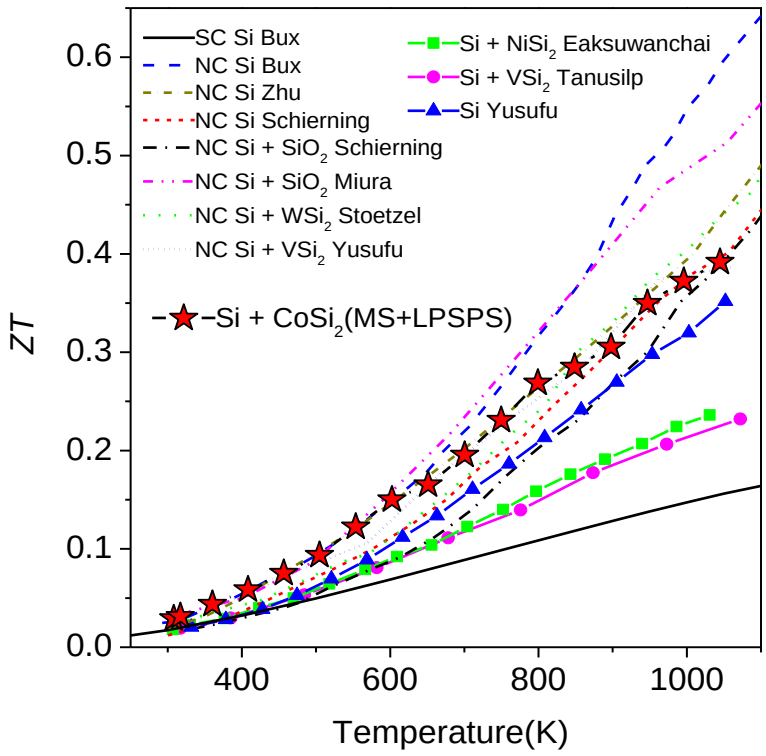

Fig. 6.2 Compare of the temperature-dependent figure of merit *ZT* of nanocrystalline bulk[1][2][3][4][5][6][7] and self-assembled composites[12][13][14]. The data of single crystal (SC) Si is taken from Bux et al.[1]

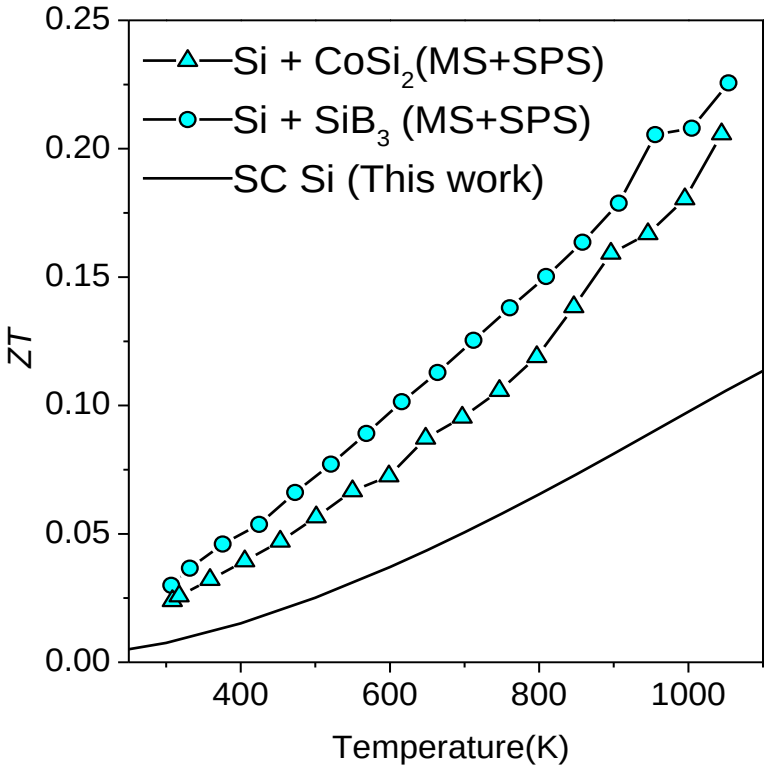

Fig. 6.3 The temperature-dependent figure of merit *ZT* of p-type bulk Si thermoelectric materials. The data of single crystal (SC) Si is taken from chapter 3.

6.4 Outlook for the future work

For achieving the targeting value of $ZT > 1$, the possibility for further improving TE performance for the strategy employed in this dissertation will be discussed here.

As for the electrical properties including σ, *S* and power factor (*PF*), a rough estimation based on the theoretical model established in chapter 3 was shown in Fig. 6.4. When comparing the experimental results attained in this dissertation, the estimated *PF* show highest values in both n-type and p-type. The degeneracy in *PF* of p-type samples prepared by MS+SPS can be attribute to the increasing density of interface between Si and silicide. Note that the reduction of *PF* in the Si+$CoSi_2$ composite was found to be mitigated. Compared to the very different structure of Si and SiB_3, the structural similarity of Si and $CoSi_2$ probably result in suppression of carriers scattering due to the reduction of interfacial defects at their interfaces. As for n-type Si+$CoSi_2$ composites, introduction of both SiP nanoprecipitates and dislocation complex may lead to a large reduction in *PF*. Considering the nanoscale size of SiP and atomic-scale structure in dislocation complex and the electron mean free path(MFP) of ~10 nm in heavily doped Si[15], it is reasonable to expect an enhanced scattering for both phonon and electron by those scattering center. To reduce the influence derived from SiP, which shows coherent interface in the initial precipitation and growth process as nearly spherical particles and semi-coherent interface in plate-like phase, further size-refinement of SiP phase may decrease interfacial defects at the semi-coherent interfaces. However, to achieve a high *ZT* value like *ZT*>1, the unavoidable degeneracy in *PF* of samples with high-density dislocation may become an important issue to be overcome. Making the balance between the enhanced carrier scattering and phonon scattering in those samples is needed for further improvement in *ZT*.

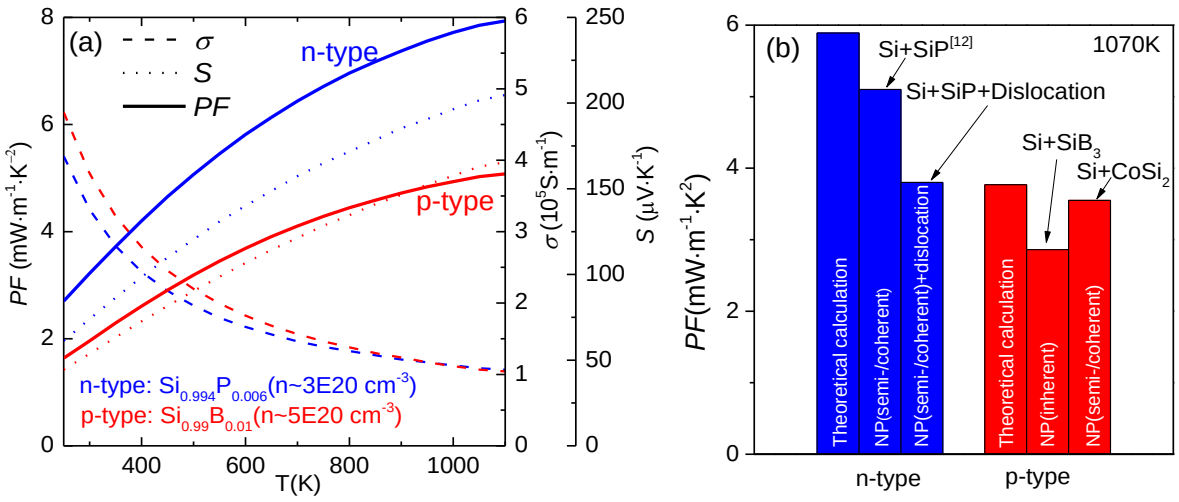

Fig. 6.4 (a) Calculated temperature dependence of thermoelectric transport properties for n- and p-type Si and (b) *PF* of theoretical and experimental data at 1070K.

To discuss the possibility for further improving TE performance by enhancing phonon scattering, the ideal size/density of microstructure should be defined. A simplified configurations of Si-based nanocomposites including precipitates and dislocations are shown in Fig. 6.5. Assuming that charge carriers are scattered only when the characteristic length of microstructure and the spacing between them smaller than the MFP of electron (~10nm in

heavily doped Si[15]), the parameter $a_i = a_p$=10 nm can be obtained for both precipitates and dislocation. Under this assumption, rough estimations of κ_{lat} by employing the theoretical model based on the Boltzmann transport equation with a frequency-dependent phonon mean free path in chapter 5 are shown in in Fig. 6.6. By refinement of the size and density of precipitates as well as density of dislocations, 50%-70% lower κ_{lat} can be expected for both n-type and p-type composites. Assuming there is little deterioration in the electrical properties compared with those of SC Si, estimated *ZT* value can be calculated, which is shown in Fig. 6.7. For heavily doped Si composites with optimized nanoprecipitates, maximum *ZT* value of 0.57 for n-type and 0.35 for p-type at 1070K are estimated. Further, the additional scattering effect of dislocations contribute to a higher *ZT* value of 0.70 for n-type and 0.45 for p-type at 1070K. Compare with the highest literature *ZT* for n-type nanocrystalline Si at same temperature range (*ZT* = 0.62 at 1070K, Bux et al.), this estimation exhibits the possibility to achieve the highest *ZT* among Si-based TE materials by using self-assembly method.

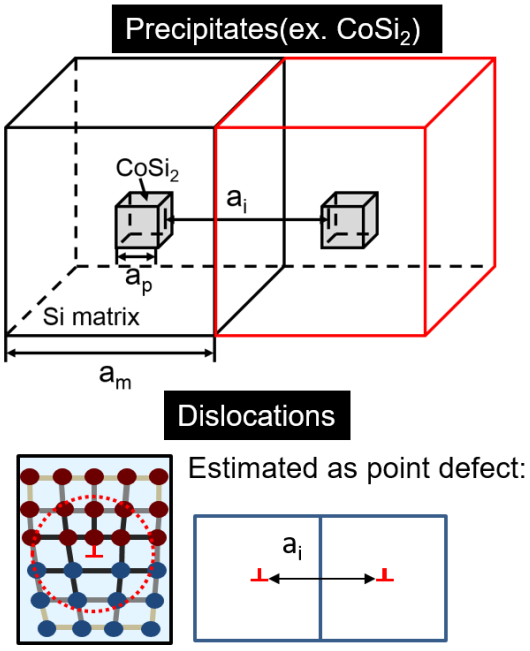

Fig. 6.5 A schematic diagram of Si-based nanocomposites including precipitates and dislocations for estimation of κ_{lat}. Here, we used $CoSi_2$ as a typical precipitate with semi-coherent/coherent interface.

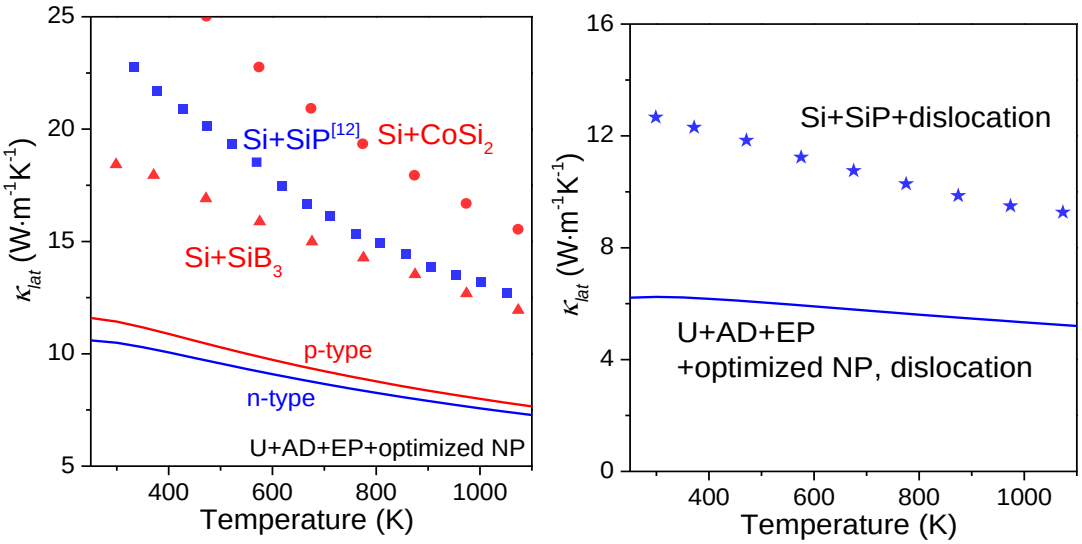

Fig. 6.6 The temperature-dependent κ_{lat} of bulk Si thermoelectric materials.

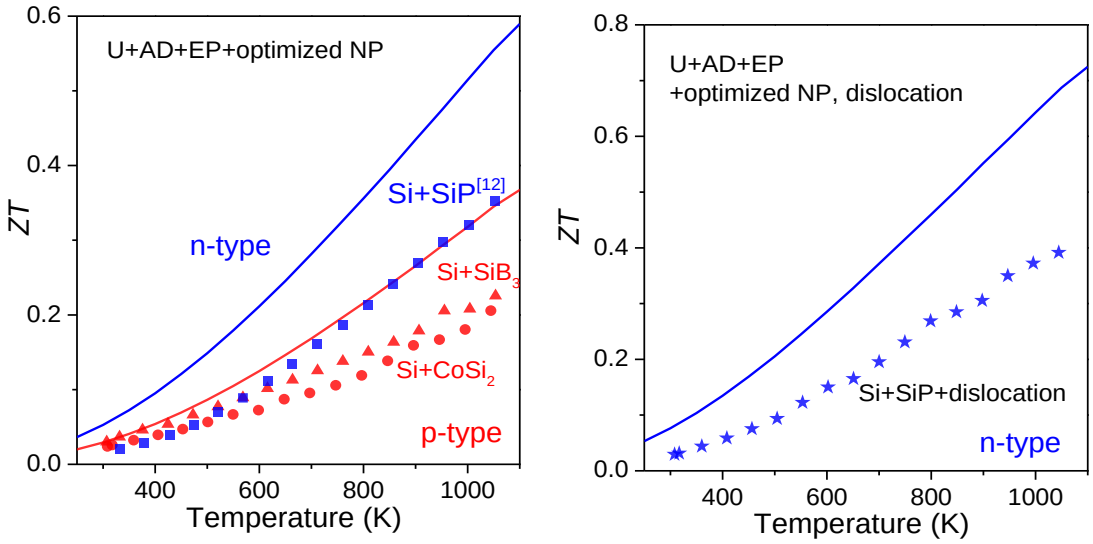

Fig. 6.7 The temperature-dependent figure of merit *ZT* of bulk Si thermoelectric materials.

Even if the strategies employed in this work are optimized, further work should be done to reach *ZT*~1. One of the most promising and effective strategy which can contribute to additional improvement on *ZT* for Si-based TE composites is size-refinement of Si. Here, we employed frequency-dependent model for grain boundary scattering[16]. By assuming an optimized grain size of 10 nm, extremely low κ_{lat} of ~ 1.8 W·m^{-1}K^{-1} can be obtained among the whole temperature range, which is close to the minimum κ_{lat} (κ_{min} = 1.28 W·m^{-1}K^{-1}) estimated from the model of Cahill and Pohl[17,18], as shown in Fig. 6.8(a). Thus, with optimized nanoprecipitates, grain boundary and dislocation density, maximum *ZT* value of 1.14 for n-type and 0.74 for p-type at 1070K for heavily doped Si composites can be expected. The theoretical maximum *ZT* due to phonon scattering enhancement is 1.26 for n-type and 0.82 for p-type at 1070K. In these case, since the electrons become the dominant heat carriers, it is possible that such high carrier concentration (>1×10^{20} cm^{-3}) should be tuned to a lower level to achieve a peak value of *ZT*.

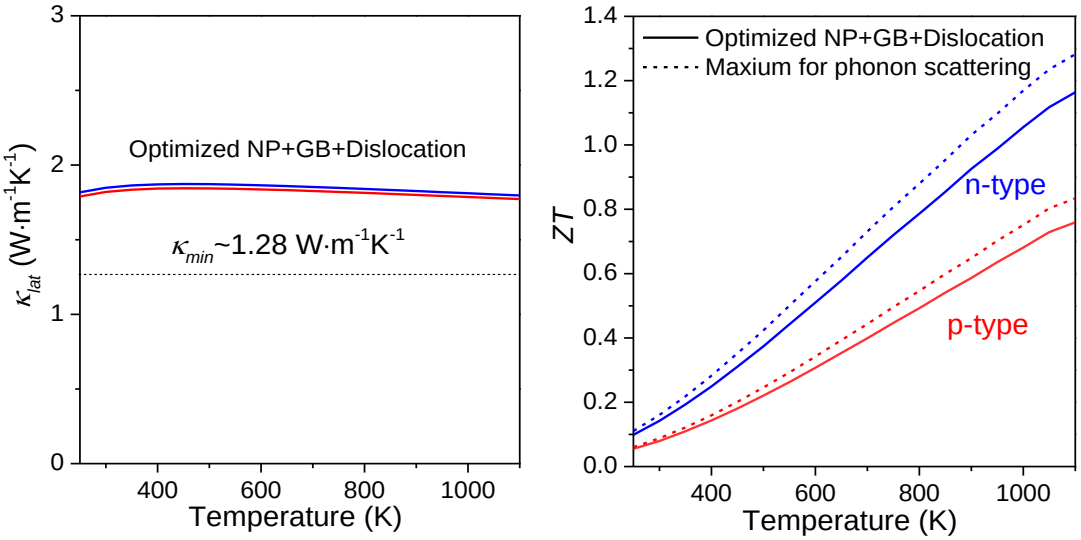

Fig. 6.8 (a) Calculated temperature dependence of κ_{lat} and (b) Calculated temperature dependence of *ZT*.

In retrospect, the effects of synthesis process on the microstructure, charge carrier and phonon transport properties has been studied systematically targeting an optimized the figure-of-merit *ZT* of bulk Si. The Si/silicide bulk composites are demonstrated as competitive candidates for further development of high-temperature thermoelectric applications. The findings on the microstructure control and improvements on the thermoelectric properties in this PhD dissertation will not only provide guidance for future materials design in bulk Si thermoelectrics, but also a convenient self-assembly approach to optimize the microstructures in nanoscale, which strongly depends on the tunable parameters in the synthesis process (ex. temperature, time and chemical composition).

6.5 Reference

[1] S. Bux, R. Blair, P. Gogna, H. Lee, G. Chen, M. Dresselhaus, R. Kaner, J. Fleurial, *Adv. Funct. Mater.* **2009**, *19*, 2445.

[2] T. Zhu, G. Yu, J. Xu, H. Wu, C. Fu, X. Liu, J. He, X. Zhao, *Adv. Electron. Mater.* **2016**, 1600171.

[3] T. Claudio, N. Stein, D. Stroppa, B. Klobes, M. Koza, P. Kudejova, N. Petermann, H. Wiggers, G. Schierning, R. Hermann, *Phys. Chem. Chem. Phys.* **2014**, 25701.

[4] A. Miura, S. Zhou, T. Nozaki, J. Shiomi, *ACS Appl. Mater. Interfaces* **2015**, *7*, 13484.

[5] G. Schierning, R. Theissmann, N. Stein, N. Petermann, A. Becker, M. Engenhorst, V. Kessler, M. Geller, A. Beckel, H. Wiggers, R. Schmechel, *J. Appl. Phys.* **2011**, *110*, DOI 10.1063/1.3658021.

[6] J. Stoetzel, T. Schneider, M. Mueller, H. Kleebe, H. Wiggers, G. Schierning, R. Schmechel, *Acta Mater.* **2017**, *125*, 321.

[7] A. Yusufu, K. Kurosaki, Y. Ohishi, H. Muta, S. Yamanaka, **n.d.**, *61301*.

[8] S. Kim, K. Lee, H. Mun, H. Kim, S. Hwang, J. Roh, D. Yang, W. Shin, X. Li, Y. Lee, J. Snyder, S. Kim, *Science (80-.).* **2015**, *348*, 109.

[9] V. Kessler, D. Gautam, T. Hülser, M. Spree, R. Theissmann, M. Winterer, H. Wiggers, G. Schierning, R. Schmechel, *Adv. Eng. Mater.* **2013**, *15*, 379.

[10] S. Bux, J. Fleurial, R. Blair, P. Gogna, T. Caillat, R. Kaner, *Mater. Res. Soc. Symp. Proc.* **2009**, *1166*.

[11] A. Armigliato, P. Werner, *Ultramicroscopy* **1984**, *15*, 61.

[12] A. Yusufu, K. Kurosaki, Y. Miyazaki, M. Ishimaru, A. Kosuga, Y. Ohishi, H. Muta, S. Yamanaka, *Nanoscale* **2014**, *6*, 13921.

[13] S. Tanusilp, K. Kurosaki, A. Yusufu, Y. Ohishi, H. Muta, S. Yamanaka, *J. Electron. Mater.* **2017**, *46*, 3249.

[14] P. Eaksuwanchai, K. Kurosaki, S. Tanusilp, Y. Ohishi, H. Muta, S. Yamanaka, *J. Appl. Phys.* **2017**, *121*, 225110.

[15] B. Qiu, Z. Tian, A. Vallabhaneni, B. Liao, J. M. Mendoza, O. D. Restrepo, X. Ruan, G. Chen, *EPL (Europhysics Lett.* **2015**, *109*, 57006.

[16] Z. Wang, J. E. Alaniz, W. Jang, J. E. Garay, C. Dames, *Nano Lett.* **2011**, *11*, 2206.

[17] H. Lyeo, D. Cahill, B. Lee, J. Abelson, M. Kwon, K. Kim, S. Bishop, B. Cheong, *Appl. Phys. Lett.* **2006**, *89*, 151904.

[18] J. Cho, X. Shi, J. Salvador, G. Meisner, J. Yang, H. Wang, A. Wereszczak, X. Zhou, C. Uher, *Phys. Rev. B* **2011**, *84*, 85207.

Acknowledgements

The process of writing this dissertation recalled many happy memories and exciting moments during my Master and Doctor's studies. I feel deeply grateful for many people who have taught and inspired me in their own ways. Among these, I would first thank my Doctor's advisor, Associate Professor Hiroaki MUTA, for his strong support, invaluable advices, useful discussions, and over-all guidance through the course of this research work.

I would acknowledge the continuous support and guidance of Associate Professor Ken KUROSAKI that provide better understanding for my research and help me to improve myself in many aspects. I am deeply grateful to Professor Takao YAMAMOTO and Takanori KITADA for their valuable time to examine my progress and his kind advice gave me ideas to accomplish this dissertation.

I want to highly appreciate the enthusiastic help and support of Assistant Professor Yuji OHISHI, for his deep physical insight and constructive criticisms of my research. I feel so lucky, that I had a chance to work in his group and to have his points of view. I would also like to express my gratitude to Associate Professor Satoshi ICHIKAWA, who offered me a precious opportunity to expand my research horizons and many advices on my career development. My special thanks also go to my Master's thesis advisor Professor Shinsuke YAMANAKA, who continuously cared about my PhD progress and provides me with continuous encouragement and sincere guidance in first several years of my work. I also like to thank Dr. Yoshinobu MIYAZAKI, for his help and support, which inspiring me a lot, and Dr. Yusuf EIKEBAIER, for his helpful discussion and encouragement.

It is my pleasure to pay tribute to all the member of Iwatani Naoji Foundation, especially for Mr. Minoru HAGA, Mr. Ikuo KOMATSU, Mr. Takanori OKADA, Ms. Fumi NAKAMURA and Ms. Chikako SHIMADA, for their indispensable financial support over the last two years.

I am grateful to fellow colleagues, for their friendship, support, encouragement: Dr. Fumihiro NAKAMORI, Dr. Masaya KUMAGAI, Dr. Seongho CHOI, Dr. Lei FENG, Mr. Kyungmin Ok, Ms. Afiqa MOHAMAD, Mr. Jungmin KIM, Ms. Yunxia WANG, Mr. Toshiki KONDO, Mr. Yasutaka SHIOTA, Mr. Kenta KONISHI, Ms. Yining SUN and Mr. Tomoki EBATA. Without them, this research cannot be fulfilled.

Finally, I would like to thank the continuous support and encouragement from my parents and my long-term friends, including Jianhua XIE, Qiujuan YANG and Yizhe ZHANG.

Research achievements

Publication

[1] **J. Xie**, Y. Ohishi, S. Ichikawa, H. Muta, K. Kurosaki, and S. Yamanaka, “Naturally decorated dislocations capable of enhancing multiple-phonon scattering in Si-based thermoelectric composites,” *J. Appl. Phys.* **Under review.**

[2] **J. Xie**, Y. Ohishi, S. Ichikawa, H. Muta, K. Kurosaki, and S. Yamanaka, “Thermoelectric properties of Si/$CoSi_2$ sub-micrometer composites prepared by melt-spinning technique,” *J. Appl. Phys.*, vol. 121, no. 20, p. 205107, 2017.

[3] **J. Xie**, Y. Ohishi, Y. Miyazaki, A. Yusufu, H. Muta, K. Kurosaki, and S. Yamanaka, “Thermoelectric properties of Si/SiB_3 sub-micro composite prepared by melt-spinning technique,” *J. Appl. Phys.*, vol. 118, no. 6, p. 65103, 2015.

[4] Y. Ohishi, **J. Xie**, Y. Miyazaki, Y. Aikebaier, H. Muta, K. Kurosaki, S. Yamanaka, N. Uchida, and T. Tada, “Thermoelectric properties of heavily boron- and phosphorus-doped silicon,” *Jpn. J. Appl. Phys.*, vol. 54, no. 7, p. 71301, Jul. 2015.

国内講演会発表

[1] **謝　駿**, 大石　佑治, 市川　聡, 牟田　浩明, 黒崎　健, 山中 伸介, “析出物と転位組織が共存する Si-遷移金属シリサイド熱電コンポジット：微細構造の解析と構造形成の解釈”, 第１４回日本熱電学会学術講演会　PS05, 2017 年 9 月.

[2] **謝　駿**, 大石　佑治, 市川　聡, 牟田　浩明, 黒崎　健, 山中　伸介, “Si-シリサイド系における液相焼結による高密度転位組織の導入と熱電特性への影響”, 第１３回日本熱電学会学術講演会 S2A3, 2016 年 9 月.

[3] **謝　駿**, 大石　佑治, 宮崎　吉宣, Aikebaier Yusufu, 牟田　浩明, 黒崎　健, 山中伸介, “液体急冷を用いた Si/$CoSi_2$ ナノコンポジットの作製と熱電性能の評価”, 第１２回日本熱電学会学術講演会 PS-08, 2015 年 9 月.

[4] **謝 駿**, 大石 佑治, 宮崎 吉宣, 牟田 浩明, 黒崎 健, 山中 伸介, “液体急冷法を用いたSi-Bナノコンポジットの作製と熱電性能の評価”, 第１１回日本熱電学会学術講演会 S2-3, 2014年9月.

International conference

[1] **Jun XIE**, Yuji OHISHI, Satoshi ICHIKAWA, Aikebaier YUSUFU, Hiroaki MUTA, Ken KUROSAKI, and Shinsuke YAMANAKA, “Introducing Dislocation Lines for Controlled Thermal Conductivity in Si-based Nanocomposites by Liquid-phase Sintering” 2017 TMS Annual Meeting & Exhibition, Mar. 2017.

[2] **Jun XIE**, Yuji OHISHI, Yoshinobu MIYAZAKI, Aikebaier YUSUFU, Hiroaki MUTA, Ken KUROSAKI, and Shinsuke YAMANAKA, “Effect of Dislocation Lines on Thermoelectric Properties in Si-based Nanocomposites Prepared by Liquid-phase Compaction” 35th International Conference & the 1st Asian Conference on Thermoelectrics, P269, May. 2016.

[3] **Jun XIE**, Yuji OHISHI, Yoshinobu MIYAZAKI, Aikebaier YUSUFU, Hiroaki MUTA, Ken KUROSAKI, and Shinsuke YAMANAKA, “Thermoelectric Properties of Si/SiB_3 sub-microcomposite Prepared by Melt Spinning Technique” 2016 TMS Annual Meeting & Exhibition, DD-4, Feb. 2016.